T.C.

İNÖNÜ UNIVERSITY

GRADUATE SCHOOL OF NATURAL AND APPLIED SCIENCES

A DECISION SUPPORT SYSTEM BASED ON CONTENT-BASED IMAGE RETRIEVAL FOR BREAST CANCER DIAGNOSIS

NUH ALPASLAN

DOCTOR OF PHILOSOPHY THESIS

DEPARTMENT OF COMPUTER ENGINEERING

JULY 2017

Tezin Başlığı : A Decision Support System Based on Content-Based Image Retrieval for Breast Cancer Diagnosis

Tezi Hazırlayan : Nuh ALPASLAN

Sınav Tarihi : 27 Temmuz 2017

Yukarıda adı geçen tez jürimizce değerlendirilerek Bilgisayar Mühendisliği Ana Bilim Dalında Doktora Tezi olarak kabul edilmiştir.

Sınav Jüri Üyeleri :

Prof. Dr. Abdulkadir ŞENGÜR
Fırat Üniversitesi

Yrd. Doç. Dr. Kazım HANBAY
Bingöl Üniversitesi

Doç. Dr. Muhammed Fatih TALU
İnönü Üniversitesi

Yrd. Doç. Dr. Adnan Fatih KOCAMAZ
İnönü Üniversitesi

Tez Danışmanı: **Doç. Dr. Davut HANBAY**
İnönü Üniversitesi

Prof. Dr. Prabir BHATTACHARYA
Morgan State Üniversitesi

İnönü Üniversitesi Fen Bilimleri Enstitüsü Onayı

Prof. Dr. Halil İbrahim ADIGÜZEL
Enstitü Müdürü

I hereby declare that all information in this document has been obtained and presented in accordance with academic rules and ethical conduct. I also declare that, as required by these rules and conduct, I have fully cited and referenced all material and results that are not original to this work.

NUH ALPASLAN

Dedication

To my loving and caring wife and daughter

Who are the part of my soul and whose love,

affection and confidence enabled

me to achieve this goal

ÖZET

Doktora Tezi

MEME KANSERİ TANISI İÇİN İÇERİK TABANLI GÖRÜNTÜ ERİŞİMİNE DAYANAN BİR KARAR DESTEK SİSTEMİ

Nuh ALPASLAN

İnönü Üniversitesi
Fen Bilimleri Enstitüsü
Bilgisayar Mühendisliği Anabilim Dalı

91+xiv sayfa

2017

Danışman: Doç. Dr. Davut HANBAY
İkinci Danışman: Prabir BHATTACHARYA

Meme kanseri, akciğer kanserinden sonra kadınlarda kanser ölümlerinin en önemli ikinci sebebidir. Meme kanserinin erken bulgularının tespit edilmesi için uzmanlar tarafından genellikle mamogramlar kullanır. Bu sadece tedavi maliyetini değil aynı zamanda hastaların ölüm oranlarını da düşürmektedir. Bununla birlikte, mamogramların yorumlanması genellikle özneldir ve daha düşük duyarlılık ve özgüllük değerleri ile zordur.

Bu tezde, göğüs kitlelerinin otomatik tespiti, sınıflandırılması ve erişimi için entegre bir sistem sunulmuştur. Sistemin amacı görüntüleri iyi huylu, kötü huylu veya normal olarak tahmin edebilmenin yanında ilgili geçmiş vakalara erişim sağlayarak ve görüntüleyerek karar verme sürecine yardımcı olmaktır. Bu kapsamda 3 farklı sistem önerilmiştir. Önerilen ilk sistemde, kitlenin geometrik özellikleri ve önerilen ghsthog, ghstcohog, ghsthogcohg öznitelikleri meme kitlesini ifade etmek için kullanılmıştır. Önerilen ikinci sistemde öznitelik çıkarımı için kitleye ait dokusal, geometrik, alt örnekleme olmayan çevritsel dönüşüm ve önerilen Eig(Hess)-HOG yöntemi kullanılmıştır. Her yöntemin avantajları ve dezavantajları geleneksel yöntemlerle ayrıntılı olarak tartışılmıştır. Son olarak, sınıflandırma ve erişim, destek vektör makinesi ve aşırı öğrenme makinası kullanılarak gerçekleştirilmiştir. Ayrıca, derin öznitelik tabanlı bir sistem geliştirilmiştir. Bu sistemde, hekimlerin kitle hakkındaki kararları, üst düzey derin öznitelikler ile ifade edilmiştir. Sonrasında, yukarıdaki özniteliklere dayalı iki aşırı öğrenme makinası sınıflandırıcısı test görüntülerinin türünü tahmin etmek için kullanılmıştır. Farklı özniteliklere dayalı sınıflandırıcıların sonuçları, test görüntülerinin türünü belirlemek için analiz edilmiştir. Görüntü erişimi ve sınıflandırma performansları, hem kesinlik-duyarlılık hem de sınıflandırma doğrulukları kullanarak iki farklı veri setinde değerlendirilip karşılaştırılmıştır. Deneysel sonuçlar, önerilen sistemin etkililiğini ve gerçek zamanlı klinik uygulamalardaki kullanılabilirliğini göstermektedir.

ANAHTAR KELİMELER: Meme kanseri, Mamogram, Sınıflandırma, Bilgisayar destekli tanı, İçerik tabanlı görüntü erişimi.

ABSTRACT

Ph.D. Thesis

A DECISION SUPPORT SYSTEM BASED ON CONTENT-BASED IMAGE RETRIEVAL FOR BREAST CANCER DIAGNOSIS

Nuh ALPASLAN

İnönü University
Graduate School of Natural and Applied Sciences
Department of Computer Engineering

91+xiv pages

2017

Supervisor: Assoc. Prof. Dr. Davut HANBAY
2nd Supervisor: Prof. Dr. Prabir BHATTACHARYA

Breast cancer is the second leading cause of cancer deaths among women after lung cancer. Physicians generally use mammograms to look for early signs of breast cancer that could reduce not only treatment cost but also patients' mortality rate. However, interpreting mammograms is often subjective and difficult due to lower sensitivity and specificity.

In this thesis, we have presented an integrated system for automated detection, classification, and retrieval of breast masses. The goal of system is to assist decision-making process by retrieving and displaying the related past cases along with predicting the images as benign, malignant or normal. In this manner, we have proposed 3 different frameworks. In our first framework, geometric features of mass and our proposed ghsthog, ghstcohog, ghsthogcohg features are used to express the breast mass. In the second framework, geometric, textural features of mass, nonsubsampled contourlet transform and our proposed eig(Hess)-HOG are used for feature extraction. The advantages and shortcomings of each method are discussed with conventional methods in detail. Finally, classification and retrieval are performed based on using support vector machines and extreme learning machines. Furthermore, a deep feature based framework is developed. In this framework, physicians' decisions on mass were expressed by high-level deep features. Then, two extreme learning machine classifiers based on the features above is employed to predict category of test images. And outputs of classifiers based on each feature were examined together to define the kind of test image. The image retrieval and classification performances are evaluated and compared in two different datasets by using both the precision-recall and classification accuracies. Experimental outcomes indicate the effeciency of the proposed system and the viability of a real-time clinical application.

KEYWORDS: Breast cancer, Mammogram, Classification, Computer-aided diagnosis, Content-based image retrieval.

ACKNOWLEDGEMENTS

First of all, I would like to express my hearty gratitude to my advisors, Prof. Dr. Prabir Bhattacharya and Assoc. Prof. Dr. Davut Hanbay for supervising my studies and encouraging towards pursuing a graduate degree. Without their continuous support, patience and encouragement, the studies presented here could not possibly have been accomplished. I have learned a lot from them through our discussions.

I owe a debt of gratitude to Assist. Prof. Dr. Mahmudur Rahman for his understanding and guidence throughout my graduate studies. I appreciate the considerable amount of time and effort he have invested. I also grateful to Assist. Prof. Dr. Leyla Karaca for her support. Besides, I would like to thank the Inonu University Turgut Ozal Medical Center, Siemens Integrated Service Management Team and particularly to the Field Manager Metin Biçici.

I would also thank to my friends and colleagues İbrahim Işık, Harun Çiğ, Emrah Dönmez and Emrah Boynukara for their support.

I would like to thank to my family who give their best effort in the making of this thesis without expecting nothing in return as their love is the most sincere and unbounded.

To my wife, Emel, no word could not express my feeling towards her. I am so fortunate to have such an invaluable life partner. My deepest heartfelt thanks to my daughter Ayşe, for her smiles encourage me to efficiently overcome the difficulties encountered in my pursuit of PhD degree. Thank you for everything.

Finally, I would like to thank my creator, God, as I always felt his existence by me.

TABLE OF CONTENTS

LIST OF FIGURES

LIST OF TABLES

LIST OF ACRONYMS

ACR	American College of Radiology
ADEWNN	Adaptive Differential Evolution Wavelet Neural Network
AGH	Anchor Graph Hashing
ANN	Artifical Neural Network
BIRADS	Breast Imaging Reporting and Data System
CAGH- ITQ	Composite Anchor Graph Hashing with Iterative Quantization
CoHOG	Co-occurrence Histograms of Oriented Gradients
CNN-CT	Convolutional Neural Network-Curvelet Transform
CNN-DW	Convolutional Neural Network-Discrete Wavelet
DAG	Directed Acyclic Graph
DCT	Discrete Curvelet Transform
DDSM	Digital Database for Screening Mammography
DFT	Discrete Fourier Transform
DOST	Discrete Orthonormal S-transform
DSIFT	Dense Scale Invariant Feature
DWT	Discrete Wavelet Transform
eig(Hess)-HOG	Eigenvalues of the Hessian matrix of HOG
ELM	Extreme Learning Machines
FFT	Fast Fourier Transform
GBVS	Graph-Based Visual Saliency
GFS	Genetic Fuzzy System
GLCM	Gray Level Co-occurence Matrix
HOG	Histograms of Oriented Gradients
IRMA	Image Retrieval in Medical Application
LESH	Local Energy-based Shape Histogram

MCWS	Marker-controlled Watershed Segmentation
NSCT	Non-Subsampled Contourlet Transform
PACS	Picture Archiving and Communication System
PCET	Polar Complex Exponential Transform
PR	Precision-Recall
RLTP	Radial Local Ternary Patterns
ROC	Receiver Operating Characteristic
SGD	Stochastic Gradient Descent
SVM	Support Vector Machines
SWT	Spherical Wavelet Transform
t-SNE	t-distributed Stochastic Neighbor Embedding
WCF	Wavelet Co-Occurrence Feature

1. INTRODUCTION

With the exponential growth of technology, rapidly decreasing storage cost, and constantly increasing internet access, the amount of digital information has been increased exponentially in recent years. Besides, tremendous amount of digital media is rapidly accessed. Therefore, retrieving accurate and relevant information from data has been one of the most significant problem. Content-based image retrieval (CBIR) is utilized in many application areas such as computer aided diagnosis (CAD) systems, art, military and architecture [1]. The demand for satisfactory CBIR systems have increased enormously. Imaging maintains significant assistance in the areas mentioned above. For diagnosis, treatment and tracking of various illnesses, imaging is a quite speedy and non-invasive technique particularly in CAD systems.

As a consequence of advantages in many fields, the digitization of images has gained considerable importance. To manage massive collection of medical image, image retrieval is an effective option.

CBIR is the set of procedures to retrieve relevant images from a database based on automatically extracted features from image content. To express image content detailed, color, texture, shape and object composition features are extracted for both database and query images. This extracted features are utilized to distinguish the most similar the images to query image.

1.1. What is Breast Cancer ?

Breast cancer is considered a major health problem since it is the leading cause of cancer deaths among women after lung cancer in both developed and developing countries [1]–[3]. It is the most widespread cancer type among women that accounts for one-third of all cancer diagnoses in US. Based on the estimates of American cancer society (ACS), there were about 232,000 new invasive breast cancer cases and 41,000 cancer deaths among women in 2015 [4], [5]. Also, Breast cancer incidence has been increased more than two times in last 20 years in Turkey. It will continue to increase in the next years due to the economic, social and cultural factors. According to the Ministry of Health of Turkey, about 163,500 people were diagnosed breast cancer in one year [6]. Although, mortality rates have decreased by 2% in the last 5 years due to the result of treatment improvements, earlier detection of cancer, and awareness, the incidence rate has increased significantly during this time.

The early diagnosis of the breast abnormalities as benign or malignant can remarkably increase the survival chance at the same time reduce the treatment cost and consequent suffering of patients [4], [7], [8]. Thus far, it is considered as the most effective and reliable tool due to its ability to identify the presence of clusters of micro calcifications, architectural distortions, or masses at their initial stage. Although, interpreting mammograms depends on training and experience and is often difficult, error-prone, and subjective with lower sensitivity and specificity [9]. The former phases of cancer have just slight markers. These markers are diversed in appearance, and it is quite tough to diagnose even for practised radiologist [5], [10]. It has been seen that between 60% and 85% of the biopsies of cancer cases predicted by radiologists found benign later and those biopsied women are exposed to needless fear and anxiety [9]. Mammography screening causes eyestrain since only a few turn out to be cancer in thousands of cases. Therefore, an anomaly may be unnoticed [9].

To assist physicians to keep away from miss-diagnosis while reading mammographies, computer-aided diagnosis (CAD) systems have been proposed for analyzing digital mammogram. Numerous procedures have been proposed to assist radiologists in accurate interpretation of mammogram. The detection of suspicious areas of micro-calcification clusters and breast masses often hidden in dense breast tissues [10], [11]. On the other hand, current CAD systems have small influence in supporting physicians detecting subtler cancers associated with mass-like abnormalities due to the relatively low performance in mass detection. Because, they have wide diversities in shape, dimension and are generally indistinctive from surrounding tissue.

1.2. What is Mammography ?

Mammography is high-contrast and high-resolution low-dose-energy X-ray imaging procedure of breast [12]. It is a particularly designed for breast imaging. It is utilized to monitorize detailed structure of breast. Left and right breasts of the women are imaged respectively during having mammogram. Craniocaudal (CC) and mediolateral oblique (MLO) views are the commonly used imaging projections in standard screening mammography as shown in Fig. 1.1. High-standard mammography allows medical experts to examine the delicate structures of breast. Therefore, there

are 4 different images, which are two CC and two MLO of each breast in a typical mammographic examination.

Early diagnosis is quite significant to treat breast cancer. Mammography is quite important in early diagnosis of breast cancer. Researches have shown that the mortality rate can decrease by 30% for women who have mammogram regularly over 50 years of age. Despite improvements in medical imaging, mammography is still the most cost-effective technology for early diagnosis of breast cancer in clinical practice. Total number of mammograms which experts have to read is reached pretty high amounts with the public awareness of mammography screening in the world [11, 12].

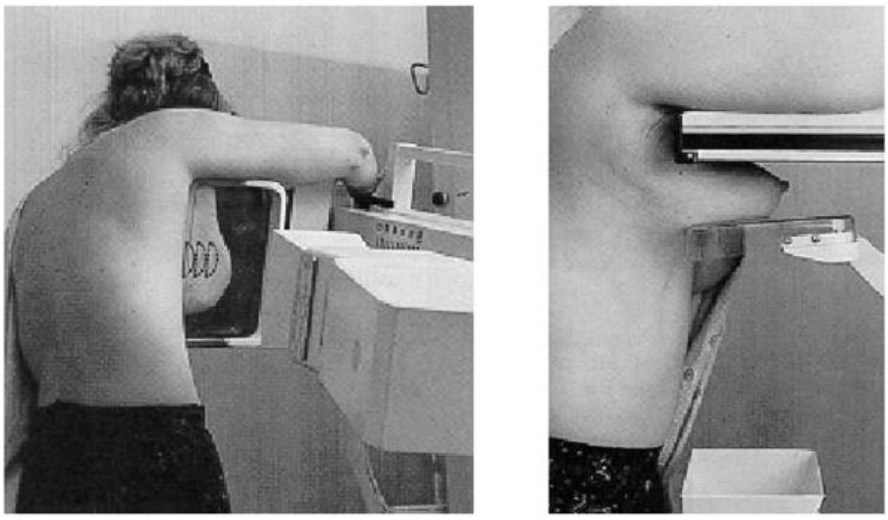

Figure 1.1 Illustration of MLO and CC views of breast [15].

There is not a specific definition about normal mammography. However, normal breast has a wide variation of appearance. The pattern demonstrated in breast is mainly comprises of fat. It is usually considered normal if no inconvenient pattern is found. Fig. 1.2 demonstrates two normal mammograms. Normal mammograms are usually seen with regular and leisure ductal patterns. Breast cancer is mostly seen with disturbed ductal structures.

Breast cancer has 3 main different types as circumscribed/oval masses, spiculated lesions and micro-calcifications. Malignant masses usually have a more non-uniform shape than benign masses. Circumscribed masses are dense and coarsely oval. Radiolucent lesions with an encapsule are generally benign. High radiopaque masses with non-uniform or poorly-defined boundary can be considered highly

suspicious. Fig. 1.3 demonstrates a benign and a malignant mammogram. Spiculated masses have a centrical tumor that is surrounded by a radiating pattern.

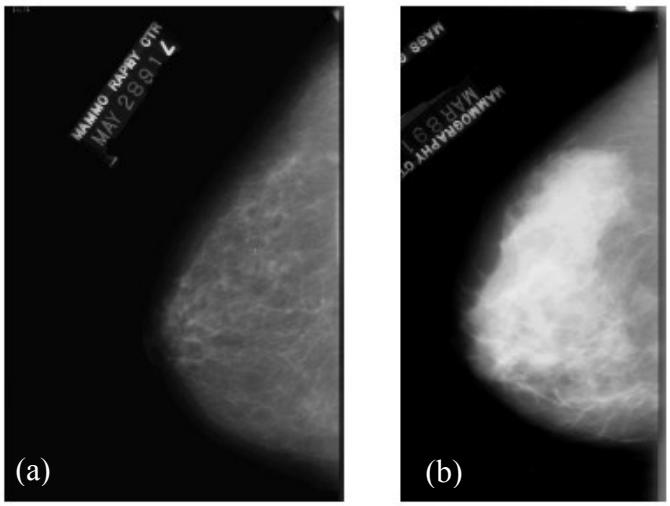

Figure 1.2 (a) fatty normal mammogram, (b) dense normal mammogram [16]

Spiculated masses are largely malignant. Fig. 1.4 demonstrates a mammography with a spiculated mass. Microcalcifications are calcium residuals which appear as bright dot-spots on screening mammography. The shape and distribution of calcifications express malignancy. Benign ones are generally smooth and sharply outlined and have high uniform density. Malignant ones generally appear in non-uniform shape and unstably distributed. Fig. 1.5 demonstrates a benign and a malignant calcification sample. There is not any deterministic boundary between benign and malignant species.

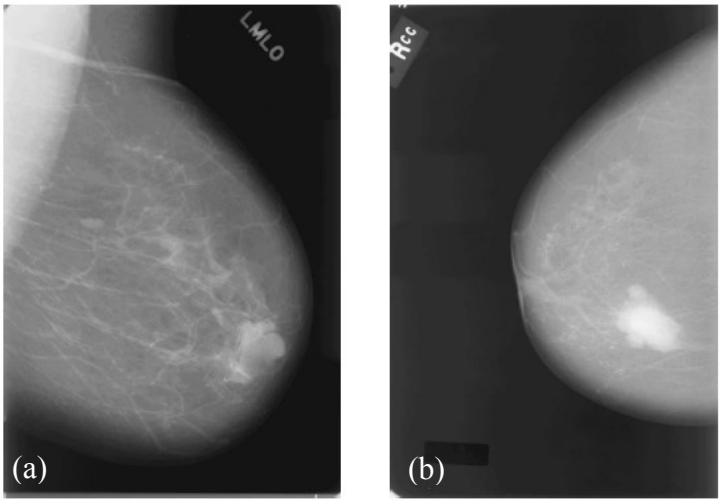

Figure 1.3 (a) benign mass, (b) malignant mass [16]

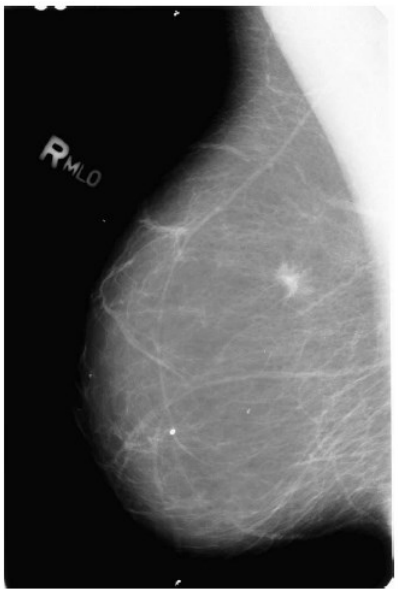

Figure 1.4 A Spiculated lesion mammogram [16]

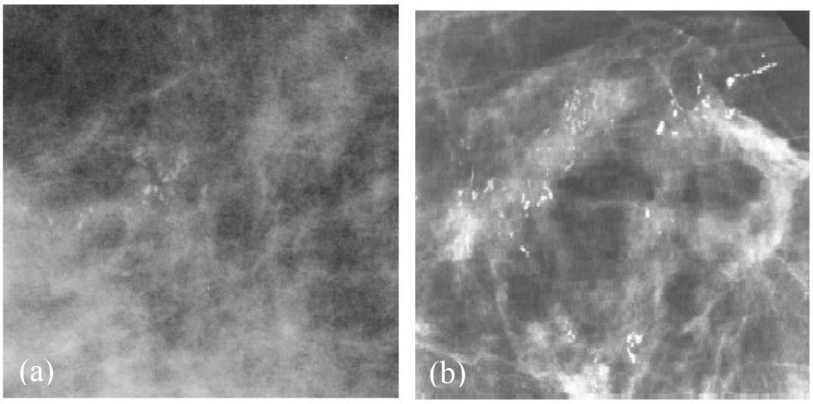

Figure 1.5 (a) a benign calcification, (b) a malignant calcification [16]

Screening mammography and diagnostic mammography are the different types of breast screening examination. Screening mammography is utilized for the patients with no indications to detect tiny masses, which cannot be identified by patient or medical expert, at early stages. Detection of breast cancer at early stages increases the rate of survival remarkably.

Diagnostic mammography is more comprehensive. It is carried out to for the patients, who have a nodule in their breasts. It is also very time consuming and is used to detect exact location and dimension of the mass, related with neighboring tissues. After obtaining further aspects of breast, mammograms are evaluated. There are 2 types of mammography: analog mammography, digital mammography.

1.2.1. Analog Mammography

In analog mammography, an x-ray beam is fired and the effect of x-rays are projected on a film after transition from compressed breast. X-Ray project on phosphor layer on the film constitutes brightness based on its amount. These brightness planes constitute the mammogram. In consequence of x-rays passing across the tissues at varied measures based on structure and thickness of tissue, internal structure of the breast is imaged. This method maintains superior quality breast image with as low radiation as possible. Finally, medical experts interpret mammograms.

Breast tissue contains fat, fiber and gland. Breast masses are seen as white areas. On the contrary, fat appears as black on mammogram. Glands, linking tissues, tumors and microcalcifications appear as white areas at varied plane on mammogram.

For obtaining maximum portion of breast tissue while mammogram imaging, breast is compressed to get a flattered region. The leading cause of compression of breast is to stay away from overlapping tissues possibly. Thus structure of breast and abnormalities can be analyzed better. For example, if breast is compressed insufficiently, low-detailed appearance of micro-calcifications can be obtained which are early indications of cancer. Besides, thanks to breast compression x-ray dose is lowered and patient movement is prevented.

1.2.2. Digital Mammography

Digital mammography utilizes the same infrastructure of analog mammography. However instead of film cassette a digital sensor matrix is utilized to obtain mammogram. So, mammogram is obtained digitally and displayed on a computer directly. According to some studies, digital mammography generates more accurate results than analog mammography. Besides, digital mammography replaces conventional analog mammography rapidly.

Digital mammograms obtained immediately and stored in Picture Archiving and Communication System (PACS). A mammogram consists of 4 images mostly. A general mammogram is expressed in 4096×4096×216 bits, and takes approximately in 30 MB file. Consequently, a breast screening case costs approximately 120 MB of storage. So, mammograms use a remarkable size of storage.

1.3. Masses in Mammograms

Each sort of breast mass has distinct qualifications from neighboring tissues. Thus, the breast masses could be discriminated from neighboring tissues. Texture and morphology properties of mass can be used for discrimination. Determination of mass malignancy is the following significant step after detection of mass.

Shape, contour and margin properties of the mass have critical cues for separation of breast masses. For example, malignant tumors are prone to spread, while benign ones are consistent. Besides, malignant tumors have irregular shaped regions and benign ones have ordinary shapes. Fig. 1.6 shows relation of malignancy with properties of masses.

BI-RADS (Breast Imaging Reporting and Data System) standards is given by ACR (American College of Radiology) on mammography reporting. Considering the BI-RADS, each mass has a score from 0 to 6 according to its morphological and textural properties.

1.4. Thesis Motivations

The breast cancer is the leading cancer type in women, 25% of all cancer cases, and about 1 in every 8 women is diagnosed with breast cancer every year in Turkey. Besides 61% of women have taken mammography in the last 2 years [1]. This means 20 million mammographies every year. In Turkey, it is recommended that women over 50 years old receive annual mammograms. Subpopulations over 40 years old have higher risk. Diagnosis of breast cancer in its early stages through periodic screening is very important to reduce mortality rates. In addition, radiologists perform subjective interpretation by characterizing breast masses as it depends on training and experience. Even for experienced radiologists, the correct evaluation rate ranges from 65 to 75%. False negative rate is 4-20% in current clinical mammography and only 15-34% of women who are sent for a biopsy actually have cancer. To support physicians for avoiding miss-diagnosis, CAD and/or content based image retrieval (CBIR) systems is required for analyzing digital mammogram. All the reasons mentioned above are motivations of our thesis.

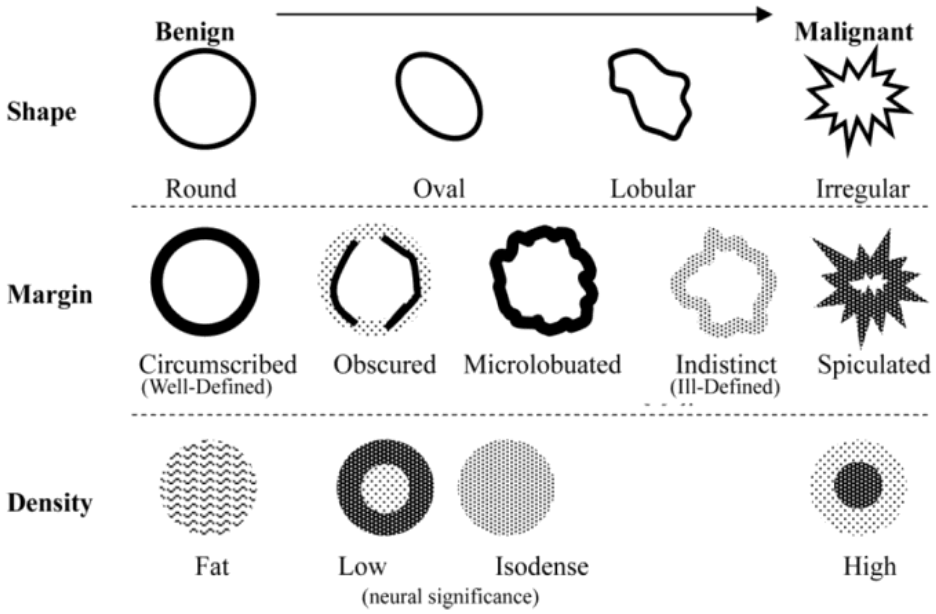

Figure 1.6 Relation of textural and morphological properties of masses with malignancy [17]

1.5. Thesis Objectives and Contributions

The aim of this thesis is to develop a novel integrated decision support system for the automated mass detection, classification and retrieval of mammograms. The main objective of this thesis is to demonstrate how the image retrieval and classification can be integrated and effectively used as a diagnostic tool to support the radiologist for the mass detection. The contributions of this work can be expressed as follows:

1. 3 different CBIR frameworks have been proposed.
2. In first framework, 3 different feature vectors have been proposed. The first method uses combination of geometric features of mass and histogram features of the HOG. The second method uses combination of geometric features of mass and histogram features of the CoHOG. The third method exploits combination of geometric features of mass and histogram features of HOG and CoHOG.
3. In second framework, eig(Hess)-HOG feature vector have been proposed. NSCT are used for mass feature extraction. Additionally, a 9-D shape feature and a 7-D mass feature are extracted which represent the mass boundary and the average contrast, smoothness, orientation, uniformity, entropy, perimeter and circularity [18]. Finally, a 6-D texture features representing the energy,

correlation, entropy, inverse difference moment, contrast and homogeneity are obtained from the GLCM.

4. In our third framework, deep feature based feature extraction is proposed. Fine-tuning operation is applied on the trained CNN network. The obtained network is used for extracting features in next procedures. Then high-level features which are extracted from fully connected (fc7) layer of trained model and f_1 feature set are extracted for training 2 ELM classifiers. And the outcomes of these two classifiers are combined. Therefore, the proposed decision mechanism simulates the doctors' thought structure in the diagnosis.
5. Also, ELM based CBIR system is proposed. In this manner, retrieval time is reduced, retrieval precision and classification accuracy is increased.
6. Compared with state of art studies, third framework has the highest accuracy, sensitivity and specificity.
7. Besides compared with state of art studies, the proposed framework I has lower feature dimension. Therefore, it has the best time efficiency. The mean running time for the classification is 0.02s.
8. Furthermore, a novel mammography dataset is developed, which is named IUMD (Inonu University Mammography Dataset) in this thesis. The dataset is obtained from Inonu University, Turgut Ozal Medical Center.

1.6. Organization of the Thesis

The rest of the thesis is constructed as follows. Section 2 gives the literature review and background, specially about the CAD-based CBIR systems for mammographic mass retrieval. The experimental datasets are demonstrated in Section 3. The breast mass contour segmentation methods and utilized feature extraction frameworks for digital mammography are described in Section 4 and 5 respectively. General properties of convolutional neural networks are explained in Section 6. Experimental results and all the discussions about experiments are given in the Section 7. The last section contains conclusions.

2. LITERATURE REVIEW AND BACKGROUND

2.1. Computer Aided Detection Systems

The diagnosis of breast tumor in early stages is the best opportunity to increase the chance of survival. Therefore, women of aged 40 or older are recommended to take mammogram regularly. However, such a recommendation results in the generation of huge number of mammograms needed to be analyzed. In addition, the interpretation of mammogram images mostly depends on the experience of the radiologists, and the tumors may be overlooked easily while viewing the image in early stages as clinical indications are delicate and varied in appearance [7], [13]. It has been seen that between 60% and 85% of the biopsies of cancer cases predicted by radiologists found benign afterwards and those biopsied women have been exposed to needless fear and anxiety.

To avoid misdiagnosis, computer-aided diagnosis systems were proposed for analyzing digital mammogram due to the rapid advancement of digital imaging, computer vision, pattern recognition and machine learning technologies [19]–[21]. Numeruous methods have been proposed to assist physicians in precise explication of mammograms for detection of micro-calcification clusters and breast masses often hidden in dense breast tissues and classification to benign and malignant lesions utilizing a wide variety of algorithms [22]–[25].

Current CAD systems are non-interactive in nature and the prediction expresses only a cue for the radiologist without the ability to explain the reasoning of the decision-making, as the final decision is left exclusively to him/her. Hence, the clinical advantage of current commercial CAD systems is still under test.

In the last years, CBIR-based CAD systems have back demand to improve physicians confidence in accepting results on decision making [26]–[28]. In [26], an efficient dimension reduction procedure have been proposed in frequency domain for enhanced multi-class breast mass classification. The proposed transform domain bi-modal reduced feature set is utilized with varied classic classifiers. According to obtained results, proposed procedure achieves improvement of 5.35% sensitivity, 3.45% specificity, and 3.98% accuracy as compared with classical domain feature set. In [29], RLTP feature descriptor that utilizes the direction of edge patterns is explored.

The experiments show that the proposed texture features are useful and radial patterns are superior to conventional rotation invariant features. In [30], two-concentric masks and discriminating texton based method are proposed. The advantage of this method against conventional texton is taking into account of class information. Discriminative texton features are obtained for both the center and the periphery region. Therefore, ignorance of the spatial information is enhanced. In [20] a cascade of deep learning methods based on bayesian optimization is proposed for the detection. A level set method based deep structured output learning is proposed for segmentation. Then, deep learning classifier which is pre-trained and fine-tuned based on breast mass dataset is used for the classification. In [31] a novel LESH feature set is proposed for anomaly detection in mammography. Proposed feature set is not only feasible for malignant and benign cases but also among varied types of anomalies. Proposed LESH features are reasonably effective for obtaining significant clinical information from mammography. In [27] the role of the non-negative matrix factorization features in diagnosis is evaluated. Ensemble of classifiers is used for final image recognition. The new approach to the integration of an ensemble is proposed. In [32] wave atom transform based scheme is proposed. Firstly, the mammographies are decomposed into wave atoms. The SVM and kNN are employed for classification. In [28] a wrapper based feature selection approach for WCF using GFS is presented. WCF features are extracted from wavelet coefficients at each level of decomposition of mammographies. In [19], a deep learning based novel classification method is proposed. Two methods, namely, CNN-DW and CNN-CT are presented. In the CNN-DW method, enhanced mammogram images are decomposed as its four subbands by means of 2D-DWT, while in the second method DCT is used. In both methods, DSIFT for all subbands is extracted. Input data matrix containing these subband features of all the mammogram patches is created that is processed as input to CNN. In [33] a novel CAD system by utilizing PCET moments is proposed. In [16] the two-dimensional DOST is used for coefficients extraction. The statistical ‘two-sample t-test’ is proposed to select most important coefficients from a large number of DOST coefficients. AdaBoost with random forest is used as classifier.

However CBIR-based CAD systems are still in development stage with lack of benchmark evaluation in ground-truth datasets and routinely utilization of CBIR systems in clinical practice is still not a reality.

To address the limitation of the current CAD in detecting mass-like abnormalities and due to the ongoing success of CBIR to provide clinical decision support for medical images of different modalities, we proposed to develop an integrated and interactive retrieval system. It will be able to respond to image based visual queries of automatically segmented suspicious mass region by displaying mammograms of relevant masses of past cases that are similar to the queried region as well as predicting the image categories (e.g., malignant, benign and normal masses). The performance and reliability of such a CBIR system depends on a number of issues including the breast mass segmentation, feature extraction, classification and similarity measures.

2.2. CBIR systems

There is a clear need to create effective tools and techniques to retrieve images from large databases for diagnosis due to the phenomenal growth in the amount of mammographies taken in clinical centers in recent years. Due to the freely available datasets, such as the DDSM, interest in developing CAD schemes for mammograms that use CBIR is attracting continued research interest during the last several years [23]–[25].

However, there is only short number of studies dedicated to CBIR-based CAD for mammographies due to the difficulty in mass detection. Preliminary research on CBIR for mammograms was the study of Alto et al. [23], [34] who proposed the use of texture, gradient, and shape features for representation of breast masses for retrieving images. Kinoshita et al. [24] used breast density to retrieve images from a mammogram dataset, available at the University of São Paulo. El-Naqa et al. [35] proposed the use of NNs and SVMs in a two-stage hierarchical learning network for predicting the perceptual similarity. Wang et al. [36] utilized from histograms for the characterization of breast mass in a mammogram database in order to evaluate breast mass automatically. Muramatsu et al. [37] proposed a psychophysical similarity measure. Oliveira et al. [38] proposed a CBIR system called ***MammoSys*** to present mass texture with a two-dimensional principal component analysis (2DPCA) method for dimensionality reduction and SVM) for image retrieval. Wei, L. et al. [39] proposed a classification approach assisted by CBIR to improve the classification accuracy. They presented an adaptive classification scheme in the context of SVM. In [40], a CBIR scheme for large mammography repositories is developed. For this

purpose, AGH algorithm is enhanced and a novel unsupervised hashing algorithm is proposed. Proposed algorithm is named as C-AGH- ITQ. To enhance the efficiency of the hash code, quantization error is minimized by introducing an orthogonal rotation matrix. The proposed scheme is applicable to comprehensive datasets. A novel CBIR scheme is proposed in [41] that utilizes a SVM ensemble capable of optimally utilizing the dispersal of input samples in the feature space based upon BI-RADS classifications of masses as carried out by the radiologists. In an article by Bing Zhang [25], a number of CBIR-based CAD schemes for mammograms were compared and their performance were assessed and it was concluded that much research work is needed before the CBIR-based CAD schemes can be accepted in the clinical practice.

To address the limitation of the current CAD in detecting mass-like abnormalities and due to the ongoing success of CBIR to provide clinical decision support for medical images of different modalities, we proposed to develop an integrated and interactive retrieval system. It will be able to respond to image based visual queries of automatically segmented suspicious mass region by displaying mammograms of relevant masses of past cases that are similar to the queried region. The most challenging problem in this task is detecting the mass from the background and extracting the discriminative local features of clinical importance. For classification, two-class (normal and abnormal) and three-class (normal, benign, and malignant cases) studies are carried out on the individual and combined input feature spaces with 10-fold cross validation. For retrieval, performance is evaluated and compared in a benchmark dataset with different similarity measures.

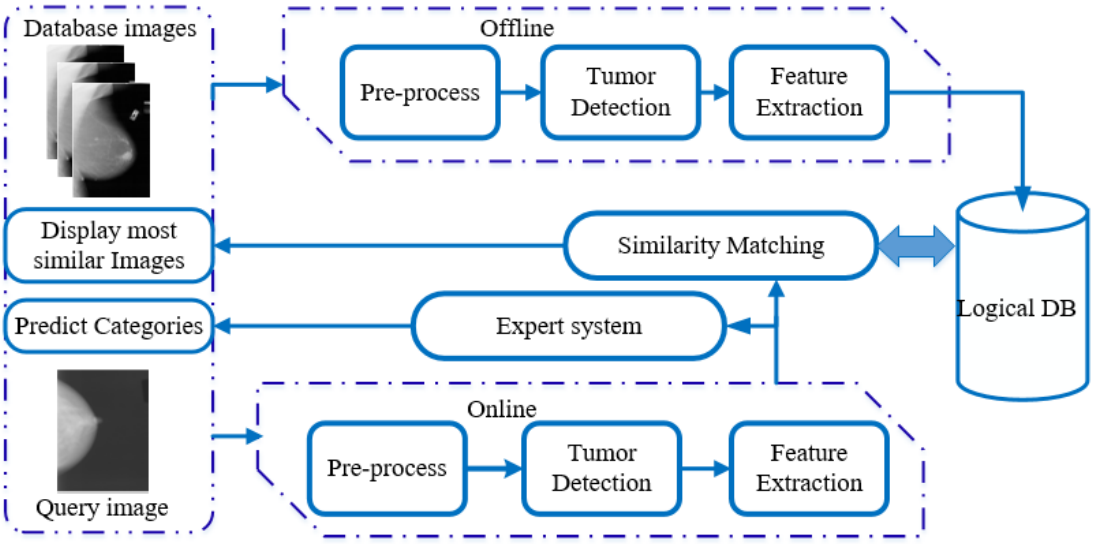

Figure 2.1 Dataflow diagram of CBIR system.

Fig. 2.1 shows the dataflow diagram of CBIR system based on image pre-processing, mass segmentation, feature extraction, classification and retrieval. Preprocessing consists of two steps, noise reduction and enhancement of image. After that, segmentation of tumor is carried out. Next, the feature descriptors are extracted from all mass patches, which were used successfully for object detection in computer vision. Finally, the similarity matching is performed to retrieve similar masses with response to a mass detected in a query (test) image and classification of breast tumors as benign or cancerous (2-class) or normal, benign, or cancerous (3-class) is implemented.

2.3. Similarity Matching Metrics

After feature extraction, the similarity calculation starts. The difference between the feature vector of queried mass (or ROI) and the feature vectors of reference images (or ROIs) is calculated to compute the similarity between the query image and the database. Then, search results are sorted with respect to their measured value of distance. There are many similarity measurement methods that have been used for image retrieval. Image features, descriptor selection and their representation methods directly affect the choice of similarity measurement method. Metrics on vector spaces are the most commonly implemented methods to calculate similarities due to their computational simplicity for linear searching. The following similarity measures were considered in our study. Let denote $\boldsymbol{x}$ a m-by-n data matrix, which is

treated as n (1-by-n) row vectors $x_1, x_1, ..., x_n$ the various distances between the vector x_i and x_j are defined as Eq. (2.1).:

Euclidean distance: $$d_{ij} = \sqrt{(x_i - x_j)(x_i - x_j)'} \quad (2.1)$$

It is a special case of the Minkowski metric, where $p = 2$.

Mahalanobis distance: $$d_{ij} = \sqrt{(x_i - x_j)C^{-1}(x_i - x_j)'} \quad (2.2)$$

where C is the covariance matrix.

City block metric: $$d_{ij} = \sum_{k=1}^{n} |x_{ik} - x_{jk}| \quad (2.3)$$

It is a special case of the Minkowski metric, where $p = 1$.

Chebychev distance: $$d_{ij} = \max_j \{|x_{ik} - x_{jk}|\} \quad (2.4)$$

It is a special case of the Minkowski metric, where $p = \infty$.

Cosine distance: $$d_{ij} = 1 - \frac{x_i x_j'}{(x_i x_i')(x_j' x_j)} \quad (2.5)$$

Correlation distance: $$d_{ij} = 1 - \frac{(x_i - \bar{x}_i)(x_j - \bar{x}_j)'}{\sqrt{(x_i - \bar{x}_i)(x_i - \bar{x}_i)'}\sqrt{(x_j - \bar{x}_j)(x_j - \bar{x}_j)'}} \quad (2.6)$$

where $\bar{x}_i = \frac{1}{n}\sum_k x_{ik}$ and $\bar{x}_j = \frac{1}{n}\sum_k x_{jk}$

The retrieving performance of the CBIR system depends on the effeciency of the above mentioned distance metrics to measure the "similarity" level among the selected images.

It is challenging to find a unique feature representation to compare images correctly for all sorts of queries. Feature descriptors at various levels of image representation are in diversified forms and may be complementary in nature. The

difference between the feature vector of queried mass (or ROI) and the feature vectors of reference images (or ROIs) is utilized to calculate the similarity between the query and reference image. The smaller distance value expresses the higher similarity between the two images. The retrieval performance of CBIR system relies on the efficiency of distance metrics.

2.4. Performance Evaluation

In this thesis, numerous experiments have been conducted to measure performance of proposed classification and retrieval-based decision support system. Performance of each method is computed by accuracy, specificity, sensitivity metrics. All metrics are calculated from confusion matrix. Table 2.1 demonstrates the confusion matrix. As shown in Table. 2.1, True positive expresses the cancer cases that appropriately separated. False positive expresses the normal cases that are wrongly separated. False negative expresses cancer cases that are wrongly separated. True negative expresses the normal cases that are appropriately separated [42].

Table 2.1 Definition of confusion matrix.

		Predicted Class	
		Positive	**Negative**
Actual Class	**Positive**	True Positives (TP) Appropriately classified cancer cases	False Negatives (FN) Wrongly classified cancer cases
	Negative	False Positives (FP) Wrongly classified normal cases	True Negatives (TN) Appropriately classified normal cases

Sensitivity expresses the classification capability of positive results and denoted as in Eq. (2.7).

$$Sens = \frac{TP}{TP + FN} \tag{2.7}$$

Specificity expresses the classification capability of negative results. Specificity formulation is denoted as in Eq (2.8).

$$Spec = \frac{TP}{TP + FN} \tag{2.8}$$

Accuracy expresses the performance of appropriately classified samples averagely. Accuracy is denoted as in Eq (2.9).

$$Acc = \frac{TP + TN}{TP + FN + TN + FP} \tag{2.9}$$

ROC curve is generally used to describe the efficiency of classification performance [43]. It shows the trade-off between the TP rate and the FP rate. To express the system performance, the area under the ROC curve (AUC) is used. The AUC is computed for FP rate over a range that is more relevant. For instance, the AUC was computed for the FP rate range for biopsy recommendation in [44]. ROC analysis was also used to assess the performance of the network to compare the obtained results to other research. PR analysis varies between 0 and 1 while 0 indicates poor and 1 indicates high classification performance.

2.5. Background

2.5.1. Classifiers

To demonstrate the efficiency of low-level features, several classifiers have been used. 10-fold cross validation is used to test each classifier and to guarantee consistence and prediction performance using the MATLAB through its image processing toolbox. We utilized support vector machine [45] and extreme learning machine classifiers in this thesis.

2.5.1.1. Support Vector Machines (SVM)

SVM is a type of linear discriminant analyzer. However, it looks for linear boundaries that separate given classes instead of finding hyper-planes for each class. The SVM carries out classification between two classes by determining a hyper plane in feature space that is based on the most informative points of the training set [45]. It places the maximum number of points of the same class on the same side and maximize the distance of each class to the hyper plane. If the data is linearly separable by a hyper plane, it is called linear separation. Eq. (2.10) denotes the hyper plane, where $w \cdot x$ is

the inner product between vectors w and x, $w \in P$ is the normal vector to the hyper plane and $|b|/\|w\|$ is the perpendicular distance of the hyper plane to the origin, with the bias $b \in R$.

$$f(x) = w \cdot x + b = 0 \tag{2.10}$$

Eq. (2.11) separates the data X into two regions: $w \cdot x + b > 0$ and $w \cdot x + b < 0$. In most cases, whereas, the data cannot be separated by a hyper plane, so a function called kernel is used instead. It receives two points' x_i and x_j from the input space, according to Eq. (2.11), and computes the product between these data in the feature space:

$$Q(x_i, x_j) = \phi(x_i) \cdot \phi(x_j) \tag{2.11}$$

The most commonly used polynomial and Gaussian kernels are defined as in Eq. (2.12) and Eq. (2.13):

$$Q_p(x_i, x_j) = \left(\delta(x_i, x_j) + \mathrm{K}\right)^d \tag{2.12}$$

$$Q_g(x_i, x_j) = \exp(-\sigma \|x_i - x_j\|)^2 \tag{2.13}$$

Where, the parameters δ , K , d in Eq. (2.12) and in Eq. (2.13) must set.

If the number of class is more than two, the problem becomes a multiclass. Various procedures were proposed for multi-class SVM extension. Pairwise coupling (PWC) is utilized for multiclass classification approach [46]. The PWC constructs binary SVM's between all possible pairs of classes. Therefore, this method uses N × (N − 1) / 2 binary classifiers for N classes.

2.5.1.2. Extreme Learning Machines (ELM)

The ELM is a single-hidden layer feed-forward neural network (SLFNs) learning algorithm [47], [48] as shown in Fig. 2.2.

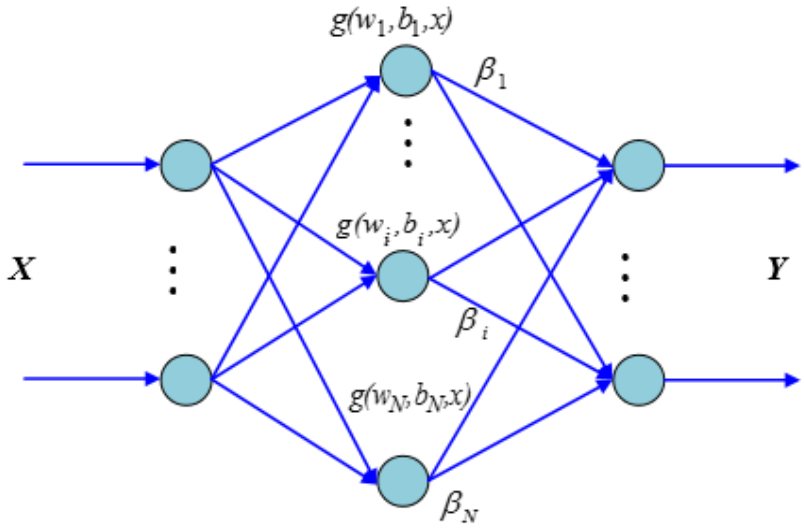

Figure 2.2 Single-hidden layer feedforward network.

For a given a training set consists of N samples (x_i, y_i) with $x_i \in R^d$ and $y_i \in R^d$ the output function y_i with N hidden nodes can be described as Eq. (2.14).

$$y_i = \sum_{i=1}^{M} \beta_i g(\omega_i x_j + b_i), \quad 1 \le j \le N \tag{2.14}$$

where β_i is the output weights, ω_i is the input weights, b_i is the biases of the i^{th} hidden node. And $g(\cdot)$ is the activation function.

It randomly assigns weights and biases firstly for hidden nodes and then analytically defines the output weights by using the least square method. Due to the random selection of weights and biases for hidden nodes, the ELM can decrease the learning time considerably and it can also achieve superior generalization performance [49].

3. EXPERIMENTAL DATASETS

In this part, we will explain different mammography databases which exist to evaluate the efficiency of breast mass detection and classification methods. The DDSM, IRMA mammographic patches and IUMD datasets are utilized in our experiments.

3.1. Digital Database for Screening Mammography (DDSM)

The DDSM dataset is a collaboratively maintained public dataset [51]. It is still being largely used as a benchmark dataset for being free of charge and having a diverse number of cases. The database contains 2620 cases where each case includes two image view anatomy of right and left breasts. Each case/study consists of 6 to10 files.

Table 3.1 Summary of DDSM dataset.

Mass Property	Value	Lesion Count
Shape	Misc	5
	Round	228
	Lobular	587
	Irregular	1308
	Oval	613
BI-RADS Score	0	185
	1	3
	2	131
	3	537
	4	1179
	5	706
Margin	Misc	105
	Circumscribed	618
	Microlobulated	170
	Obscured	408
	Indistinct /ill-defined	753
	Spiculated	687
		Total : **2741**

The size of the images varies from 1024 × 300 pixels to 1024 × 800 pixels. The DDSM database offers more than 9,000 images and from where we selected a total of 5880 images for experiments and result evaluation. Summary of DDSM dataset is demonstrated in Table 3.1.

3.2. Image Retrieval in Medical Application (IRMA) mammographic patches

The Image Retrieval in Medical Application (IRMA) mammographic patches [52] dataset is used to conduct experiments. The IRMA, consisting of MIAS and DDSM datasets, is the benchmark dataset. It contains mammographic patches and many studies have demonstrated effectiveness of their algorithms using a subset of patches from this database. Table 3.2 lists the number of images in both DDSM and MIAS datasets based upon the above discussed classification. Some sample patches are shown in Fig. 3.1.

Table 3.2 Distribution of normal, benign and malignant mammogram patches of 2 different data sets for four BIRADS classes.

IRMA: MIAS Patch Dataset				
BIRADS	Normal	Benign	Malignant	TOTAL
	90	32	38	160
IRMA: DDSM Patch Dataset				
	773	900	903	2576

3.3. Inonu University Mammography Dataset (IUMD)

In this thesis, a mammography dataset is developed, which is named IUMD (Inonu University Mammography Dataset). Case selection is performed retrospectively from PACS system of Inonu University, Department of Radiology, Turgut Ozal Medical Center among more than 20 thousand cases screened between 2011 April and 2017 May. Each case consists of 4 images in DICOM format. All of the information about patient is removed and the whole dataset is anonymized. Finally, IUMD consists of 722 mammographic cases, where expert radiologists annotated each case.

The mammography images have taken from Siemens Mammomat Inspiration device. Each mammogram in IUMD consists of four images in lossless PNG format.

Each image converted from DICOM file. Fig. 3.2 shows the Siemens Mammomat Inspiration device and Table 3.3 shows the summary of IUMD dataset.

Every year thousands of healthy women taken regularly mammography screening. So keeping dose as low as possible is extremely important. This protects women from unnecessary radiation while pursuing premium image quality. At the same time high image quality is the key to detecting the smallest detail. Mammomat Inspiration device gives promising results with up to 30% less dose and without compromising image quality. This reduces the variation between operators and examinations and the risk of patient movement.

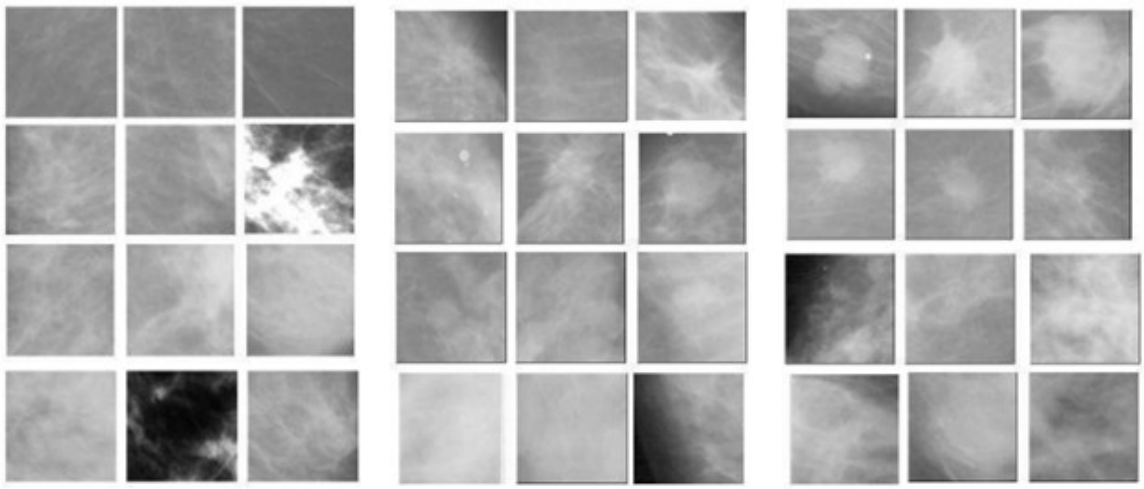

Normal *Benign* *Malignant*

Figure 3.1 Examples of IRMA mammographic patches

Table 3.3 Summary of IUMD dataset.

IUMD Dataset

BIRADS SCORE	Number of images
0	300
1	844
2	384
3	888
4, 5	472
Total	2888

3.4. The ImageNet Large Scale Visual Recognition Challenge (ILSVRC)

ILSVRC is the most common natural image dataset which consists of more than 1 million image. It is generally utilized in deep learning applications. It also maintains enough number of samples with determined labels and this is pretty significant for training a deep model [53].

Figure 3.2 Siemens mammomat inspiration device

4. UTILIZED FEATURE EXTRACTION FRAMEWORKS

Feature extraction plays key role in breast cancer diagnosis framework. Feature extraction procedure can only be carried out if the suspicious regions of breast masses are appropriately defined. Obtained features must be distinguishable, believable and independent. Furthermore, the obtained features must be acceptable in size for applicability and computationally efficient. In selecting effective features from mammogram lesions, numerous studies were focused on capturing the texture of images and improving correlation to the human visual similarity [5], [18]. Among them, Curvelet transform, Gabor Wavelet, DWT (Discrete Wavelet Transform), and SWT (Spherical Wavelet Transform) have been widely examined and compared [54], [55] in addition to other widely used texture features obtained from the co-occurrence matrices and fourier transform. Since breast mass sample can be indicated on varied locations of the mammograms with varied orientations, the obtained features must be the linear shift and rotation invariant. Considering this criteria, NSCT (Non-Subsampled Contourlet Transform), the HOG (Histograms of Oriented Gradients) and the CoHOG (Co-occurrence HOG) based methods are used to extract features from region-of-interests (ROIs) based on the mass contour segmentation results (a rectangular ROI was generated from the bounding box (BB) of each mass).

4.1. Digital Mammography Feature Extraction Framework I

In first framework, different combination of concatenated feature vectors have been used for classification and retrieval experiments. We have proposed 3 different feature vectors. The first method uses combination of geometric features of mass and histogram features of the HOG named ghsthog. The second method uses combination of geometric features of mass and histogram features of the CoHOG named ghstcohog. The third method exploits combination of geometric features of mass and histogram features of HOG and CoHOG named ghsthogcohg. The details of proposed methods will be explained in the following section.

4.1.1. Histogram of Oriented Gradients (HOG)

HOG is a keypoint descriptor which expresses the local statistics of the gradient orientations around a keypoint [56]. The HOG can express object appearance for the reason that the histogram process gives translational invariance and the gradient orientations are strong to lighting changes, hence mostly applied in pedestrian

detection tasks. There are two components in HOG feature extraction process. One is the cell and the other is the block. Fig. 4.1 summarizes the computation of HOG feature extraction process. The HOG feature extraction process consists of three phases. In the first phase, first order derivatives in x and y directions are computed and the image is divided into $m \times n$ tiled regions. The first order derivatives are calculated by filtering the image with Eq. (4.1) and (4.2) and gradient magnitudes and orientations are calculated with Eq. (4.3), Eq. (4.4) respectively.

$$f_x(x,y) = I(x+1,y) - I(x-1,y) \quad \forall x \tag{4.1}$$

$$f_y(x,y) = I(x,y+1) - I(x,y-1) \quad \forall x,y \tag{4.2}$$

$$m(x,y) = \sqrt{f_x(x,y)^2 + f_y(x,y)^2} \tag{4.3}$$

$$\theta(x,y) = \tan^{-1}\left(\frac{f_y(x,y)}{f_x(x,y)}\right) \tag{4.4}$$

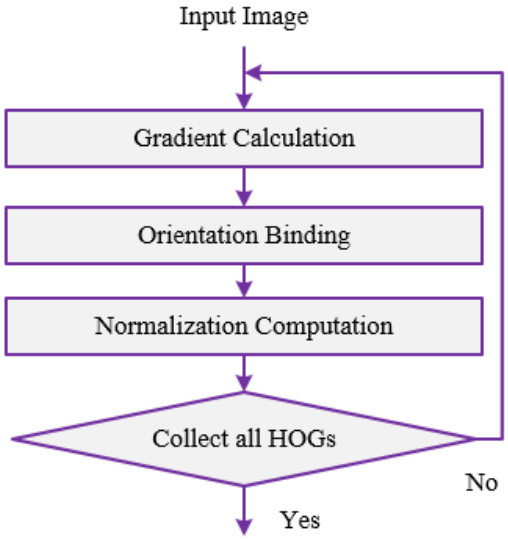

Figure 4.1 Overview of HOG calculation

Gradient orientations divided into n bins. Then, for each tiled region 1-D histogram of gradient orientations which is weighted by gradient magnitude is calculated. Eventually, obtained feature vectors are normalized and HOG feature vectors are collected for all blocks [56].

4.1.2. CoHOG Feature Extraction

CoHOG is an effective gray level feature descriptor based on gradient orientations [57], [58] which expresses the distribution of gradient orientations from co-occurrence matrices for a given offset over an image. The combinations of neighboring gradient orientations provide reliable features for object recognition in images, and therefore this is very beneficial for image classification problems.

$$C_{i,j} = \sum_{p=0}^{n-1} \sum_{q=0}^{m-1} \begin{cases} 1 & \text{if } \theta(p,q) = i \text{ and } \theta(p+x,q+y) = j \\ 0 & \text{otherwise} \end{cases} \tag{4.5}$$

Where the matrix θ represents gradient orientations and the parameters x and y represent vertical and horizontal offset values. The overview of CoHOG calculation is represented in Fig. 4.2. Firstly, gradient orientations (θ) are calculated by Eq. (4.4) as shown in Fig. 4.2 (a) and orientation angles in the range $[0,2\pi)$ are quantized into eight labels. Each label stands for an orientation for each pixel. For instance, orientation angle in the range of (π/4, π/2] is labeled by the number "2". Where u and v are the vertical and the horizontal components of gradient vectors, respectively. The indices (i, j) represent pixel positions in image matrix denoted by $I(i, j)$. Secondly, the co-occurrence matrix (CM) C is obtained by gradient orientations of $n \times m$ image according to Eq. (4.5) as shown in Fig. 4.2 (b). A pixel-pair can be represented by an offset, which express the spatial relationship between two points. Ten different offsets {(0,1), (0,2), (1,1), (1,2), (2,1), (1,0), (2,0), (1,-1), (1,-2), (2,-1)} were used in experiments.

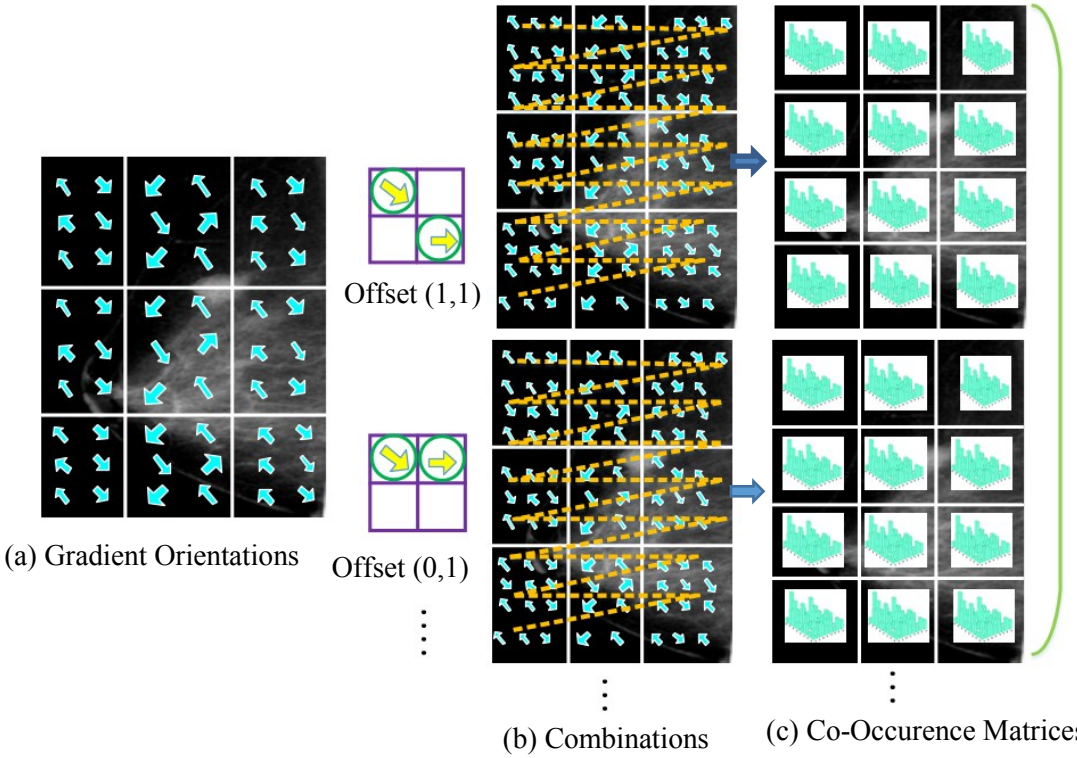

Figure 4.2 Overview of CoHOG calculation.

The CM conveys info related with the local textures by using short-range offsets and the global textures by using long-range offsets [34]. By using short range and long range offsets, the CMs can represent shapes in a detailed way. In addition, relative location and orientation are considered with each neighboring pixel, respectively. The CMs are computed for each small region with all offsets as shown in Fig. 4.2 (c). Finally, the components of all the co-occurrence matrices are concatenated into a single vector. From one tiled region, CoHOG obtains 10 CMs. Each CM has 8×8 components.

4.1.3. Intensity histogram features

The histogram features extracted from the HOG and the CoHOG features of breast masses are mean, variance, skewness, kurtosis, entropy and energy that show the variation of mass features in different ways. The first order statistical features for this study are mean, variance, skewness, kurtosis, entropy and energy features calculated using the standard expressions derived in [5] and defined in Eq. (4.6), Eq. (4.7), Eq. (4.8), Eq. (4.9), Eq. (4.10), and Eq. (4.11).

$$Mean\,(h_1) = \sum_{i=0}^{N-1} h(i) \Big/ N \tag{4.6}$$

$$Variance\,(h_2) = \frac{\sum_{i=0}^{N-1} (h(i) - \bar{h})^2}{N} \tag{4.7}$$

$$Skewness\,(h_3) = \frac{\sum_{i=0}^{N-1} (h(i) - \bar{h})^3}{N \times s^3} \tag{4.8}$$

$$Kurtosis\,(h_4) = \frac{\sum_{i=0}^{N-1} (h(i) - \bar{h})^4}{N \times s^4} \tag{4.9}$$

$$Energy\,(h_5) = \sum_{i=0}^{N-1} h(i)^2 \tag{4.10}$$

$$Entropy\,(h_6) = \sum_{i=0}^{N-1} h(i) \log h(i) \tag{4.11}$$

4.1.4. Geometrical features

The breast tumors are variegated in shape and location. Because of the variance, the roughness, size, shape, edge and density are geometrical features that are an important basis for tumor detection. Based on the segmentation of tumor, its geometrical features: roundness, entropy of standardized radius, variance of standardized radius, ratio of area and roughness are extracted and analyzed.

Roundness: The smoother the edge indicates the smaller the roundness, and the greater the odds of it being a benign tumor. Roundness is defined as

$$g_1 = \frac{P^2}{A} \tag{4.12}$$

Where P is the perimeter, A is the area of mass.

Variance of standardized radius: It describes the range of variance of the standardized radius. It is defined as

$$g_2 = \sqrt{\frac{1}{N-1} \sum_{i=1}^{N} \left(d(i) - d_{avg}\right)^2} \tag{4.13}$$

Where N is the number of edge points, *d(i)* is the *i-th* standardized radius of edge points.

Ratio of area: It describes the circularness of a tumor. If the value is smaller, the shape of the image is similar to a circle. It is defined as

$$g_3 = \frac{1}{d_{avg} N} \sum_{i=1}^{N} \left(d(i) - d_{avg} \right) \tag{4.14}$$

Where $d(i) - d_{avg} = 0 \ \forall d(i) \le d_{avg}$ is the average standardized radius of edge points.

Roughness: The more irregular the shape is, the bigger the roughness. It is defined as

$$g_4 = \frac{1}{N} \sum_{i=1}^{N} \left| d(i) - d(i+1) \right| \tag{4.15}$$

In this thesis, a model of feature vectors is established mathematically in the form

$$f = [f_1 \ \ f_2] \tag{4.16}$$

where both f_1 and f_2 are multidimensional vectors, f_1 presents the 1-D intensity histogram features (Table 4.1) of a tumor and f_2 presents the geometrical features of HOG and/or CoHOG features of a tumor. The formats of f_1 and f_2 are shown as

$$f_1 = [h_1 \ \ h_2 \ \ h_3 \ \ h_4 \ \ h_5 \ \ h_6] \tag{4.17}$$

Where, h_1, h_2 ,h_3, h_4, h_5, h_6 are the six intensity features set of a tumor.

$$f_2 = [g_1 \ \ g_2 \ \ g_3 \ \ g_4] \tag{4.18}$$

Where, g_1 , g_2 , g_3 and g_4 are the four geometric features set of a tumor.

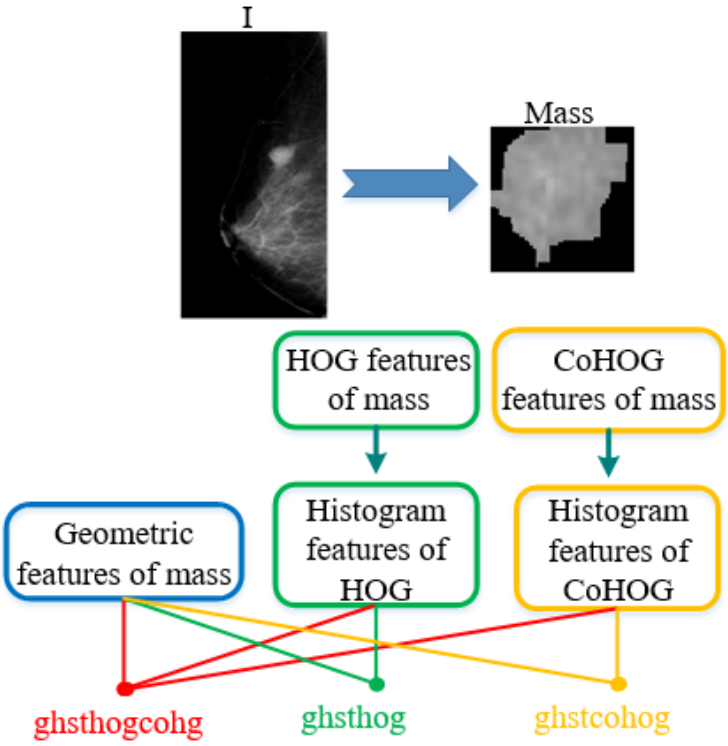

Figure 4.3 Flowchart of the proposed feature extraction process.

Finally, we used different combination of concatenated feature vectors for classification and retrieval experiments as shown in the process flow chart in Fig. 4.3. The first method uses combination of geometric features of mass and histogram features of the HOG named ***ghsthog.*** The second method uses combination of geometric features of mass and histogram features of the CoHOG named ***ghstcohog***. The third method exploits combination of geometric features of mass and histogram features of HOG and CoHOG named ***ghsthogcohg.***

4.2. Digital Mammography Feature Extraction Framework II

In our second proposed framework, eig(Hess)-HOG feature vector has been proposed. NSCT is used for mass feature extraction. Additionally, a 9-D shape feature and a 7-D mass feature are extracted which represent the mass boundary and the average contrast, smoothness, orientation, uniformity, entropy, perimeter and circularity [18]. Finally, a 6-D texture features representing the energy, correlation, entropy, inverse difference moment, contrast and homogeneity are obtained from the gray level co-occurrence matrix (GLCM). Detailed explanation of proposed framework will be given in next section.

4.2.1. Non-Subsampled Contourlet transform

Despite different applications of Wavelet Transform (WT) in medical image analysis, it has some limitations in capturing the directional information in images such as smooth contours and the directional edges [59]–[63]. For example, orthogonal wavelets consider only horizontally, vertically, and diagonally directed discontinuities. These directions do not effectively express the edges and textures of medical images such as breast mammograms which have smooth curves that represent benign, malignant masses and micro-calcifications, etc. To express the contour-like smooth edges directly in the discrete domain effectively, the Contourlet Transform (CT) was introduced by Do and Vetterli [64], which is an extension of the WT that uses multi scale transform that is constructed by combining the Laplacian pyramid with directional filter banks (DFB) and has additional characteristics such as directionality and anisotropy in addition to the properties of WT. Although the CT is a more effective method than the WT in image representation, it is not shift-invariant due to down-sampling and up-sampling. NSCT was proposed by Cunha et al. [65] to compensate this limitation and due to its beneficial features, the NSCT has been used in this thesis for representing the breast masses according to its features.

In NSCT, to keep away from the frequency aliasing of the CT and to obtain the shift-invariance, the non-subsampled Laplacian Pyramids (NSLP) and the non-subsampled directional filter banks (NSDFB) are utilized based on idealized frequency partitioning obtained with the structure proposed in [64], [65]. Additionally, the multi-scale and directional decomposition processes are free from each other. The number of decomposition directions is changeable and can be adjusted to any value of 2^{l_j} where the l^j parameter can be represented at scale j, $1 \leqslant j \leqslant J$ and J represents the number of decomposition scales.

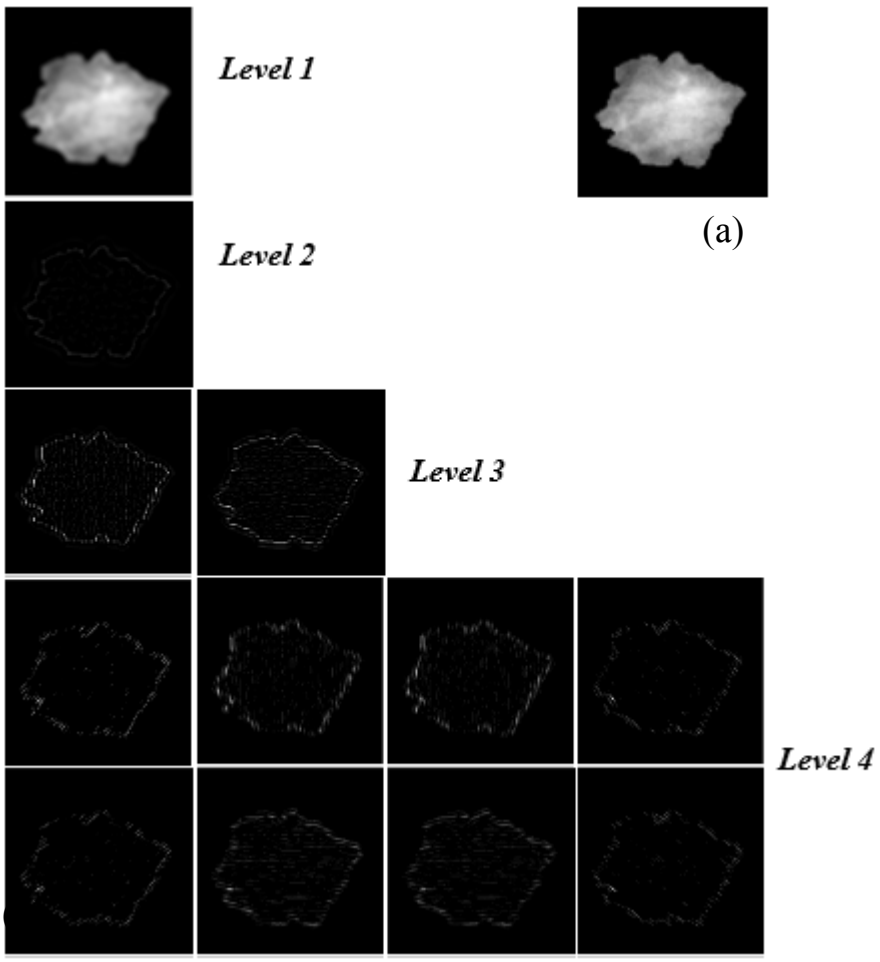

Figure 4.4 Non-sampled contourlet transform of an ROI: (a) ROI sample, (b) four-level decomposition.

Different from the classical CT, all subbands of NSCT have the same resolution. That means, the NSCT coefficients of each subband are in one-to-one correspondence with the original surface in the spatial domain. For feature extraction, a combination of k mean, variance, energy, entropy, skewness and kurtosis parameters from 4-level non-sampled contourlet transform is examined. An example of the NSCT for a mass is shown in Fig. 4.4. The image is decomposed into four pyramidal levels, resulting in one, two and eight sub-bands.

4.2.2. Eig(Hess)-HOG features

HOG is useful for the classification and retrieval of textured breast masses with different shapes. It is computed for each key point from a block. The adjacent area of each key point is partitioned into cells. One-dimensional histogram of gradient orientations is accumulated for each cell. The histogram of all the cells generates the feature [24], [56]. A simple 1-D $[-1; 0; 1]$ mask is used for conventional gradient

computation. In conventional HOG, firstly the grayscale image is filtered with mask to obtain x and y derivatives of image as in Eq. (4.1) and Eq. (4.2). The magnitude and orientation is calculated as in Eq. (4.3) and (4.4).

Eig(Hess)-HOG uses the Hessian matrix instead of the Gaussian derivative filters to compute the eigenvalues of image surface. The Hessian matrix contains more differential information than the conventional gradient. The Hessian matrix of an image is defined as the second-order partial derivative matrix of the gray scale image. The second order differentials provide more accurate analysis in detail about function curves in breast masses [24], [66]. The Hessian matrix (H) of image I for a scale σ is calculated in Eq. (4.19)

$$H_{\sigma}(x,y)=\begin{bmatrix} D_{xx} & D_{xy} \\ D_{yx} & D_{yy} \end{bmatrix}=\begin{bmatrix} I*G_{xx} & I*G_{xy} \\ I*G_{xy} & I*G_{yy} \end{bmatrix} \tag{4.19}$$

where $*$ indicates the convolution operation, D_{xx}, D_{yy}, D_{xy} are the second-order derivative of the image along direction of x, y, xy respectively. G_{xx}, G_{yy}, G_{xy} are the second-order derivative filter of the image along direction of x, y, xy respectively.

The Hessian matrix extracts the principal directions and the principal curvatures in image surface. The eigenvalues (λ_1 and λ_2) of the Hessian matrix are calculated in Eq. (4.20) [24]:

$$\lambda_{1,2}=\pm\sqrt{\frac{\left(I*G_{xx}-I*G_{yy}\right)^2}{4}+\left(I*G_{xy}\right)^2}+\frac{I*G_{xx}-I*G_{yy}}{2} \tag{4.20}$$

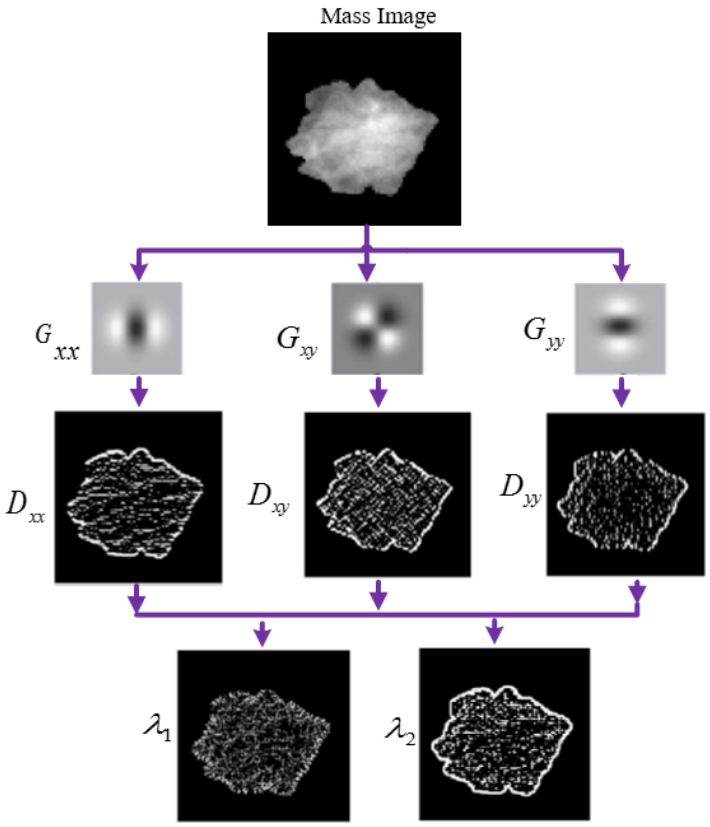

Figure 4.5 Computation of eigenvalues of the hessian matrix for a breast mass.

The gradient magnitude and orientations were computed by using the eigenvalues λ_1 and λ_2 as in Eq. (4.21) and Eq. (4.22):

$$I_{\theta gradient} = \sqrt{(\lambda_1)^2 + (\lambda_1)^2} \tag{4.21}$$

$$\theta = \arctan\left(\frac{\lambda_2}{\lambda_1}\right) \tag{4.22}$$

The number of possible orientation bins is referred to as N_o and the number of cells for direction is referred to as N_c. We set the parameters of the descriptor to $N_c = 4$ cells and $N_o = 8$ bins resulting in a total of N_o x $N_c^{\,2} = 128$ elements in a HOG feature. Fig. 4.5 demonstrates the computation of eigenvalues of the Hessian matrix for mass ROI.

In addition as shown in Fig. 4.6, a 9-D shape feature and a 7-D mass feature are extracted which representing the mass boundary and the average contrast, smoothness, orientation, uniformity, entropy, perimeter and circularity [18]. Finally, a 6-D texture feature representing the energy, correlation, entropy, inverse difference moment, contrast and homogeneity is obtained from the GLCM.

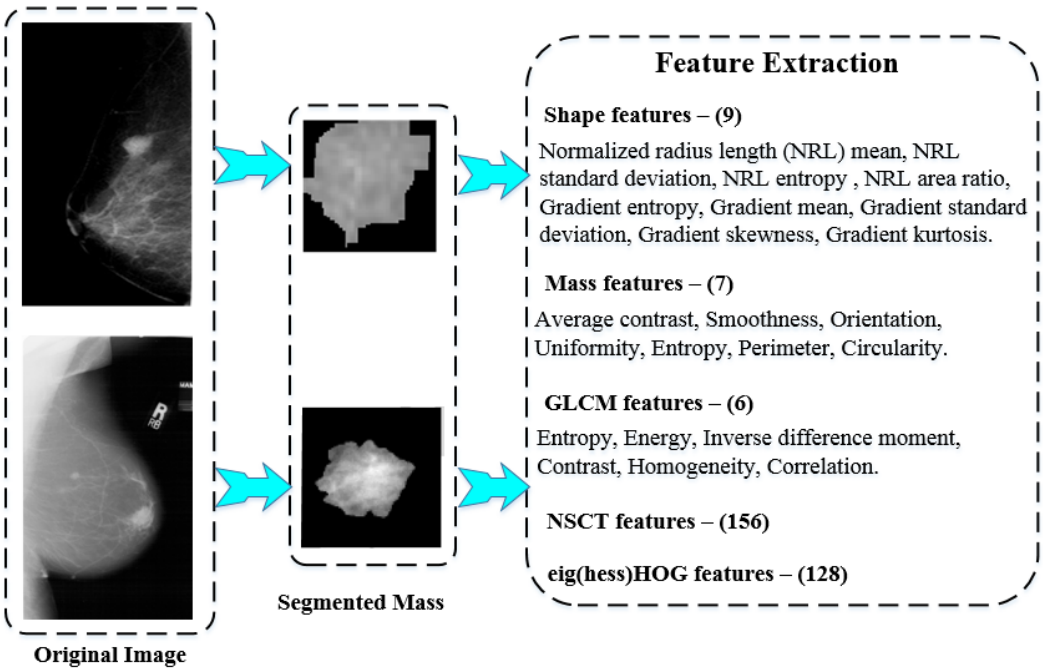

Figure 4.6 Feature extraction stage with an example mammogram

4.3. Digital Mammography Feature Extraction Framework III

In this framework, deep feature based framework is proposed. By using mammographic patches dataset, fine-tuning operation is applied on the trained CNN network. The obtained network is used for extracting features in the next procedures. Then, high-level features extracted from fc7 layer of trained model and f_1 feature set are used for training 2 ELM classifiers. Finally, the outcomes of these two classifiers are combined. Owing to simulating the structure of human brain, the deep CNN model, it has a great capability of simulating multiscale impressions of physician's brain. And the proposed decision mechanism has a better simulation of doctors' thought structure in the diagnosis.

There is not any sufficiently large training set in the area of breast cancer detection. In order to accomplish this problem, our CNN is trained on ILSVRC [53] which is a dataset containing more than 1 million labeled natural images first. However, the natural images in dataset are in RGB format and not in relevance with gray level mammography images. So, GPU processing and time consuming increase. Therefore, the dataset is transformed into gray scale. Our feature description network is inspired by [67], [68].

We applied [69] for training strategy. It is a supervised learning process, the learning rate was initialized at 0.01. The training is continued 100 iterations for the natural images. Then learning rate on mammography images was initialized at 0.00001 and the second stage was executed 100 iterations.

Main details of the CNN are shown in Tables 4.3 and 4.4. Then fine-tuning operation which uses the already learned model is applied, regulated according to the architecture, and resumed training from the already learned model weights on mammography images. Specifically, breast dataset in this thesis consists of 600 mass images of 227×227 [52]. According to the successful application of [70], mammography images are rotated angles of 45°, 90°, 135°, 180°, 225°, 270° and cropped 2×2 for augmentation of dataset 28 times. The main structure of AlexNet is shown in Fig. 4.7.

We utilized SGD [72] for optimization of the network. It is very simple and effective in the training process. The training point at each cycle is selected randomly. After that, derivative of the loss term is computed and parameters are updated by moving the local minima in the direction of the gradient. A CNN model consists of several of blocks above in the form of directed acyclic graph (DAG). The DAG is simplified as Fig. 4.8, where each output of corresponding block $(f_1; f_2; f_3 \ldots; f_l)$ is described as $(x_1; x_2; x_3 \ldots; x_l)$, and the parameters of each layer was $(w_1; w_2; w_3 \ldots; w_l)$. So the derivative of w_l is expressed as follows.

$$\frac{dz}{d(vec\,\mathbf{W_1})^T} = \frac{dz}{d(vec\,\mathbf{W_L})^T} \frac{d\,vec\,\mathbf{W_L}}{d(vec\,\mathbf{W_{L\text{-}1}})^T} \cdots \frac{d\,vec\,\mathbf{W_{l+1}}}{d(vec\,\mathbf{x_l})^T} \frac{d\,vec\,\mathbf{W_l}}{d(vec\,\mathbf{W_l})^T} \qquad (4.23)$$

To measure the performance of CNN model, the loss of network is computed by the cross entropy between the predicted probability distribution and the ground truth distribution. For obtaining optimal results from fine-tuning operation, the learning rate was reduced gradually.

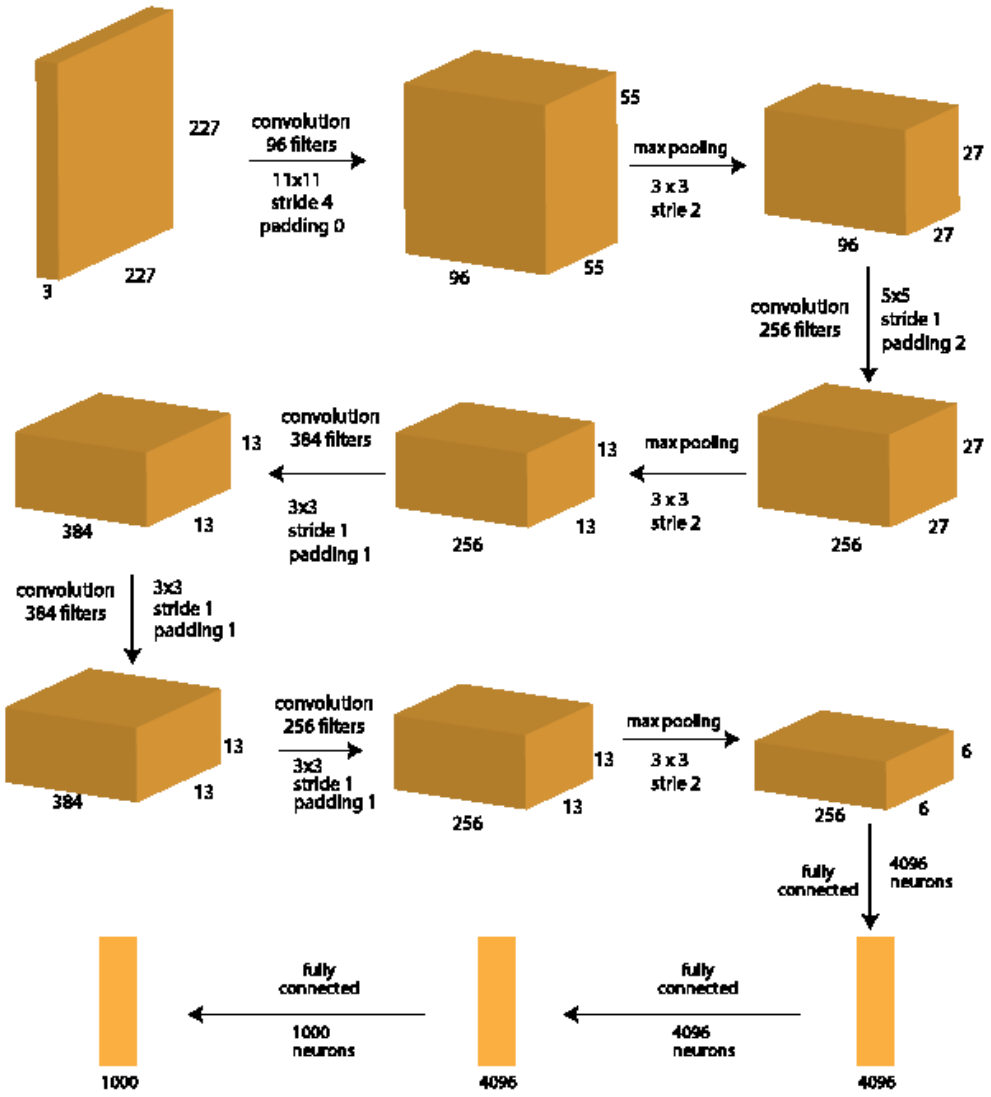

Figure 4.7 Main structure of AlexNet [71]

The hierarchical features can be extracted with various methods of different layers by the fine-tuned CNN. In this thesis, we applied the hierarchical features that is the output of CNNs layers.

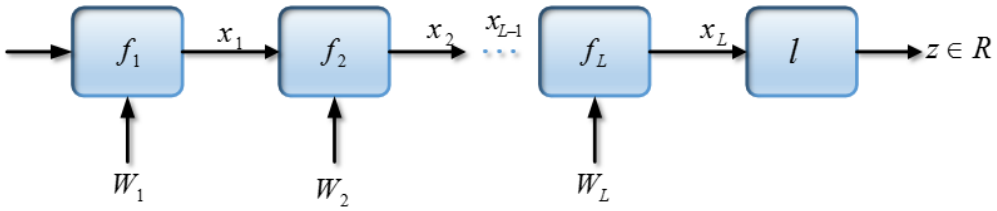

Figure 4.8 The DAG expression of CNN.

5. BREAST MASS CONTOUR SEGMENTATION

The most challenging aspect in developing any CAD based systems for mammograms is to segment the suspicious mass which is often hidden in dense breast tissues. Since a cancerous region might be typically represented by local-oriented patterns, accurately segmenting it is an important first step for the effective performances of the successive feature extraction, similarity matching and classification steps in our CBIR development process. Hence, a large number of segmentation methods have been proposed in the literature for the detection of breast masses, such as adaptive region growth [73], multi-layer topographic region growth algorithm [74], active contour (snake) modeling [75], level set algorithm [76], dynamic programming [77] etc. However, due to the limitation of benchmark evaluation and testing datasets to compare the performances, it is difficult to find the most robust and effective method in this domain till now.

In this thesis, we have used two different segmentation methods. First segmentation method is based on Marker-controlled watershed segmentation (MCWS). Second method utilizes Graph-Based Visual Saliency (GBVS).

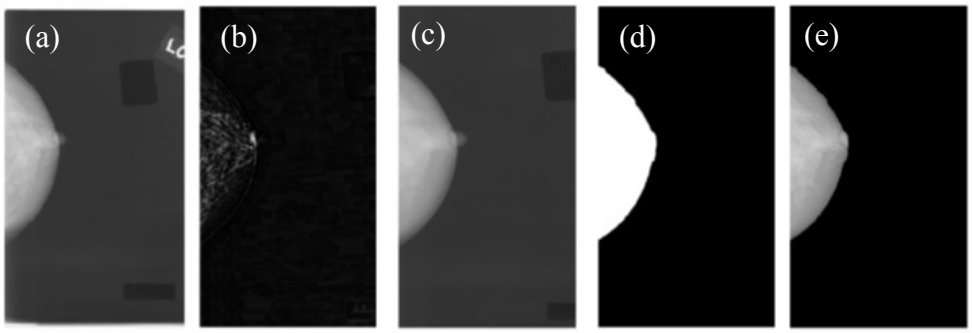

Figure 5.1 Outputs of artifact elimination: (a) mammographic image of CC view, obtained from case 0320; (b) image obtained by top-hat morphological operation; (c) image resulting from subtraction operation; (d) Otsu's thresholding applied image; (e) image without artifacts obtained from the multiplication step.

In this method, image pre-processing is performed with the top-hat morphological operation and a marker-controlled watershed segmentation algorithm is applied on images with no background artifacts for effective mass detection.

5.1.1. Image pre-processing

Several factors can affect the segmentation performance such as artifacts and personal patient information. The aim of pre-processing is to enhance the image visibility by removing artifacts and undesired distortions, stretch the intensity between breast region and background, and finally segment the breast area from background. To remove artifacts on mammograms and enhance the segmentation performance, a top-hat morphological operation is performed at first (Fig. 5.1(b)) which is the difference between an input image and its opening. The top-hat morphological operation helps to extract small elements and details from given images. Mathematical expression of the top-hat morphological operation is given in Eq. (5.1), (5.2), (5.3), (5.4):

$$TH_{top} = \max[0, I(x,y) - (I \circ se)(x,y)], \tag{5.1}$$

$$(I \circ se)(x,y) = [I \ominus se(x,y) \otimes se](x,y) \tag{5.2}$$

$$(I \ominus se)(x,y) = \max[I(x-k_1, y-k_2), (k_1,k_2) \in se] \tag{5.3}$$

$$(I \otimes se)(x,y) = \max[I(x+k_1, y+k_2), (k_1,k_2) \in se] \tag{5.4}$$

Where, $I(x,y)$ is the mammogram and se is the structuring element, both specified over the set Z^2, and (k_1,k_2) is a pair of pixels of the se. After this step, a subtraction was carried out between the resulting and the original image (Fig. 5.1(c)). Then, Otsu's thresholding is applied to the image resulted from subtraction (Fig. 5.1(d)). Mathematical expression is given in Eqs. (5.5) and (5.6):

$$\sigma_\omega^2(t) = \omega_1(t)\sigma_1^2 + \omega_2(t)\sigma_2^2 \tag{5.5}$$

$$\sigma_b^2(t) = \sigma^2 - \sigma_\omega^2(t) = \omega_1(t)\omega_2(t)[\mu_1(t) + \mu_2(t)]^2 \tag{5.6}$$

where $\omega_1(t)$ and $\omega_2(t)$ denotes the separation probabilities for the regions respectively, t is the threshold value, σ_1^2 and σ_2^2 are the variances of each class, and μ_1 and μ_2 are the mean values of each class. Finally, a multiplication was carried out between the Otsu's output and the original one which results images with no background artifacts as shown in Fig. 5.1(e).

5.1.2. Marker-controlled watershed segmentation (MCWS)

Watershed transform is an edge-based segmentation method. In topography, a watershed line represents where a drop of water will fall into particular region. This idea is profitably utilized in the digital images. The image gradient can be considered as landscape. The low gradient values represent valleys while the peaks having high gradient values represent the edges [78]. The major disadvantage of the method is the over-segmentation because of the too many local minima's. Due to drawbacks of over-segmentation, marker-controlled watershed transformation has been proposed [79]. This method is robust, stable and flexible to segment objects with closed contours such as breast masses.

This segmentation procedure consists of the following five steps:

1. ***Computation of a segmentation function:*** This is an image whose dark regions are the objects one tries to segment. To generate the segmentation function, varied operations can be carried out to input image. In this study, gradient magnitude is applied to the input image. To compute the gradient magnitude, the Sobel filter and some simple arithmetic are used. At the borders of the objects, the gradient value is high and inside the objects the gradient value is low. The watershed transform can be carried out directly on the gradient magnitude but it causes over segmentation. The additional preprocessing such as the marker computations is required.
2. ***Computation of internal markers:*** Varied methods can be carried out to find the internal markers. The morphological operations called opening-by-reconstruction and closing-by-reconstruction are used to clean up the images.
3. ***Computation of external markers:*** Preferably, external markers must be close to the edges of the objects. For this purpose, background is thinned by computing the skeleton from the "influencing zones" of the foreground of the last image.
4. ***Modification of the segmentation function:*** Each marker denotes a specific place within the segmentation function to force that region to be a global minimum of the image by using the minima imposition technique. That means, the modified segmentation function (gradient image) only has regional minima in the locations of the markers.
5. ***Computation of the watershed transform:*** At last, the watershed transformation is carried out to the modified segmentation function to obtain the mass boundary.

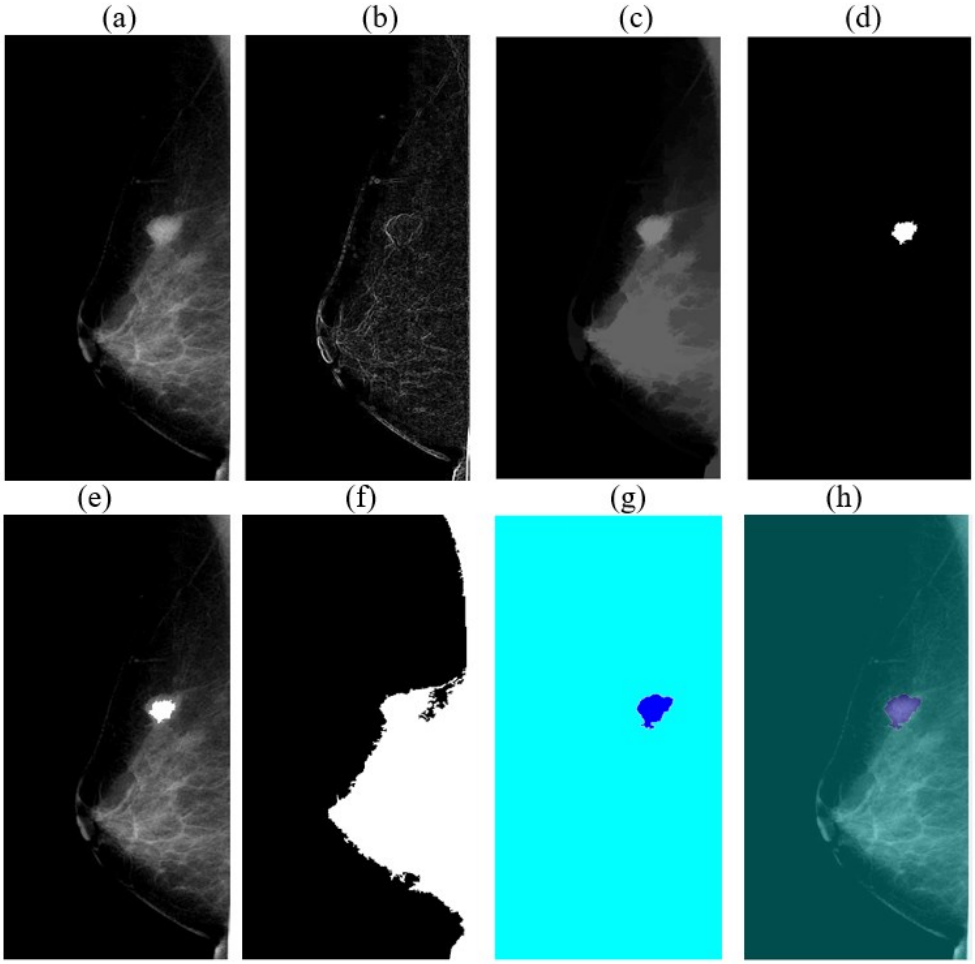

Figure 5.2 (a) Initial image, (b) Gradient magnitude image, (c) Opening-closing by reconstruction image, (d) Regional maxima of opening-closing by reconstruction image, (e) Regional maxima superimposed on original image, (f) Thresholded opening-closing by reconstruction image (g) Colored watershed label matrix (h) Lrgb superimposed transparently on original image.

Fig. 5.2 illustrates the various steps involved in this process. In Fig. 5.2(e), the foreground markers, the background markers and the segmented object boundaries superimposed on the original image. This visualization illustrates how the locations of the foreground and background markers affect the result.

5.2. Visual Saliency Based Segmentation

The breast anatomy has a complicated structure because of the presence of pectoral muscles and the different mass density. Although it is easy to analyze breast tissues without getting confused with pectoral muscles for a radiologist, it is always difficult to distinguish between pectoral muscles and mass for an automatic method in a CAD

system. For that reason, pectoral muscles are removed usually before the segmentation. However, automatic segmentation of pectoral muscle is a troublesome process and also an additional workload in analysis of mammography images in CC view which are generally without pectoral muscles.

In this thesis, a Graph-based visual saliency (GBVS) is utilized for segmentation by applying thresholding on the saliency map which does not require the removal of pectoral muscles to detect the breast masses. It has the ability of generating an output showing concentrated saliency maps in the appropriate image regions where the value of an image pixel location corresponds to the saliency of that pixel with respect to the neighbors. The usefulness of saliency models in cases where some structures are implicit with respect to the image such as pectoral muscles in mammograms is demonstrated in [80]. It is also experimentally shown that the GBVS yields the best results for mass detection from screening mammograms [81].

The GBVS calculates the saliency of a region with respect to its local neighborhood using directional contrast. In mammography images, it has been monitored that the contrast of mass containing regions is significantly different from the remaining breast tissue. As discussed earlier, the mass encircled by dense tissues is difficult to recognize, whereas the directional contrast with respect to the local neighborhood helps in identifying such masses along with the masses present in fatty regions. The computation of saliency map consists of following stages: Firstly, to differentiate mass from the neighboring regions in contrast, feature maps are computed from contrast values along four different orientations of 2D Gabor filters (0°, 45°, 90°, and 135°). Then, activation maps are computed as the balanced distribution of a Markov chain which is obtained using the initial feature maps [25], [82]. The balanced distribution denotes higher weights only for the edges present in salient regions. The Ergodic Markov chains are modeled on a fully connected directed graph obtained from feature maps. Weighted connections are used to create the graph. It is created by connecting nodes in a feature map. The directed edge node (i, j) to node (k, l) weight is assigned in the graph.

$$w((i,j),(k,l)) \stackrel{A}{=} D \cdot F(i-k, j-l), \tag{5.7}$$

Where $F(a,b) \stackrel{A}{=} \exp(-\frac{a^2+b^2}{2\sigma^2})$

$$D \overset{A}{=} \left| \log\left(\frac{M(i,j)}{M(p,q)}\right) \right| \tag{5.8}$$

where $M(i,j)$ denotes a node in the feature map and σ is set to 0.15 times the image width.

Due to the fact that activation maps lack the accumulation of weights, a normalization of activation map is performed to avoid uniform saliency maps. Activation maps are normalized using a similar approach as used in the previous step. Markov chains are computed from the activation maps. The function D in Eq. (5.9) maps to the value at location (k,l) in activation map. The value of the parameter σ is 0.06 times the image width [83].

$$D \overset{A}{=} A(p,q) \tag{5.9}$$

where *A(p,q)* represents a node in the activation map. In final stage, normalized activation maps are combined using the sum rule to obtain the saliency map. Once the saliency map is computed, a threshold is empirically selected to obtain the optimal size ROIs. Fig. 5.3 illustrates some examples of saliency maps generated from pre-processed images and ROI segmentation from the saliency maps.

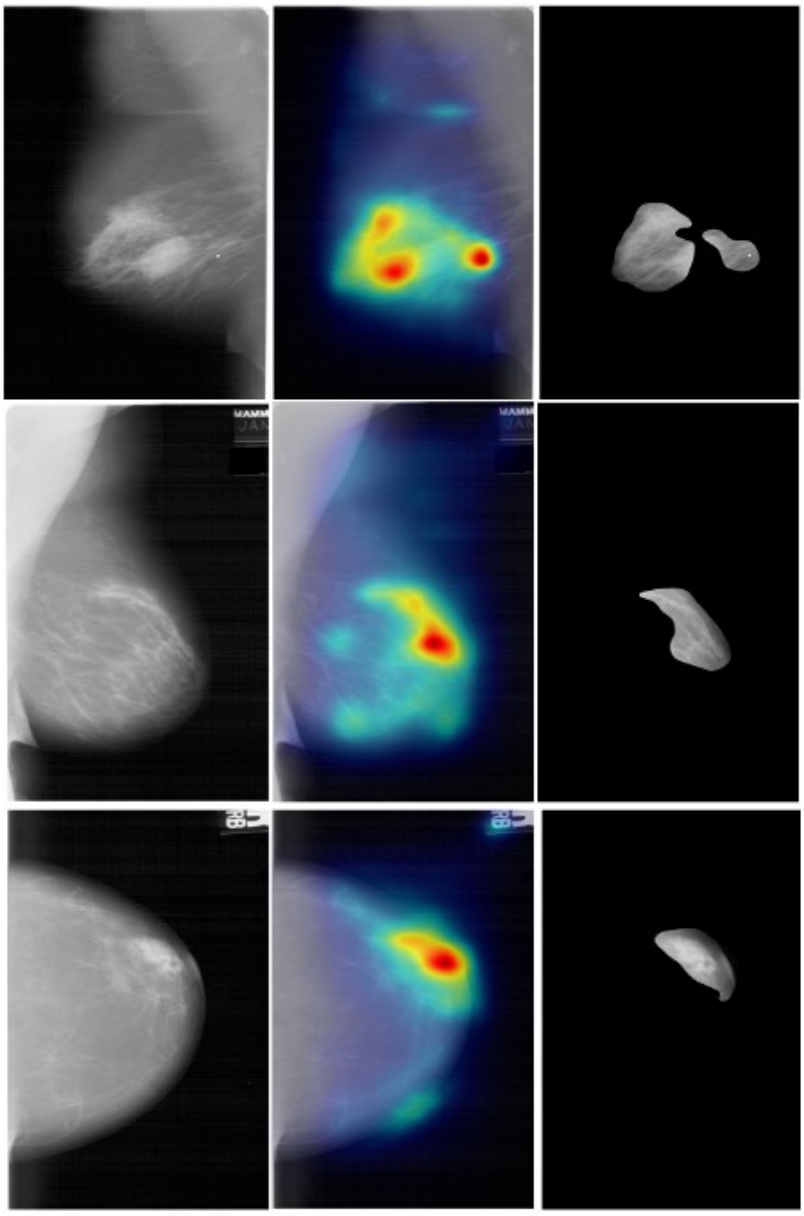

Figure 5.3 Saliency map generated from enhanced image and suspicious regions obtained after thresholding.

6. CONVOLUTIONAL NEURAL NETWORKS

In recent years, deep learning has shown quite robust feature learning capabilities and succeed noticeable performance in computer vision (CV) [84] and medical image analysis [85]–[87] applications. Convolutional neural networks (CNN) is a type of deep learning method. CNN has generated quite good results on application of visual image analysis. Among deep learning methods, CNNs are being remarkably popularly in vision related applications such as semantic segmentation, object detection , face recognition and image classification [68], [88], [89].

CNNs were essentially proposed by LeCun [90] for a hand written digit recognition task. Thenceforth it has been utilized on ImageNet like datasets that contains rich images classes. It has succeeded state-of-the-art performance on the ImageNet Large Scale Visual Recognition Challenge [53].

To develop a machine learning framework for carrying out a certain task, remarkable field expertise, attentive and satisfactory study are required in conventional machine learning. The classical machine learning methods cannot process the data in raw format. However, deep learning methods are representation learning methods. The machines can be supplied directly with raw data and discover the representations required for detection or classification automatically [91]–[93] in representation learning. In these systems, raw data is given to input of the system and it goes through simple non-linear transformations. By passing through the number of transformations, it is possible to learn very complex functions [92], [93].

CNN is also used in medical field. For instance, it is used for restoration and segmentation of electron microscopy images in [94]–[96]. Also, it is used for detection of mitosis in breast histology images in [97], [98] and segmentation of infant brain tissue images in [69]. Consequently, it is seen that CNN based methods considerably outperforms conventional methods.

With the development of powerful computers, training of networks became 10x or 20x times faster. Also, availability of large datasets makes it possible to train deep architectures in a supervised manner easily, so it leads to state-of-the-art achievements in the literature [99].

CNNs are different from classical neural networks in terms of the form and functions of layers. In classical networks, layers are one dimensional and neurons in these layers are fully connected to each other. CNNs suggest the use of locally connected neurons instead of using fully connected neurons. CNNs are fed by multi-dimensional arrays which maintain neighborhood relation in data. In Fig. 6.1 general architecture of regular neural networks (MLP) is shown. The ability of the CNN is encouraged with its use in many fields from the 90s to today. AT&T check reading, Microsoft's OCR and handwriting recognition systems are some of the first examples of CNN. Also, Google utilized CNNs to detect license plate and face to protect privacy in StreetView.

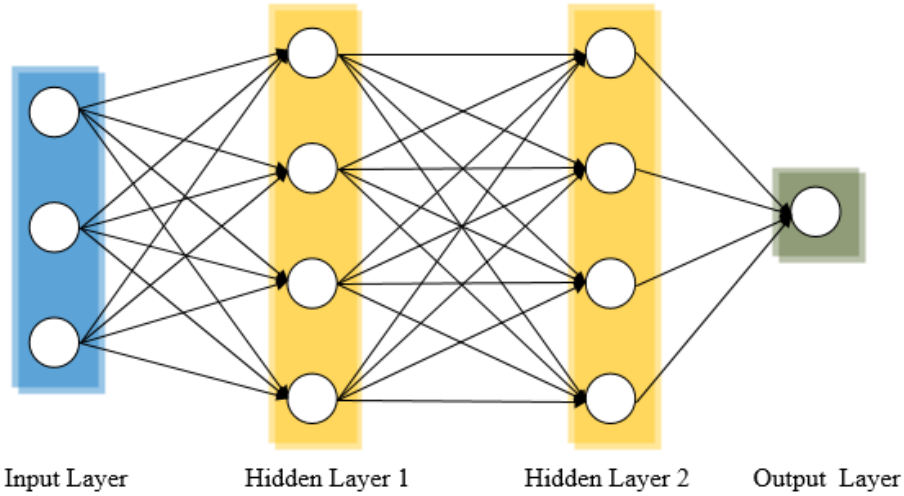

Figure 6.1 Regular neural network structure

Input of the CNNs are generally three dimensional images and the output layer gives the class scores of the input images. CNNs consist of four sublayers, namely a convolution sublayer, a pooling sublayer, normalization sublayer and a fully connected sublayer. These layers are stacked on top of each other to construct the CNN structure. The network capacity can be tuned by selection of the number of layers or number of and size of filters.

6.1. Convolution Sublayer

This layer type is the core of CNN structure. A convolutional layer consists of multiple feature maps which consist of the collection of neurons. This layer convolves input with filters and adds bias which is different for each filter.

The input image (I) of dimensions $nY \times nX \times nC$, in which nY is the number of rows of the image, nX is the number of columns of the image, and nC is the number of channels of the image. The input image (I) is convolved with rows and columns flipped filters $(W)\,\tilde{W}$ with dimensions $nfY \times nfX \times nC \times nf$, in which nfY is the number of rows of the filter, nfX is the number of columns of the filter, nC is the number of channels of the filter which is the same as the number of channels of the image, and nf is the number of the filter. The discrete definition convolution of 2D image I and W is given by [69]:

$$o[m,n] = I[m,n] * W[m,n] = \sum_{u=-\infty}^{\infty} \sum_{v=-\infty}^{\infty} I[u,v] * W[m-u, n-v]. \tag{6.1}$$

Bias b of size nf is added after convolution. Output of this operation is matrix a which is in dimensions of $naY \times naX \times nf$ where naY is the number of columns in resulting image, which is equal to $nY - nfY + 1$, naX is the number of rows in the resulting image which is equal to $nX - nfX + 1$, and nf is the number of channels of the resulting image which is equal to number of filters. In Fig. 6.2, input has the size of $5 \times 5 \times 3$. Input is padded with 0s of width $wp = 1$ and height $hp = 1$. The number of feature maps to be learned is 2. The size of filter is $3 \times 3 \times 3 \times 2$. The stride parameter is 1 for both width and height. The feature map h_k, which is learned by the filter k, is determined by the weights W_k and bias b as follows:

$$h_k = f\left(W_k * x + b\right) \tag{6.2}$$

, where f is an activation function. The volume of output should be:

$$d_0 \times \left(\frac{w_i - w_f + 2w_p}{w_s} + 1\right) \times \left(\frac{h_i - h_f + 2h_p}{h_s} + 1\right) \tag{6.3}$$

The number of parameters to be learned should be:

$$\left(w_f \bullet h_f \bullet d_f + 1\right) \bullet o_d \tag{6.4}$$

The output has size of $3 \times 3 \times 3 \times 2$. The number of parameters to be learned is $(3 \times 3 \times 3 + 1) \times 2 = 56$.

Convolution sublayer performs the same filter to various locations. Since the distribution of data is uniform across different locations, implementation of the same

filter to various locations in the images is pretty reasonable especially for medical images

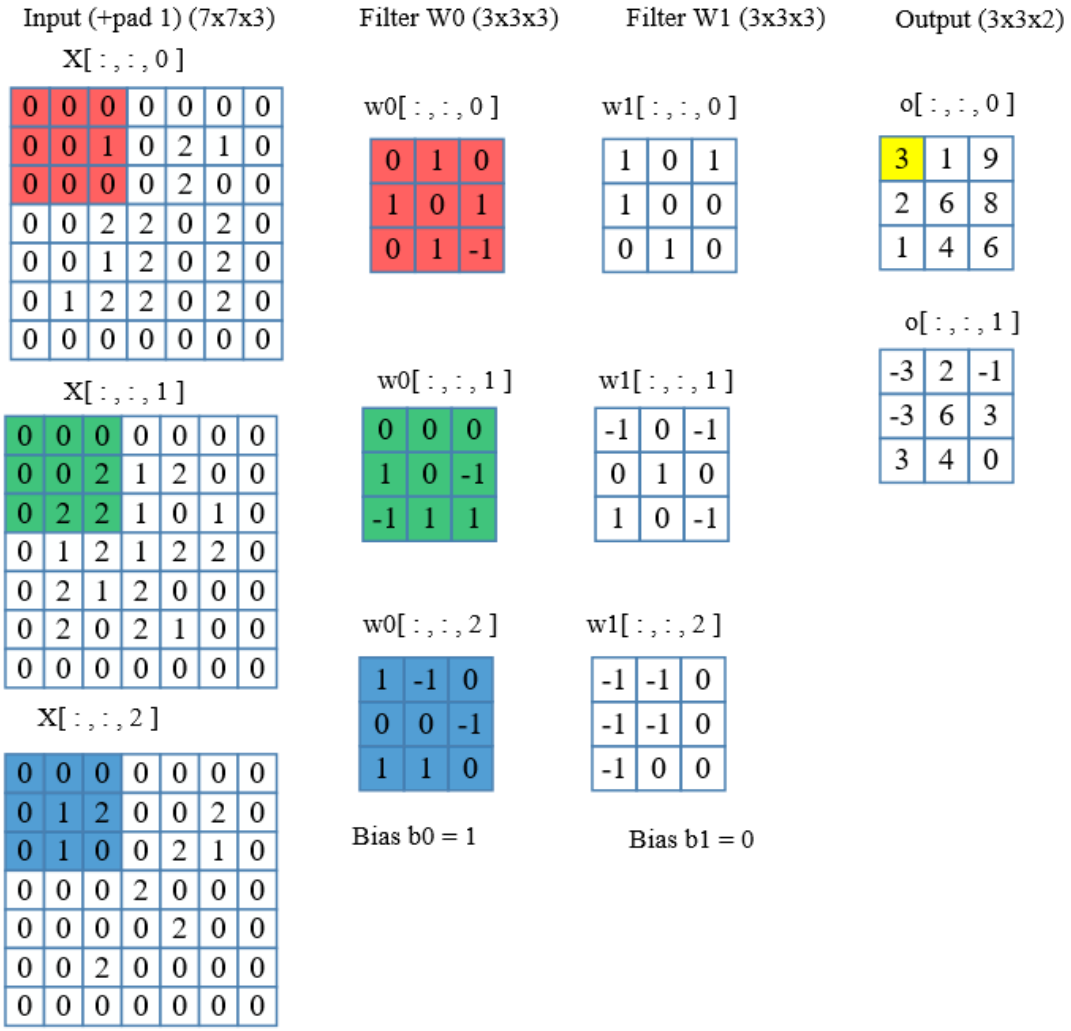

Figure 6.2 Convolutional layer.

6.2. Pooling Sublayer

Pooling operation summarizes the outputs of spatially close units of feature map. It is used to transfer the most discriminative features to next layer for providing invariance of significant patterns. The mean, max and L2–norm operations are the most common examples. Moreover, by utilization of stride more than one row or column decreases the dimension of data in the next layer. Thanks to reduction of dimension, the computation time and number of parameters in the network decreases, so over-fitting is avoided. Furthermore, pooling makes the system invariant to small transformations since the pooling operates on a region. Eq. (6.5) and (6.6) shows the average and maximum pooling, respectively:

$$h(x,y,z)=\frac{1}{n}\sum_{i_z,i_y\in N}u(i_z,i_y,z) \tag{6.5}$$

$$h(x,y,z)=\max(\ u\ (i_z,i_y,z))\ :\ i_z,i_y\in N \tag{6.6}$$

The size of window (F) and the stride (S) are the two parameters of the pooling operation. Stride determines the coefficient of downsampling in width and height dimension. Usually, max pooling operation is utilized since it outperforms the other options like average pooling. Moreover, the hyperparameters also have some well-known and commonly used values in practice: the F=2, S=2 or F=3, S=2 pairs are chosen. The first one, F=2, S=2 is known as non-overlapping pooling while the second one, F=3, S=2, is called as overlapping-pooling which is claimed to avoid overfitting in [68]. Non-overlapping and overlapping max pooling examples are shown in Fig. 6.3.

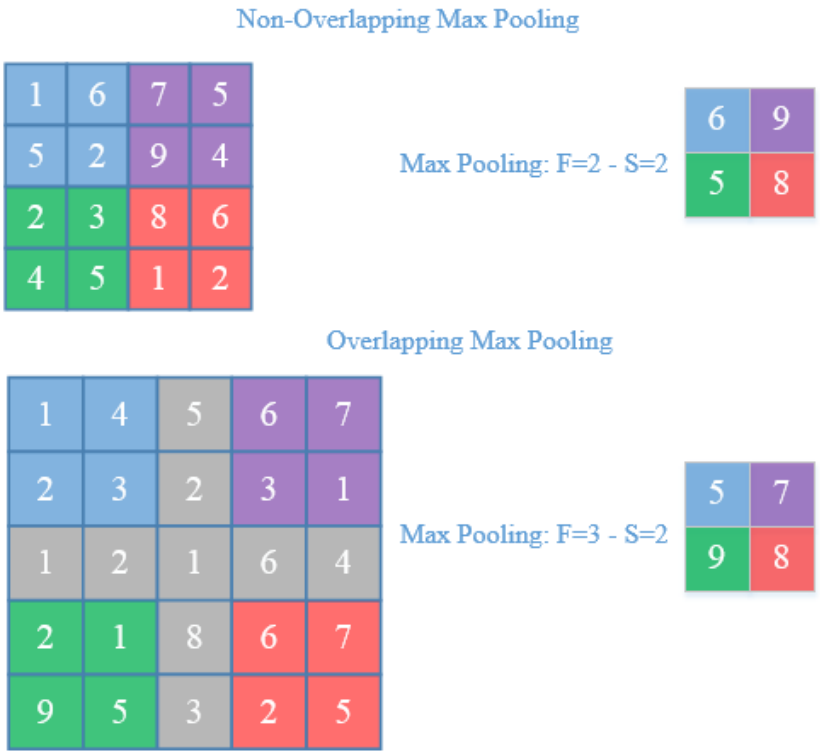

Figure 6.3 Non-overlapping and overlapping max pooling examples

6.3. Rectified Linear Unit (ReLU)

Rectified linear function, with Eq. (6.7) and shown in Fig. 6.4, improves the discriminative power of the network [100].

$$relu(a) = \max(0, a) \tag{6.7}$$

6.4. Normalization Layer

Normalization layer is preferred after ReLU function for its ability to increase generalization. In this layer, neurons at the same location belonging to different convolution kernels, are normalized. However, there exist a common thought that the effect of normalization layer is so small or none, so the usage of normalization layers in state of the art networks are very limited or none, e.g. [101].

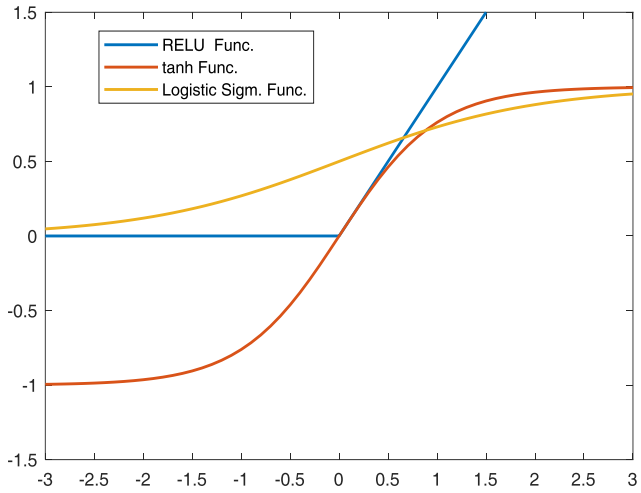

Figure 6.4 Non-linearty functions (a) Logictic sigmoid function (b) Hyperbolic tangent sigmoid function (c) Rectified linear function

6.5. Dropout

Dropout operation [84], [102] is used to reduce overfitting and extract more robust features. As seen in Fig. 6.5, the node to be dropped out has a probability p to remove temporarily. This prevents nodes from memorizing. In dropout operation, a layer with n nodes is considered as $2n$ possible neural networks. In testing process, all nodes are not going be dropped out and their weights will be multiplied by p. With the help of this, $2n$ networks are combined into one neural network. Dropout operation is implemented only to fully connected layers except the last layer. It is not implemented to convolutional layers or pooling layers. Furthermore, a cross-channel normalization operator is also applied at each spatial location as shown in Fig. 6.6.

- Sigmoid Function

$$f(z) = \frac{1}{1 + \exp(-z)} \tag{6.8}$$

$$f'(z) = f(z)(1 - f(z)) \tag{6.9}$$

$f : \Re \mapsto [-1, 1]$

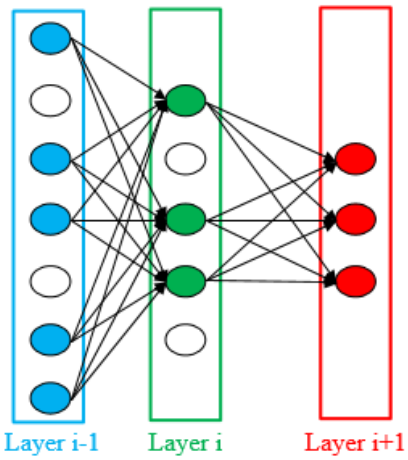

Figure 6.5 Dropout operation.

- Hyperbolic Tangent (tanh)

$$f(z) = \tanh(z) = \frac{e^{z} - e^{-z}}{e^{z} + e^{-z}} \tag{6.10}$$

$$f'(z) = 1 - f(z)^2 \tag{6.11}$$

$f : \Re \mapsto [-1, 1]$

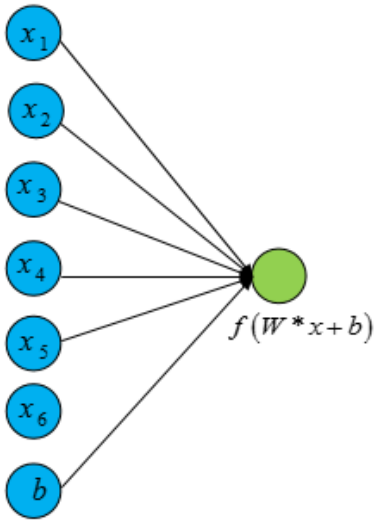

Figure 6.6 Activation function applied to a neuron.

7. EXPERIMENTAL RESULTS

For classification of breast masses as either normal and abnormal (two-class separation) or normal, benign, and malignant cases (three-class study), we used SVM and ELM classifiers for excellent generalization performance and little human intervention.

7.1. Experiment design

In our experiments, ten fold cross validation (CV) is used in experimental design. The SVM learning approach was examined with the Gaussian radial basis function (GRBF) (r = 2, C = 100). The overall performance of a classifier is guaranteed by a 10-fold CV in all evaluation indices.

To measure the performance of proposed classification approaches in different feature spaces, the sensitivity and specificity are computed for each confusion matrix. The accuracy, sensitivity and specificity parameters are employed for the performance evaluation of our classification approaches.

The retrieval effectiveness is evaluated with the PR graph. It is frequently used in information retrieval. In our experimental design, each image in the testing dataset is served as a query image. The performances of the two image categories (e.g., normal and abnormal) and the three image categories (benign, malignant, normal) are compared based on the PR graphs.

7.2. Experimental Results of Proposed Framework I

In first proposed framework, 3 different feature vectors have been proposed. The combinations of geometric features of mass, histogram features of the HOG and CoHOG is used for feature extraction. Also, SVM based CBIR system is proposed.

7.2.1. Classification Results:

Table 7.1 Classification performance of ***ghsthog*** and ***ghstcohog*** for the 2 class.

	ghsthog			***ghstcohog***		
Fold #	Acc(%)	Sens(%)	Spec(%)	Acc(%)	Sens(%)	Spec(%)
Fold 1	90.43	89.71	91.21	90.45	90.92	92.64
Fold 2	94.56	93.17	97.26	86.43	84.37	92.48
Fold 3	95.68	94.84	90.16	92.25	91.86	91.66
Fold 4	93.24	89.61	95.35	91.31	88.34	90.26
Fold 5	95.76	90.63	91.24	93.27	90.23	88.87
Fold 6	90.32	91.75	90.52	87.29	91.92	93.72
Fold 7	89.36	93.61	92.71	92.13	93.54	90.46
Fold 8	92.27	94.35	94.32	88.12	90.62	91.43
Fold 9	91.44	94.68	91.17	91.86	92.43	92.54
Fold 10	90.49	90.65	96.26	90.29	87.07	86.04
Ave	92.35	92.30	93.02	90.34	90.13	91.11

From Table 7.1 and 7.2, the mean classification accuracy of SVM classifier for **ghsthog** and **ghstcohog** features are 92.35% and 90.34% respectively. Table 7.1 shows the results for 2 class study and Table 7.2 shows the results for 3 class study. From Table 7.3 the average classification accuracy of SVM classifier for **ghsthogcohg** feature is 93.83% and 91.90% for 2 and 3 class study respectively. Table 7.3 shows the results for both 2 and 3 class study.

To further verify the effectiveness of the proposed methods, the sensitivity and specificity of all the methods are also computed and listed in Table 7.1, 7.2 and 7.3. The sensitivity and specificity values express alternative measure of the diagnosis accuracy. From Tables 7.1 and 7.2, it is seen that the ***ghsthog*** is more effective than ***ghstcohog*** method for both two and three class studies. From Tables 7.3, it can be seen that the ghsthogcohg is most powerful method for both two and three class studies.

Table 7.2 Classification performance of ***ghsthog*** and ***ghstcohog*** for the 3 class.

	ghsthog			***ghstcohog***		
Fold #	Acc(%)	Sens(%)	Spec(%)	Acc(%)	Sens(%)	Spec(%)
Fold 1	91.86	91.23	90.75	87.27	92.20	90.21
Fold 2	92.36	88.34	87.37	90.41	91.36	86.15
Fold 3	89.47	90.46	88.29	88.82	92.51	92.54
Fold 4	93.07	92.72	92.75	92.29	91.23	89.24
Fold 5	90.85	91.37	91.31	93.34	90.76	90.53
Fold 6	91.19	85.91	94.43	91.96	86.96	89.18
Fold 7	87.23	84.82	90.71	90.34	90.41	87.83
Fold 8	94.61	90.57	91.62	84.24	82.81	94.17
Fold 9	90.52	92.14	92.19	92.12	89.49	97.65
Fold 10	86.84	96.74	93.74	83.51	84.57	91.00
Ave	90.80	90.43	91.31	89.43	89.23	90.85

Table 7.3 Classification performance of ***ghsthogcohg*** for the 2 and 3 classes.

	2 class			***3 class***		
Fold #	Acc(%)	Sens(%)	Spec(%)	Acc(%)	Sens(%)	Spec(%)
Fold 1	94.32	91.04	92.53	90.34	90.31	92.86
Fold 2	84.21	94.53	94.76	92.45	89.51	95.24
Fold 3	90.53	96.62	97.46	88.56	92.34	89.19
Fold 4	98.12	90.83	98.53	95.38	93.54	90.87
Fold 5	95.68	92.74	93.37	91.49	91.67	93.43
Fold 6	98.35	90.31	99.43	90.52	90.77	96.92
Fold 7	88.27	95.48	98.24	95.58	87.86	90.59
Fold 8	95.07	92.42	91.23	87.85	92.64	94.17
Fold 9	97.34	86.64	92.25	92.49	90.28	90.34
Fold 10	96.41	93.39	93.20	94.34	89.28	96.09
Ave	93.83	92.40	95.10	91.90	90.82	92.97

7.2.2. Retrieval Results

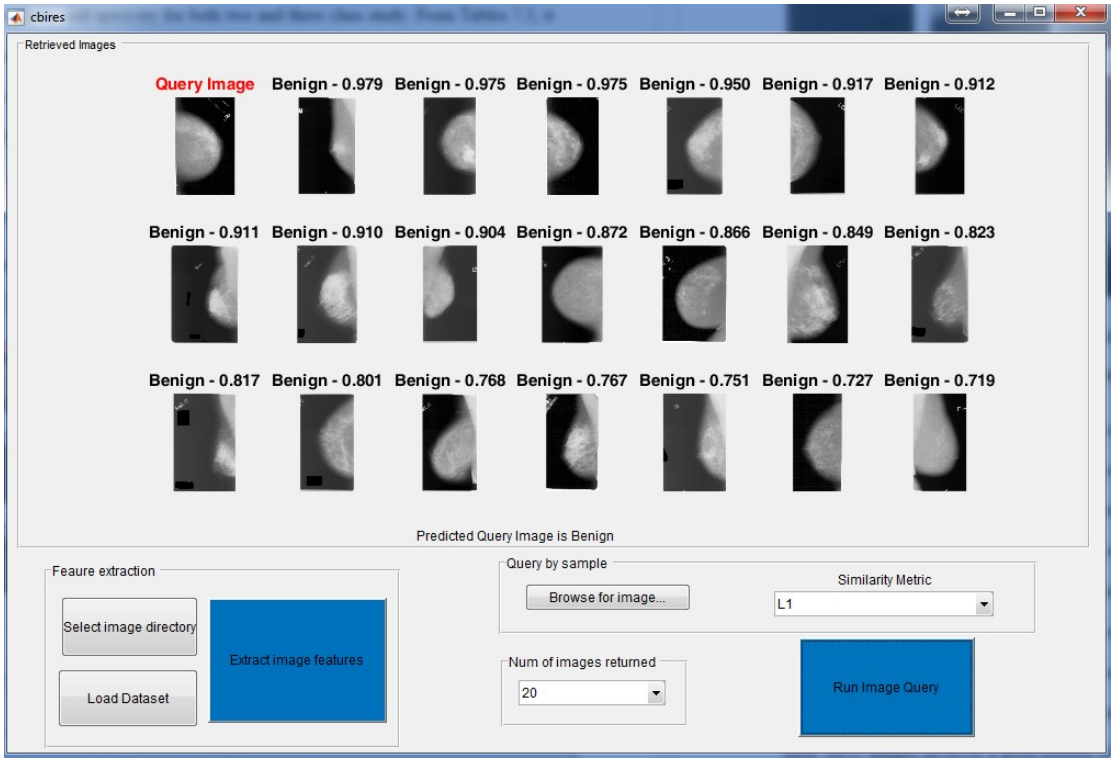

Figure 7.1 The user interface of our developed software.

Fig. 7.1 demonstrates the user interface of our developed software tool for mammographic content based image retrieval. Fig. 7.2 indicates a sample of a benign query image and retrieved images based on ***ghsthogcohg*** features. Except for retrieved image 6, all the retrieved images are benign. Another retrieval instance of cancer type query is demonstrated in Fig. 7.3. All the retrieved images are cancer.

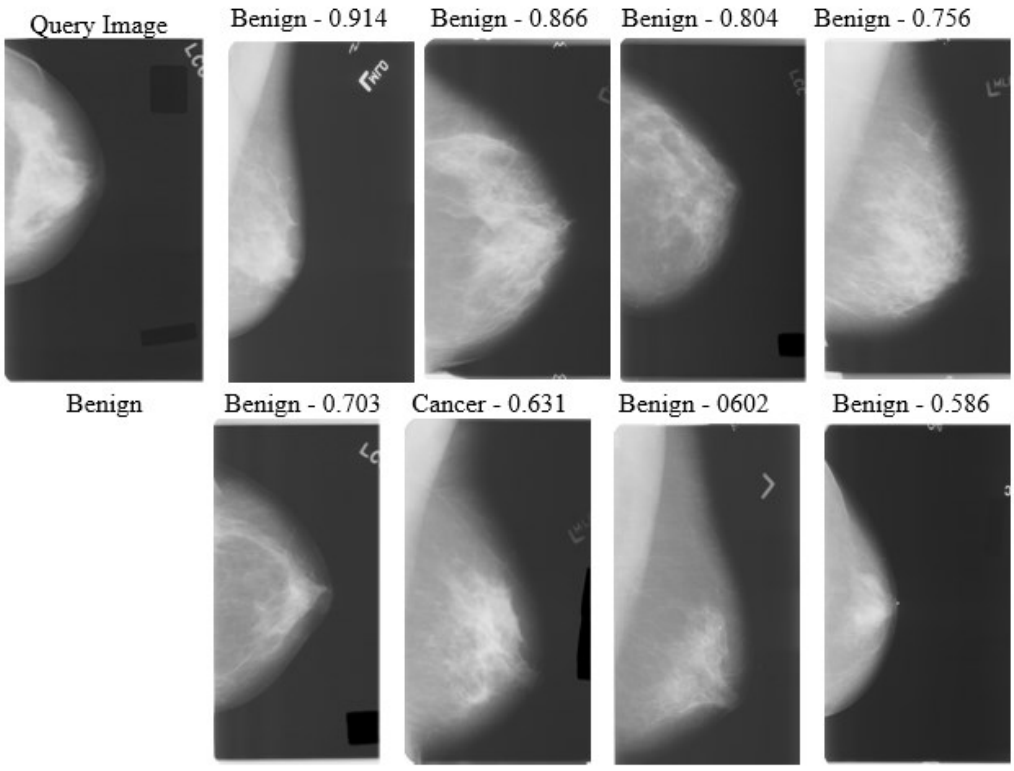

Figure 7.2 Retrieval instance of benign query based on ***ghsthogcohg***.

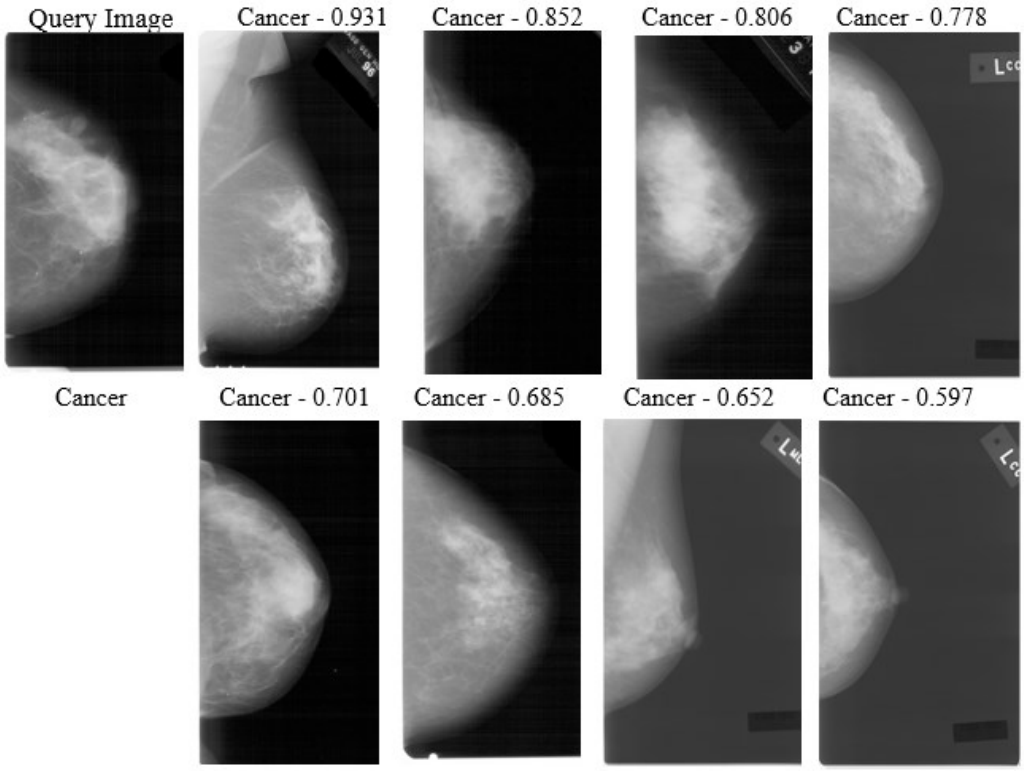

Figure 7.3 Second retrieval instance of cancer query based on ***ghsthogcohg***.

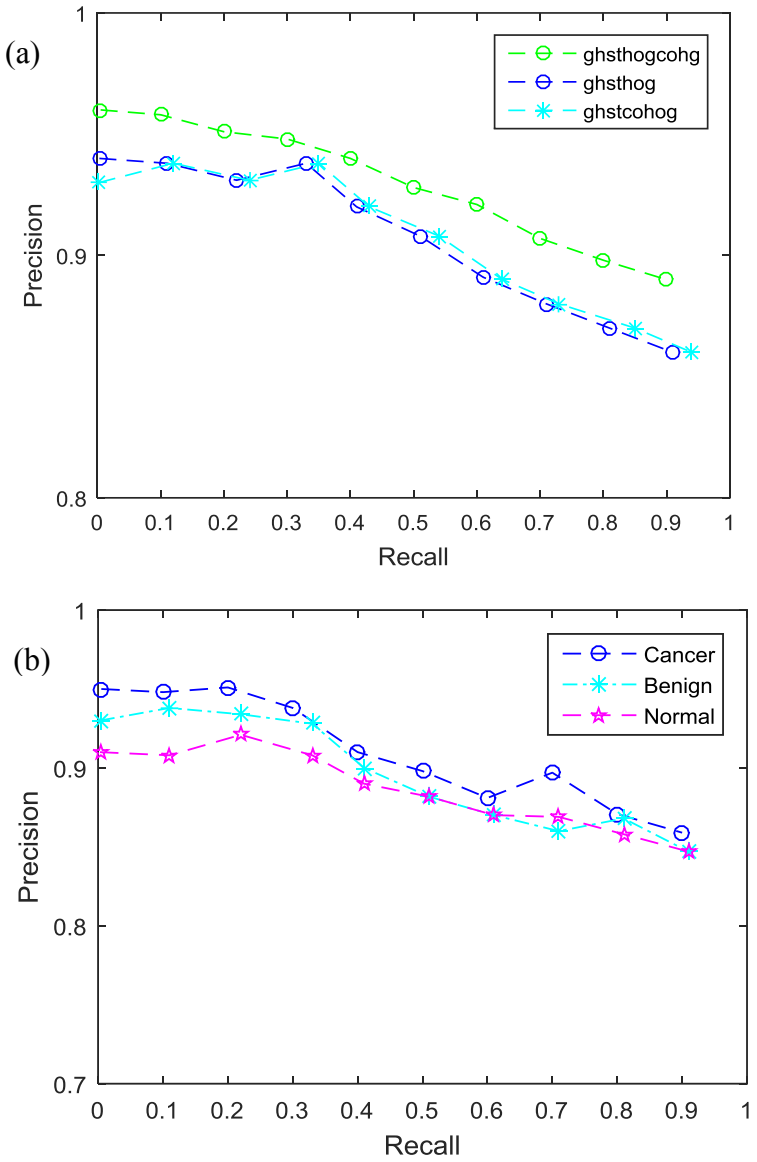

Figure 7.4 Efficiency comparison of retrieval task. (a) comparing of three features; (b) comparing of ***ghsthogcohg*** on 3 different mass types.

A precision–recall curve of ***ghsthogcohg, ghsthog*** and ***ghstcohog*** algorithms was shown in Fig. 7.4(a), representing that ***ghsthogcohg*** features outperform the ***ghsthog*** and ***ghstcohog***. Fig. 7.4(b) shows that, when ***ghsthogcohg*** features are utilized, cancer type mass is the most distinguishable among three types. The experiments confirm the efficiency of ***ghsthogcohg*** features on the characterization of breast masses. The characteristic of masses was better expressed by ***ghsthogcohg***. Concerning ***ghsthogcohg***, for 7% of recall, 93% of precision means that from 5880 mammogram images, 5468 were retrieved appropriately.

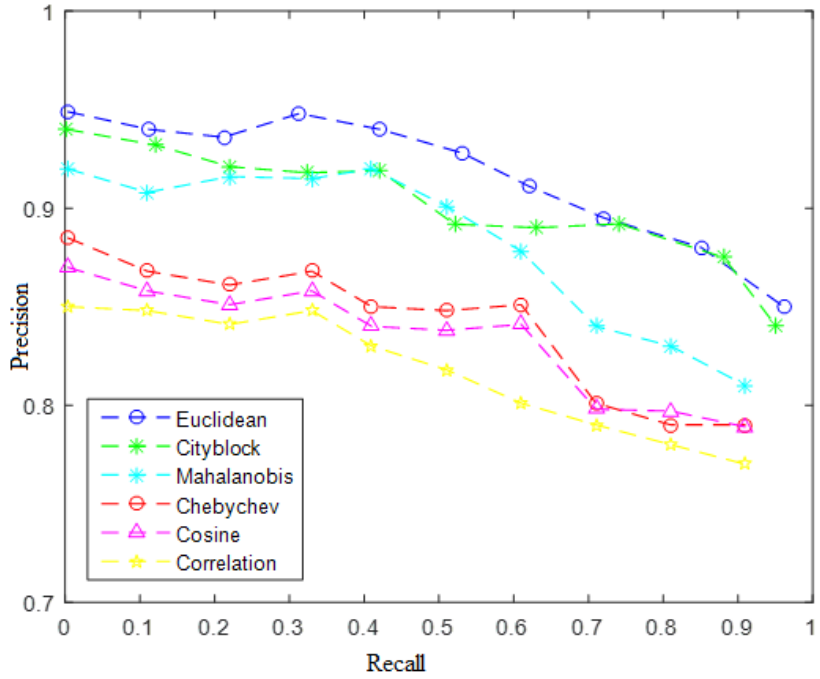

Figure 7.5 Retrieval efficiency comparison for different distance metrics.

Fig. 7.5 presents the PR curves for the six different distance measures. From Fig. 7.5, it is clear that the best accuracy is achieved when ***Euclidean*** distance is used. The city block and Mahalanobis distance also give good performance.

7.3. Experimental Results of Proposed Framework II

In our second proposed framework, eig(Hess)-HOG feature vector has been proposed. NSCT is used for mass feature extraction. Additionally, a 9-D shape feature and a 7-D mass feature are extracted which represent the mass boundary and the average contrast, smoothness, orientation, uniformity, entropy, perimeter and circularity [18]. Finally, a 6-D texture features representing the energy, correlation, entropy, inverse difference moment, contrast and homogeneity are obtained from the GLCM.

Also, ELM based CBIR system is proposed. In this manner, retrieval time is reduced, retrieval precision and classification accuracy are increased.

The performance of ELM classifier depends on the selection of number of neurons in hidden layer L which was determined as $L = 700$ by trials with increments within the range of 100-1000. It was found that both the training and the testing errors were decreased when L increased to around 700 and after that the training and the testing performance did not improve and kept almost fixed as shown in Fig. 7.6. We also

tested with different activation functions, such as sigmoid, tangent sigmoid, sin, and radial basis and the tangent-sigmoid was found to be the optimal one.

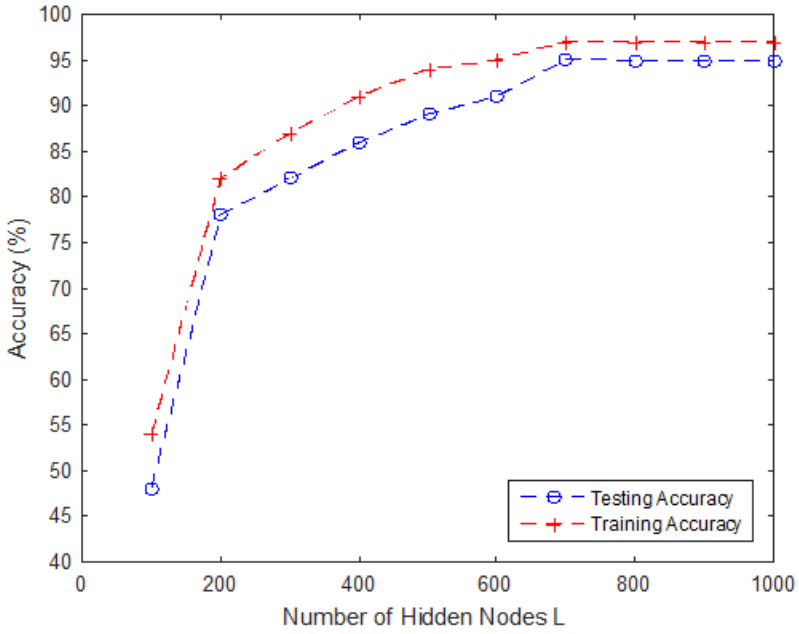

Figure 7.6 The number of hidden layer nodes L determination with L=700.

Table 7.4 Utilized different types of feature sets

f	*Feature Set*
f_1	Shape, Mass, GLCM, NSCT, eig(Hess)HOG
f_2	Shape, Mass, GLCM, NSCT
f_3	Shape, Mass, GLCM, eig(Hess)HOG
f_4	NSCT
f_5	NSCT, eig(Hess)HOG
f_6	eig(Hess)HOG

Finally, for both classification and retrieval evaluation, different combination of concatenated feature vectors is utilized as shown in Table 7.4. For example, the f_1 feature set consists of all five different features: shape, mass, GLCM, NSCT, eig(Hess)-HOG features, whereas f_6 feature set consists of eig(Hess)-HOG feature only.

7.3.1. Classification Results

As mentioned, the classification accuracies in different feature sets of Table 7.4 are compared and with both SVM and ELM classifier and it was found out that the

f_1 feature set with ELM classifier is the most effective feature set for both two and three class study. For example, Tables 7.5 demonstrate the results for both 2 and 3 class studies for the f_1.

Table 7.5 Classification performance of f_1 feature set for the 2 and 3 classes.

	2 class			*3 class*		
Fold #	Acc.(%)	Sens. (%)	Spec. (%)	Acc. (%)	Sens. (%)	Spec. (%)
Fold 1	98.0167	96.5553	95.0939	86.1817	92.8298	92.7950
Fold 2	97.7035	95.8768	94.0501	94.1176	92.5861	93.5955
Fold 3	96.7641	95.5637	94.3633	93.5607	92.7602	92.5513
Fold 4	97.7035	95.9290	94.1545	93.1778	97.7035	98.9039
Fold 5	96.9729	94.6159	94.2589	97.7035	98.4342	98.0689
Fold 6	97.4948	95.9812	94.4676	98.7474	98.5386	98.6952
Fold 7	96.9729	95.8768	94.7808	98.5908	98.2255	91.3271
Fold 8	97.3904	96.2422	95.0939	92.6854	94.3574	95.7158
Fold 9	97.4948	97.0856	94.6764	94.1484	92.4765	92.8945
Fold 10	97.3904	95.6681	93.9457	93.4169	93.9394	93.8349
Ave	96.9729	95.5480	94.1232	92.4155	98.3612	93.4796

From Table 7.5, it can be observed that f_1 feature set is most effective feature set for both two and three class study. In fact, f_1 feature set with ELM as classifier achieved the highest classification accuracy rate in terms of mean accuracy, sensitivity and specificity parameters after 10-fold CV.

For example, Table 7.6 demonstrates the results for both 2 class study for the f_1 feature set. From The f_1 feature set is more effective than the other feature sets in terms of accuracy, sensitivity and specificity for both two class study. In fact, f_1 feature set with ELM classifier achieved the highest classification accuracy rate in terms of mean accuracy, sensitivity and specificity parameters.

Table 7.6 Classification performance of f_1 feature set for the 2-class on IUMD.

2 class (%)			
fold #	Acc.(%)	Sens.(%)	Spec.(%)
Fold 1	96.4193	92.8978	95.8884
Fold 2	95.2916	92.7586	93.8529
Fold 3	95.1978	93.3192	93.9311
Fold 4	96.5877	93.3129	94.1905
Fold 5	94.1955	92.1351	92.0557
Fold 6	95.6966	92.9699	96.4384
Fold 7	95.8351	92.8351	95.3252
Fold 8	94.7563	93.6277	94.2451
Fold 9	95.2157	94.0933	96.3703
Fold 10	93.8342	94.1093	93.2885
Ave	95.3030	93.2059	94.5586

Table 7.7 Performance comparisons of SVM and ELM classifiers using different feature sets.

		Measures	(%)					
			f_1	f_2	f_3	f_4	f_5	f_6
2 class	ELM	Ave. Acc.	96.973	95.709	95.219	93.742	92.228	94.665
		Ave. Sens.	95.548	97.223	96.722	96.743	97.421	99.853
		Ave. Spec.	94.123	94.196	93.716	90.741	87.035	89.478
	SVM	Ave. Acc.	94.086	92.015	94.427	91.536	90.341	91.852
		Ave. Sens.	93.824	95.357	93.118	94.124	94.117	96.741
		Ave. Spec.	91.216	92.628	90.240	88.687	84.896	86.224
3 class	ELM	Ave. Acc.	92.415	92.318	91.517	79.547	78.092	85.788
		Ave. Sens.	98.361	98.877	98.678	98.642	97.409	99.357
		Ave. Spec.	93.479	91.691	92.442	83.016	83.528	93.152
	SVM	Ave. Acc.	90.125	89.654	89.884	76.004	74.011	83.256
		Ave. Sens.	95.244	94.519	95.331	94.875	92.546	95.446
		Ave. Spec.	89.886	87.359	90.214	79.954	80.820	89.744

The classification efficiency, training and testing the performances of SVM and ELM were compared independently. As shown in Table 7.7, it can be seen that the proposed methods are effective on the DDSM database and ELM is a highly effective classification technique for this task. It is also proved to be highly efficient as lesser computational time was required compared to SVM with same sets but of different training data sizes.

7.3.2. Retrieval Results

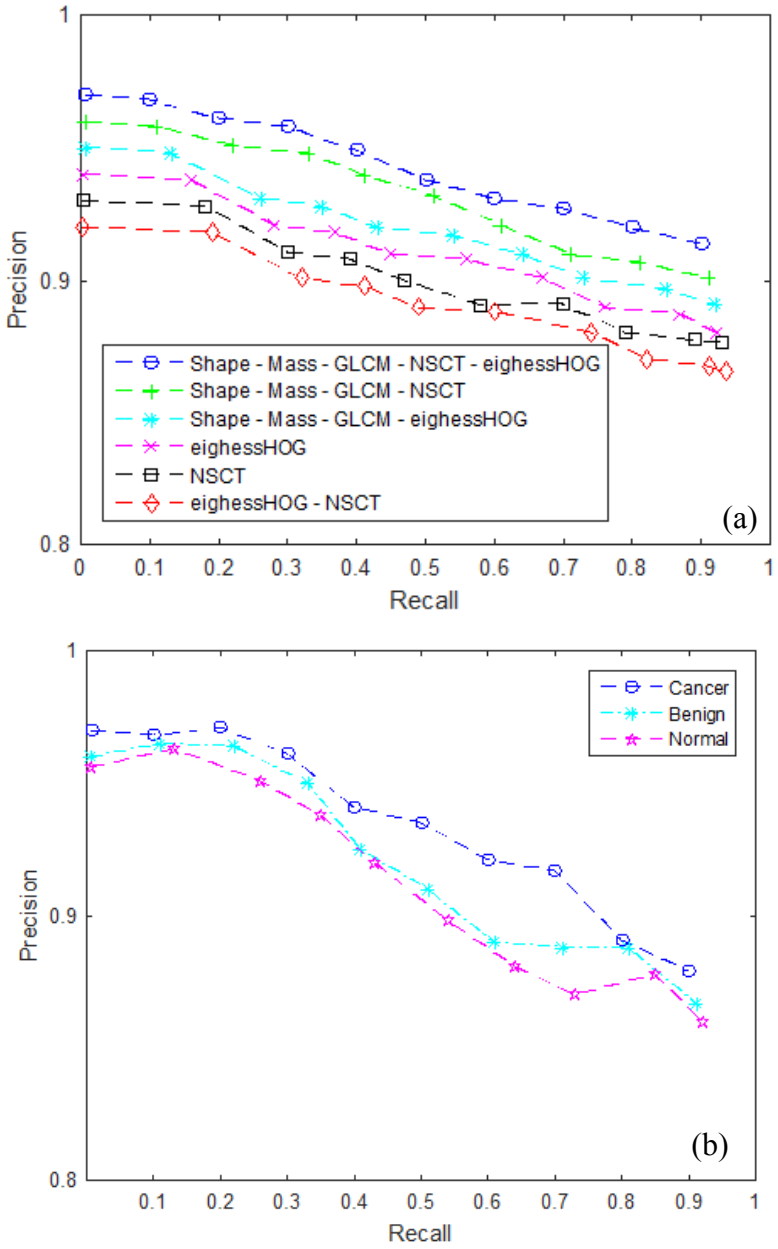

Figure 7.7 Efficiency comparison of retrieval task (a) comparison of six feature sets; (b) retrieval performance of f_1 feature set.

A precision–recall curve of different feature sets (f_1-f_6) on DDSM dataset is shown in Fig. 7.7 (a) which represents that f_1 outperforms all other feature sets. Fig. 7.7 (b) shows that when f_1 feature sets are used, the cancer masses are the most discriminative among three types of masses. Concerning f_1 feature set for 4% of recall, 96% of precision means that from 5880 mammogram images, 5644 are retrieved appropriately.

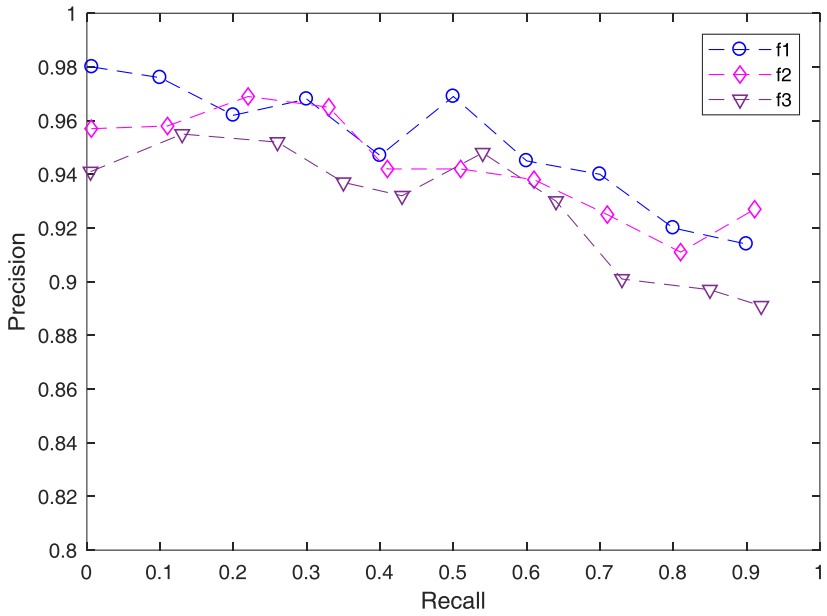

Figure 7.8 Performance evaluation of 3 feature sets on IUMD.

A precision–recall curve of different feature sets (f_1-f_3) on IUMD is shown in Fig. 7.8 which represents that f_1 feature set outperforms the all other feature sets. The results verify that the characteristic of breast masses was better represented by the f_1 feature set. Concerning f_1 feature set for a 3% of recall, a precision of 97% means that from 2880 mammogram images returned by the our proposed CBIR system, 2685 were relevant.

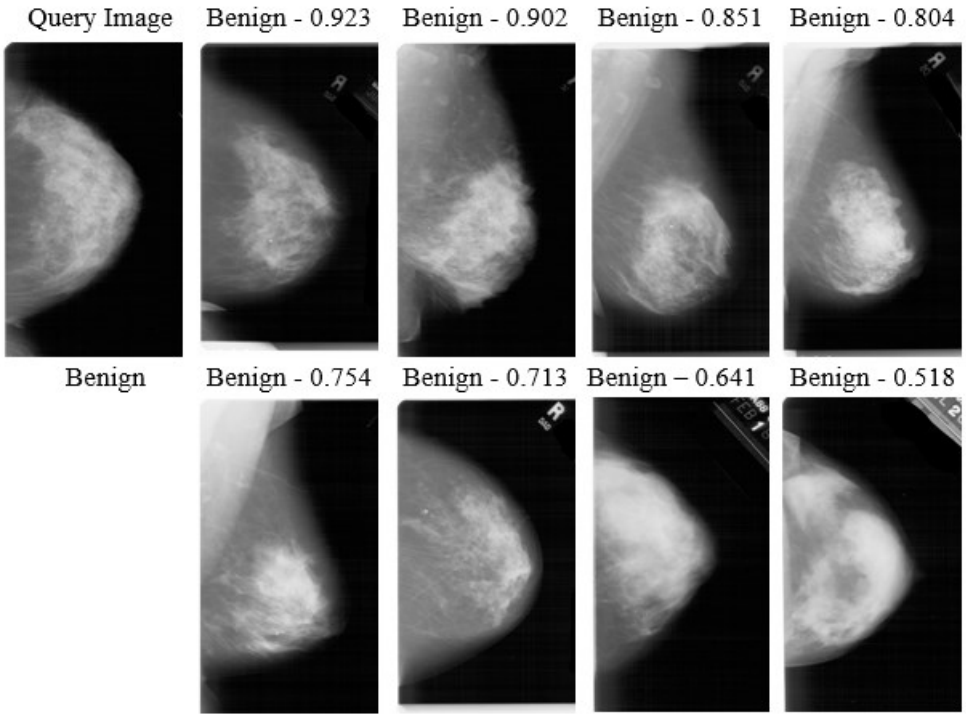

Figure 7.9 Retrieval instance of benign query based on f_1 feature set.

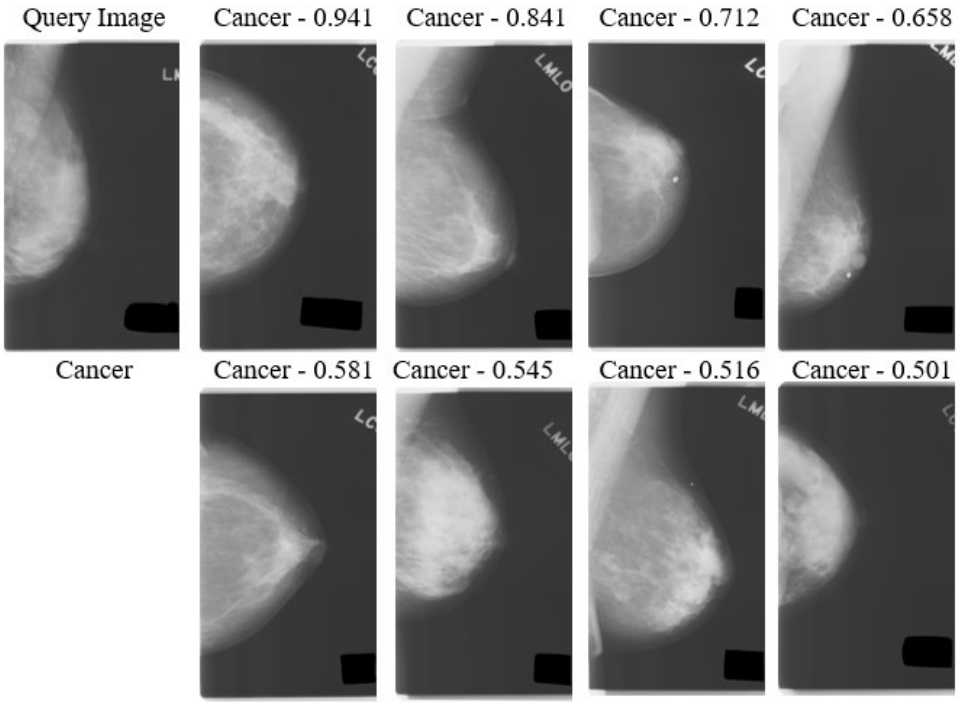

Figure 7.10 Retrieval instance of cancer query based on f_1 feature set.

Fig. 7.9 indicates a sample of benign query image and retrieved images based on the f_1 feature set. The system retrieved all the top 8 images appropriately. Another retrieval instance of cancer type is demonstrated in Fig. 7.10. All the retrieved images are cancer type.

7.4. Experimental Results of Proposed Framework III

In our third framework, deep feature based feature extraction is proposed. Fine-tuning operation is applied on the trained CNN network. The obtained network is used for extracting features in next procedures. Then high-level features which are extracted from fc7 layer of trained model and f_1 feature set are extracted for training 2 ELM classifiers. And the outcomes of these two classifiers are combined. And the proposed decision mechanism has a better simulation of doctors' thought structure in the diagnosis.

7.4.1. Proposed Decision Mechanism

We have extracted high-level features from fc7 layer of network and f_1 feature set is used for training. Then two ELM classifiers have been utilized to determine the type of mass based on the features. In addition, we applied 10-fold cross validation in our linear ELM experiments. In addition, each image in the dataset is a gray scale with the size of 227×227. All images had been normalized and whitened before given into to the network to enhance the performance of CNN [103].

The main objective of proposed framework is to obtain global, local and details of breast masses. It helps to form a unified description of mass. Our decision support system imitates physicians' diagnosis operation. It is largely consists of symptom comparisons. The obtained deep features played significant roles in the whole framework. Because it is thought that human cognitive system is in accordance with these deep features. ILSVRC dataset is chosen to train our CNN model.

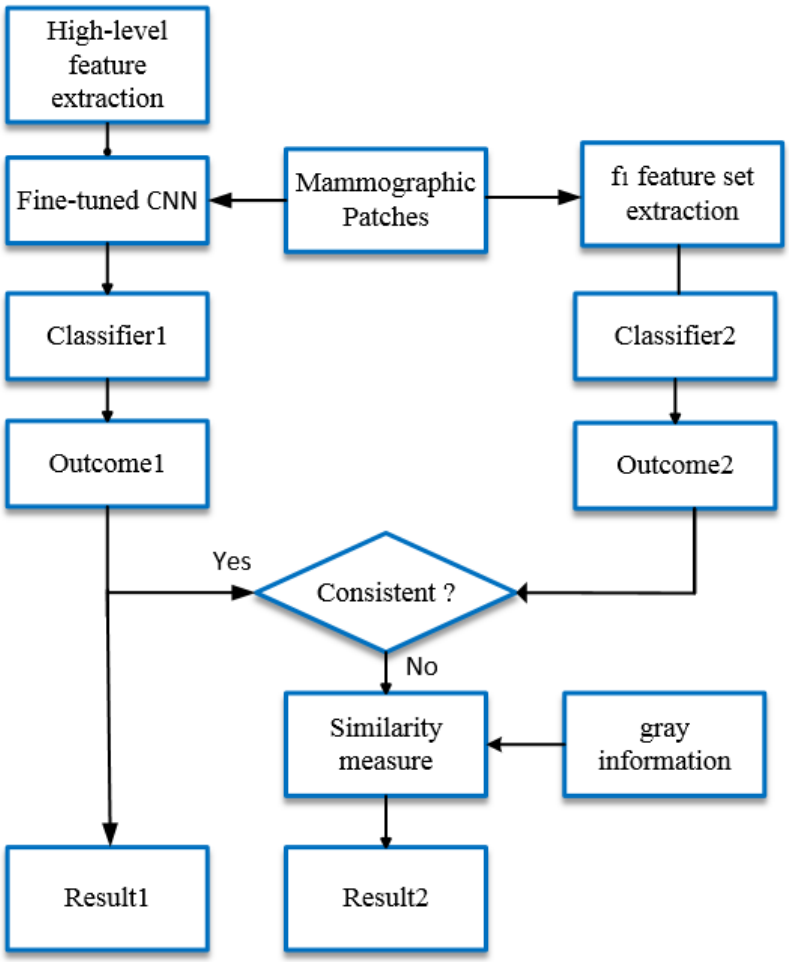

Figure 7.11 Proposed decision mechanism flow chart.

To associate the outputs of two classifiers the methodology in Fig. 7.11 is utilized. High-level features of test images are extracted from the fine-tuned network and f_1 feature set is extracted as explained in previous section. f_1 feature set consists of all five different features: Shape, Mass, GLCM, NSCT, eig(Hess)-HOG features. Then, two different classifiers have been used for classification and retrieval of the obtained features.

In testing phase, if the outputs of two classifiers are same, the outputs are taken as correct as shown in Fig. 7.11. If the outputs of test images are conflicting, they are associated with uncertain set. To make decision on what type each image in the testing set belongs to, gray level intensity is used to compute closeness of the images to benign and malignant ones. While computing closeness parameter, benign and malignant training instances are clustered into several subclasses respectively. Hierarchical k-means method is utilized for clustering of images in training set [104]. Considering the closeness parameter, the uncertain set is separated into two types.

Image in the uncertain set is $x_{U_i}, i = 1,2,...m$ clusters of training benign and malignant instances is $C_{B_j}, j = 1,2,...n$ and $C_{M_j}, j = 1,2,...n$ respectively; numbers of images in subclass are $N_{B_j}, j = 1,2,...n$ in benign data and $N_{M_j}, j = 1,2,...n$ in malignant data; $\left|x_{U_i} - C_{B_j}\right|$ and $\left|x_{U_i} - C_{M_i}\right|$ were both euclidean distance of uncertain image x_{U_i} to center of clustering. The similarity of a test image in uncertain set to benign ones is:

$$S_{U_{IB}} = \frac{1}{\sum_{j=1}^{n} \frac{N_{B_j}}{N_B} \left|x_{U_i} - C_{B_j}\right|}, i = 1,2,...m \tag{7.1}$$

And similarity of a test image in uncertain set to malignant ones is:

$$S_{U_{IM}} = \frac{1}{\sum_{j=1}^{n} \frac{N_{M_j}}{N_M} \left|x_{U_i} - C_{M_j}\right|}, i = 1,2,...m \tag{7.2}$$

Thereafter, the similarity of each image is calculated and the final decision is given according to the rules given below [105]:

If $S_{U_{IB}} \geq S_{U_{IM}}$, the instance is considered as benign;

If $S_{U_{IB}} < S_{U_{IM}}$, the instance is considered as malignant;

To demonstrate the efficiency of utilized features the t-distributed stochastic neighbor embedding (t-SNE) is used [106]. The tSNE method visualizes high dimensional information. The effectiveness of this method was shown in assessment of different types of features. The t-SNE map separates the points linearly in two-dimensional map. To demonstrate efficiency of different types of features, deconvolution, activation and other operations have been applied on high level and f_1 feature set [107], [108]. The t-SNE map helps to indicate the emphasis of different type features. Consequently, we used t-SNE maps to know whether the features could express masses.

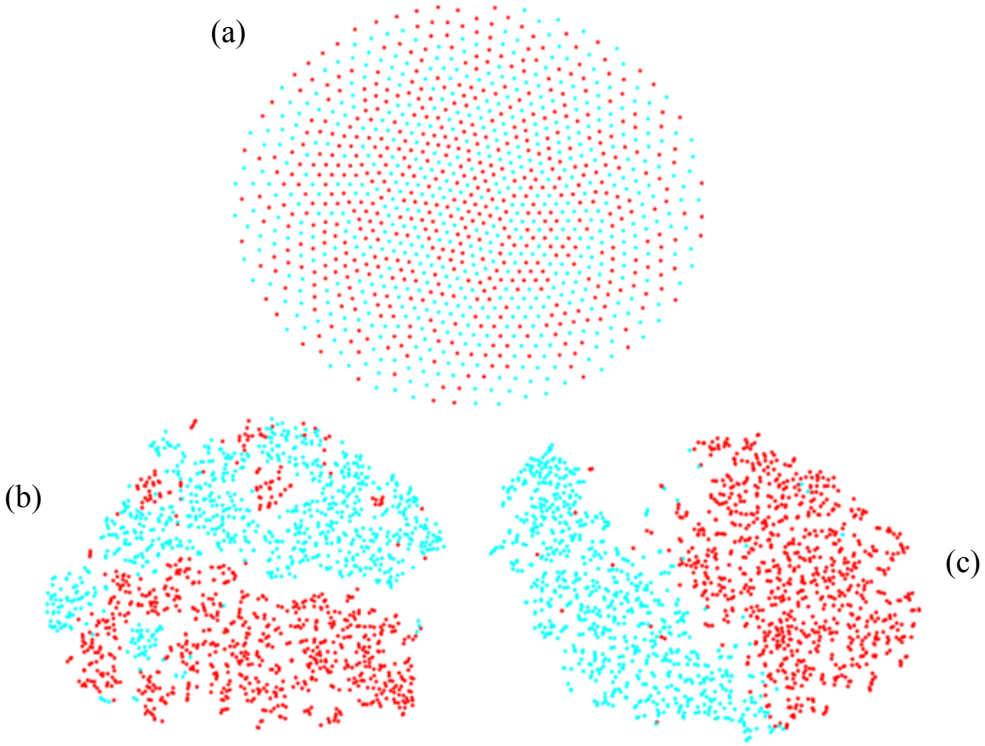

Figure 7.12 The t-SNE maps of features. (a) original images (b) high-level feature (c) f_1 feature set.

7.4.2. Classification Results and Analysis

Fig. 7.13 shows the ROC curves for high-level, f_1 feature set and our method. As shown in Fig. 7.13, when we used the f_1 feature set and high-level features individually for the classification and retrieval tasks, performances weren't good enough. It can be enhanced. Fig. 7.12 also shows the ability of CNN model to extract discriminative features in an intuitive way. Consequently, it is obviously seen that deep features improve the distinction performance of two different mass types. It is also seen that samples were more distinguishable after they were expressed by deep features.

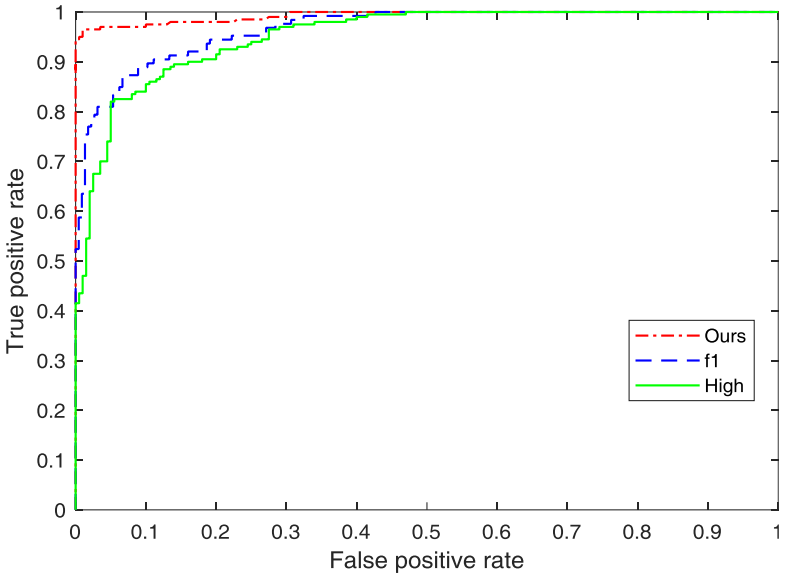

Figure 7.13 ROC curves of high-level, f_1 feature set and our method based classification.

From Tables 7.8, it can be observed that f_1 feature set is more effective than high-level features. In fact, our proposed decision mechanism with ELM as classifier achieved the highest classification performance.

Table 7.8 Classification performance of deep feature based decision mechanism.

fold #	*Accuracy(%)*	*Sensitivity(%)*	*Specivity(%)*
Fold 1	97.9256	97.0549	93.4207
Fold 2	99.0522	97.7084	97.8459
Fold 3	94.2580	98.6837	95.0127
Fold 4	91.8532	91.0009	96.3730
Fold 5	98.2569	95.6649	93.2901
Fold 6	97.4948	96.7060	92.8495
Fold 7	98.9437	97.4345	94.8181
Fold 8	98.6504	93.3903	94.4945
Fold 9	99.5822	93.9883	97.3896
Fold 10	97.1248	97.5814	96.2121
Ave	97.3142	95.9213	95.1706

Table 7.9 Comparison of proposed frameworks with state of art systems.

Literature	*Dataset*	*Classifier*	*Acc(%)*	*Sens(%)*	*Spec(%)*
Wang et al. [109]	DDSM	SVM	92.74	-	-
B. Swiderski et al. [27]	DDSM	SVM	0.909	0.967	0.801
M. Jadoon et al, [19]	DDSM	SVM	83.74	-	-
Liu and Tang [18]	DDSM	SVM	93.00	92.00	92.00
Dong et al., [110]	DDSM	GA-SVM	93.24	94.78	91.76
Jen & Yu, [80]	DDSM	ADC	-	86.0	84.0
N. Gedik et al.	DDSM	SVM	93.95	87.23	91.39
R. Rouhi et al., [111]	DDSM	MLP	95.01	96.25	93.78
Jiao et al. [86]	DDSM	CNN	96.7	-	-
Proposed scheme I	DDSM	SVM	**93.83**	92.40	**95.10**
Proposed scheme II	DDSM	ELM	**96.97**	**95.54**	94.12
Proposed scheme III	DDSM	ELM	**97.31**	**95.92**	**95.17**

Table 7.9 shows the comparison between our frameworks and a number of state of art systems. For the DDSM database, our proposed frameworks obtained comparable performance in accuracy, sensitivity and specificity. As seen from Table 7.9 best results have been obtained from the third framework. Second framework is the other best method after the third method. The promising results might be owing to the good segmentation algorithm as well as the effective feature extraction methods.

7.4.3. Computational Time Analysis

The proposed approaches have enough classification and retrieval ability. However, computational complexity and classification time is an important issue. For further verifying the classification time effectiveness of the proposed frameworks, additional experiments are conducted. Table 7.10 shows the size of feature vector, accuracy and overall classification time of the methods in literature comparatively. It can be seen that the proposed framework III achieves excellent classification performance. However, as seen from Table 7.10, the proposed framework I has lower feature dimension. So it has the best time efficiency. But, it has not enough classification accuracy. Our proposed frameworks provide highly discriminative features for lower computational time and improved performance. As a result, our

proposed frameworks have lower computational time in both classification and retrieval stages. Besides, it seen also seen from Table 7.10 that utilization of novel feature descriptors improves the average classification performance. Therefore, it is critical to consider the higher order derivatives to improve the accuracy and reduce the feature dimension.

Table 7.10 Computational performance of proposed frameworks.

Method	Feat. size	Accuracy (%)	Time (s)
SM-BoW [109]	5394	90.56	2.67
SM-LDA [109]	438	92.74	0.24
SCC [112]	1380	85.48	0.80
PCA-CC [113]	10000	90	5.5
COCC [114]	225	83.9	0,15
Z. Jiao et al.[86]	2048	96.7	1,62
PCET [33]	605	93.72	0,32
RLTP [29]	100	82.27	0,08
CNN-CT [19]	784	83.74	0,65
Proposed framework I	**30**	93.83	**0,02**
Proposed framework II	306	96.973	0,26
Proposed framework III	2048	**97.3142**	1,09

As shown in Fig. 7.14, it can be observed that the ELM is a quite efficient. The different size of training data is used to train SVM, and ELM to indicate the efficiency of ELM. The SVM is more complex than ELM, it consumes more computational time. It is observed from Fig. 7.14 that ELM is much more efficient than SVM.

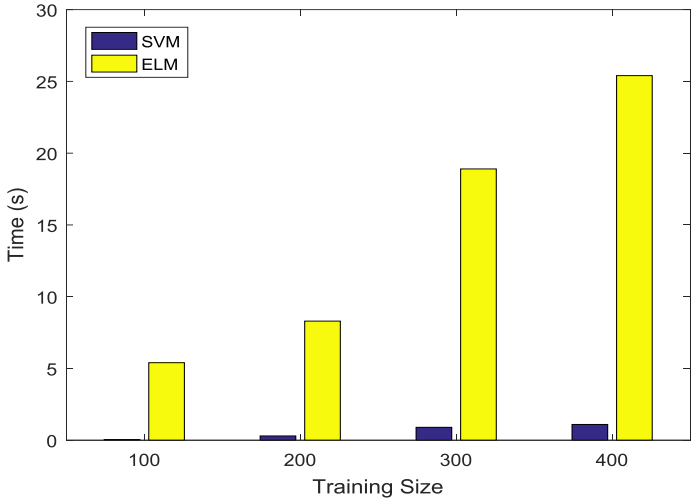

Figure 7.14 Training time and data size relationship.

7.4.4. Retrieval Results

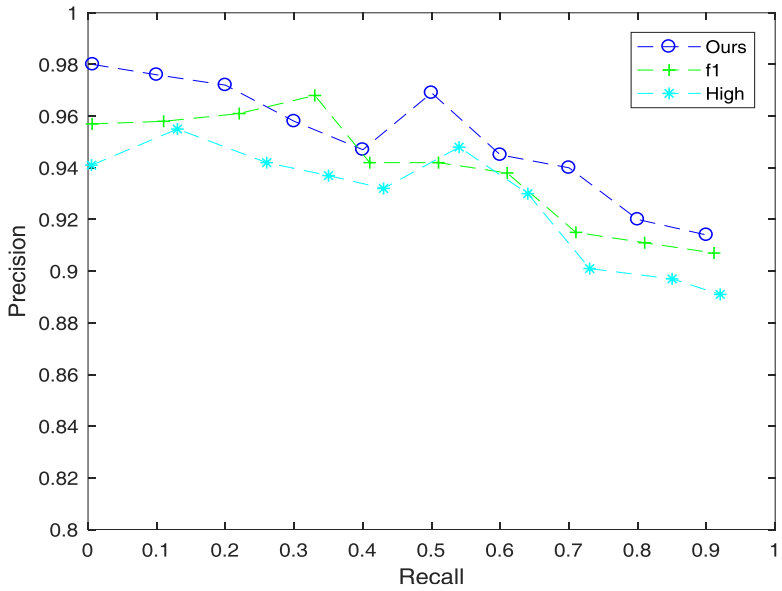

Figure 7.15 Performance evaluation of different feature sets.

A precision–recall curve based on different feature sets is shown in Fig. 7.15 which shows that our proposed decision mechanism outperforms the all other feature sets. The results verify that the characteristic of breast masses was better represented by the deep feature based decision mechanism. Concerning this decision mechanism, for a 3% of recall, a precision of 97% means that from 29824 mammographic patches returned by the our proposed CBIR system, 28929 were relevant.

Fig. 7.16 demonstrates an instance of a benign query mass image and retrieved masses based on our framework. All retrieved 8 images are benign. The other instance

is demonstrated in Fig. 7.17, using an image of cancer category. All the retrieved mammographic patches are cancer.

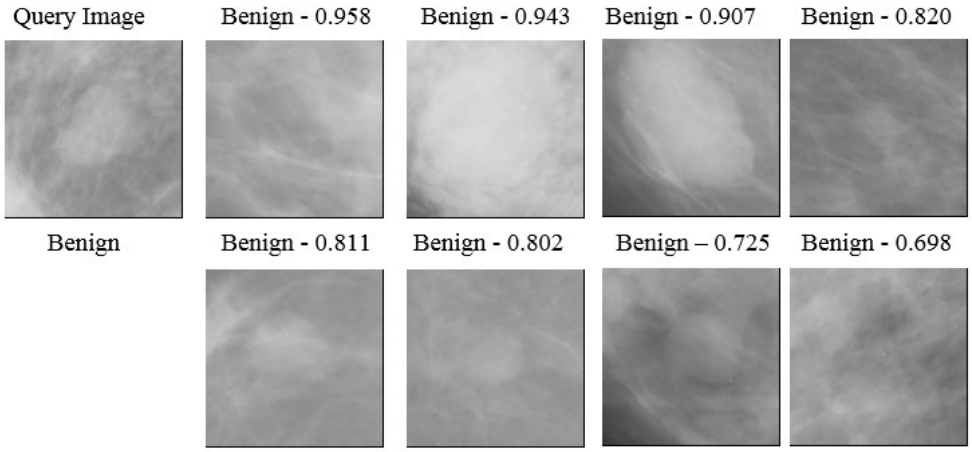

Figure 7.16 Retrieval instance of benign query based on f_1 feature set.

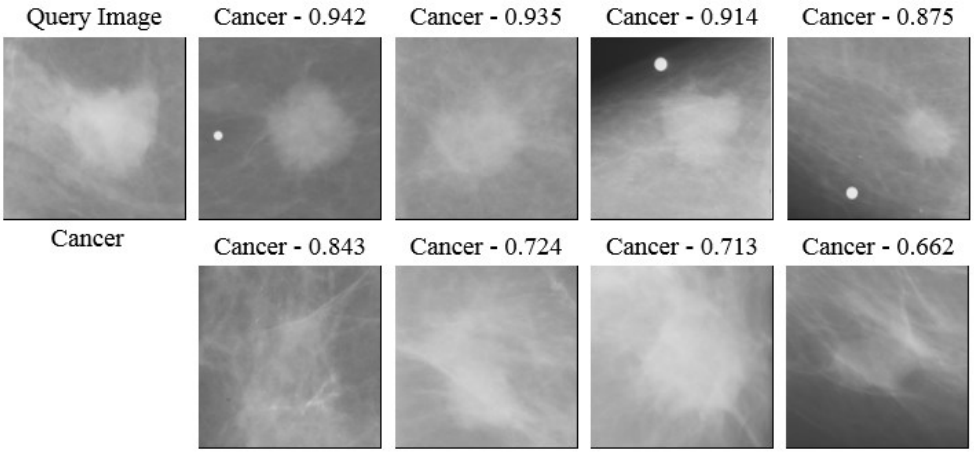

Figure 7.17 Retrieval instance of cancer query based on f_1 feature set.

The feature extraction is a quite challenging task. Therefore, the difficulty of making efficient features with various types was unavoidable. In addition, strategies for combination of these features have been popular in the last decade. However, researchers have not obtained satisfactory results on large datasets. Experiments clearly state that a single type of conventional feature is not enough for mammogram retrieval. Our proposed framework benefits from deep features of a CNN model. The proposed decision mechanism is effective enough to obtain good performance.

Experimental results significantly show that proposed decision mechanism outperforms the state of art systems. Furthermore, it also represents effectiveness of our procedure when large datasets are not available in the medical field.

8. CONCLUSIONS

Breast cancer indicates development of malignant lesions in cells. It is the most common cancer type in the world after lung cancer. It is reported that one in every 8 females will have breast cancer at a certain time in their lives. Although seen in men, women cases are 100 times more than men cases. The best preventive method against breast cancer is early diagnosis. For this reason, various methods are being developed to increase early detection. Computer assisted detection and diagnosis systems are used to assist doctors in interpreting medical images. They use digital radiographic images (mammography, MRI, ultrasound, etc.), mathematical and statistical analysis methods to determine ambiguous areas (target diagnoses or pathologies) for the radiologist. CAD is an auxiliary diagnostic system; the final decision belongs to the physician. Recently, CAD systems have become part of routine clinical trials for breast cancer detection through mammograms in screening centers and hospitals in the United States. As a result, a decision support system is developed for the automated mass detection, classification and retrieval of mammograms in the thesis. The developed system is evaluated for the retrieval and classification of the mammographic images. And, we also developed a novel mammography dataset which is named IUMD because of insufficiency of existing datasets.

In this thesis, three different CBIR frameworks have been proposed. The developed CBIR system can briefly summarized as follows.

Segmentation of Breast Region

- This is a general process before the detection of breast mass. In this process, the segmentation of target region has been performed by eliminating the label outside the breast area, noise parts. Breast contour is also obtained roughly. In addition, pectoral muscle removal is performed.

Mass Detection

- To determine the suspicious mass regions, 2 different segmentation methods are utilized. In our first framework, Marker-controlled watershed segmentation (MCWS) is utilized and Graph-Based Visual Saliency (GBVS) is used in our second framework.

Feature Extraction

- In our first framework, 3 different feature vectors have been proposed. The first method uses combination of geometric features of mass and histogram features of the HOG named ghsthog. The second method uses combination of geometric features of mass and histogram features of the CoHOG named ghstcohog. The third method exploits combination of geometric features of mass and histogram features of HOG and CoHOG named ghsthogcohg.
- In our second framework, eig(Hess)-HOG feature vector have been proposed. NSCT are used for mass feature extraction. Additionally, a 9-D shape feature and a 7-D mass feature are extracted which representing the mass boundary and the average contrast, smoothness, orientation, uniformity, entropy, perimeter and circularity [18]. Finally, a 6-D texture features representing the energy, correlation, entropy, inverse difference moment, contrast and homogeneity is obtained from the GLCM.
- In our third framework, deep feature based feature extraction is proposed. Fine-tuning operation is applied on the trained CNN network. The obtained network is used for extracting features in next procedures. Then high-level features which extracted from fc7 layer of trained model and f_1 feature set are extracted for training 2 ELM classifiers. And the outcomes of these two classifiers are combined. And the proposed decision mechanism has a better simulation of doctors' thought structure in the diagnosis.

Classification and Retrieval

- In determining the benign / malignant and benign / malignant / normal probabilities of detected mass regions, the above-mentioned proposed features are used to classify by SVM and ELM methods.
- Also, ELM based CBIR system is proposed. In this manner, retrieval time is reduced; retrieval precision and classification accuracy are increased.
- In our first framework, ghsthogcohg has a 7% of recall and a 93% of precision. This means that 5468 of 5880 mammogram images retrieved appropriately. The correct classification accuracy, sensitivity and specificity of first framework is 93.83% 92.40% and 95.10% respectively.
- In our second framework, f_1 feature set has a 4% of recall and a 96% of precision. This means that 5644 of 5880 mammogram images retrieved

appropriately. The correct classification accuracy, sensitivity and specificity of first framework is 96.973%, 95.548% and 94.123% respectively.

- In our first framework, proposed decision mechanism has a 3% of recall, a precision of 97%. This means that 28929 of 29824 mammographic patches returned by proposed CBIR system relevant. The correct classification accuracy, sensitivity and specificity of first framework is 97.3142%, 95.9213% and 95.1706% respectively.
- Compared with related literature, proposed framework III has the highest accuracy, sensitivity and specificity.
- Besides compared with related literature, the proposed framework I has lower feature dimension. Therefore, it has the best time efficiency. The mean running time for the classification is 0.02s.

The developed system is evaluated for the retrieval and classification of the mammographic images. The experiments show the efficiency of our approaches for visually similar mass retrieval and prediction the kind of image for diagnostic correctness.

9. REFERENCES

[1] &NA;, *American Cancer Society Published Second Edition of Global Cancer Atlas*, **Oncology Times**, 37:1 (2015) 34.

[2] D. S. AL Mousa *et al.*, *Mammographic Density and Cancer Detection*, **Academic Radiology**, 21:11 (2014) 1377–1385.

[3] L. Tabár *et al.*, *Swedish Two-County Trial: Impact of Mammographic Screening on Breast Cancer Mortality during 3 Decades*, **Radiology**, 260:3 (2011) 658–663.

[4] R. L. Siegel, K. D. Miller, and A. Jemal, *Cancer statistics, 2015*, **CA: A Cancer Journal for Clinicians**, 65:1 (2015) 5–29.

[5] D. C. Moura and M. A. Guevara López, *An evaluation of image descriptors combined with clinical data for breast cancer diagnosis*, **International Journal of Computer Assisted Radiology and Surgery**, 8:4 (2013) 561–574.

[6] V. Özmen, *Controversies on Mammography Screening in the World and Bahceşehir Population-Based Organized Mammography Screening Project in Turkey*, **J Breast Health**, 11 (2015) 152–154.

[7] H. D. Nelson, *Screening for Breast Cancer: An Update for the U.S. Preventive Services Task Force*, **Annals of Internal Medicine**, 151:10 (2009) 727.

[8] K. Ganesan, U. R. Acharya, C. K. Chua, L. C. Min, K. T. Abraham, and K.-H. Ng, *Computer-Aided Breast Cancer Detection Using Mammograms: A Review*, **IEEE Reviews in Biomedical Engineering**, 6 (2013) 77–98.

[9] R. M. Rangayyan, F. J. Ayres, and J. E. Leo Desautels, *A review of computer-aided diagnosis of breast cancer: Toward the detection of subtle signs*, **Journal of the Franklin Institute**, 344:3–4 (2007) 312–348.

[10] Y. Zhang, N. Tomuro, J. Furst, and D. S. Raicu, *Building an ensemble system for diagnosing masses in mammograms*, **International Journal of Computer Assisted Radiology and Surgery**, 7:2 (2011) 323–329.

[11] I. Buciu and A. Gacsadi, *Directional features for automatic tumor classification of mammogram images*, **Biomedical Signal Processing and Control**, 6:4 (2011) 370–378.

[12] J. M. H. Timmers, H. J. van Doorne-Nagtegaal, A. L. M. Verbeek, G. J. den Heeten, and M. J. M. Broeders, *A dedicated BI-RADS training programme: Effect on the inter-observer variation among screening radiologists*, **European Journal of Radiology**, 81:9 (2012) 2184–2188.

[13] V. Corsetti *et al.*, *Evidence of the effect of adjunct ultrasound screening in women with mammography-negative dense breasts: Interval breast cancers at 1year follow-up*, **European Journal of Cancer**, 47:7 (2011) 1021–1026.

[14] S. Hofvind, G. Ursin, S. Tretli, S. Sebuødegård, and B. Møller, *Breast cancer mortality in participants of the Norwegian Breast Cancer Screening Program*, **Cancer**, 119:17 (2013) 3106–3112.

[15] E. S. De Paredes and E. S. De Paredes, *Atlas of mammography*, Wolters Kluwer Health/Lippincott Williams & Wilkins, 2007 .

[16] R. Dash, S. Roy, S. Beura, and B. Majhi, *Classification of mammogram using two-dimensional discrete orthonormal S-transform for breast cancer detection*, **Healthcare Technology Letters**, 2:2 (2015) 46–51.

[17] C.-H. Wei, S. Y. Chen, and X. Liu, *Mammogram retrieval on similar mass lesions*, **Computer Methods and Programs in Biomedicine**, 106:3 (2012) 234–248.

[18] X. Liu and J. Tang, *Mass Classification in Mammograms Using Selected Geometry and Texture Features, and a New SVM-Based Feature Selection Method*, **IEEE Systems Journal**, 8:3 (2014) 910–920.

[19] M. M. Jadoon, Q. Zhang, I. U. Haq, S. Butt, and A. Jadoon, *Three-Class Mammogram Classification Based on Descriptive CNN Features*, **BioMed Research International**, 2017 (2017) 1–11.

[20] N. Dhungel, G. Carneiro, and A. P. Bradley, *A deep learning approach for the analysis of masses in mammograms with minimal user intervention*, **Medical Image Analysis**, 37 (2017) 114–128.

[21] T. Kooi *et al.*, *Large scale deep learning for computer aided detection of mammographic lesions*, **Medical Image Analysis**, 35 (2017).

[22] R. M. Nishikawa, *Current status and future directions of computer-aided diagnosis in mammography*, **Computerized Medical Imaging and Graphics**,

31:4–5 (2007) 224–235.

[23] R. M. Rangayyan, *Content-based retrieval and analysis of mammographic masses*, **Journal of Electronic Imaging**, 14:2 (2005) 23016.

[24] S. K. Kinoshita, P. M. de Azevedo-Marques, R. R. Pereira, J. A. H. Rodrigues, and R. M. Rangayyan, *Content-based Retrieval of Mammograms Using Visual Features Related to Breast Density Patterns*, **Journal of Digital Imaging**, 20:2 (2007) 172–190.

[25] B. Zheng, *Computer-Aided Diagnosis in Mammography Using Content-Based Image Retrieval Approaches: Current Status and Future Perspectives*, **Algorithms**, 2:2 (2009) 828–849.

[26] S. R. Ara, S. K. Bashar, F. Alam, and M. K. Hasan, *EMD-DWT based transform domain feature reduction approach for quantitative multi-class classification of breast lesions*, **Ultrasonics**, 80 (2017) 22–33.

[27] B. Swiderski *et al.*, *Novel methods of image description and ensemble of classifiers in application to mammogram analysis*, **Expert Systems with Applications**, 81 (2017) 67–78.

[28] M. M. Pawar and S. N. Talbar, *Genetic Fuzzy System (GFS) based wavelet co-occurrence feature selection in mammogram classification for breast cancer diagnosis*, **Perspectives in Science**, 8 (2016) 247–250.

[29] C. Muramatsu, T. Hara, T. Endo, and H. Fujita, *Breast mass classification on mammograms using radial local ternary patterns*, **Computers in Biology and Medicine**, 72 (2016) 43–53.

[30] Y. Li, H. Chen, X. Wei, Y. Peng, and L. Cheng, *Mass classification in mammograms based on two-concentric masks and discriminating texton*, **Pattern Recognition**, 60 (2016) 648–656.

[31] S. K. Wajid and A. Hussain, *Local energy-based shape histogram feature extraction technique for breast cancer diagnosis*, **Expert Systems with Applications**, 42:20 (2015) 6990–6999.

[32] N. Gedik, A. Atasoy, and Y. Sevim, *Investigation of wave atom transform by using the classification of mammograms*, **Applied Soft Computing**, 43 (2016) 546–552.

[33] S. P. Singh, S. Urooj, and A. Lay-Ekuakille, *Breast Cancer Detection Using PCPCET and ADEWNN: A Geometric Invariant Approach to Medical X-Ray Image Sensors*, **IEEE Sensors Journal**, 16:12 (2016) 4847–4855.

[34] H. Alto, *Errata: Content-based retrieval and analysis of mammographic masses*, **Journal of Electronic Imaging**, 16:1 (2007) 19801.

[35] I. El-Naqa, Y. Yang, N. P. Galatsanos, R. M. Nishikawa, and M. N. Wernick, *A Similarity Learning Approach to Content-Based Image Retrieval: Application to Digital Mammography*, **IEEE Transactions on Medical Imaging**, 23:10 (2004) 1233–1244.

[36] X. H. Wang *et al.*, *Automated Assessment of the Composition of Breast Tissue Revealed on Tissue-Thickness-Corrected Mammography*, **American Journal of Roentgenology**, 180:1 (2003) 257–262.

[37] C. Muramatsu *et al.*, *Determination of subjective similarity for pairs of masses and pairs of clustered microcalcifications on mammograms: Comparison of similarity ranking scores and absolute similarity ratings*, **Medical Physics**, 34:7 (2007) 2890–2895.

[38] J. E. E. de Oliveira, A. M. C. Machado, G. C. Chavez, A. P. B. Lopes, T. M. Deserno, and A. de A. Araújo, *MammoSys: A content-based image retrieval system using breast density patterns*, **Computer Methods and Programs in Biomedicine**, 99:3 (2010) 289–297.

[39] L. Wei, Y. Yang, and R. M. Nishikawa, *Microcalcification classification assisted by content-based image retrieval for breast cancer diagnosis*, **Pattern Recognition**, 42:6 (2009) 1126–1132.

[40] J. Liu, S. Zhang, W. Liu, C. Deng, Y. Zheng, and D. N. Metaxas, *Scalable Mammogram Retrieval Using Composite Anchor Graph Hashing with Iterative Quantization*, **IEEE Transactions on Circuits and Systems for Video Technology**, (2016) 1–1.

[41] C.-H. Wei, Y. Li, and P. J. Huang, *Mammogram retrieval through machine learning within BI-RADS standards*, **Journal of Biomedical Informatics**, 44:4 (2011) 607–614.

[42] W. Xie, Y. Li, and Y. Ma, *Breast mass classification in digital mammography*

based on extreme learning machine, **Neurocomputing**, 173 (2016) 930–941.

[43] J. A. Cook, *ROC curves and nonrandom data*, **Pattern Recognition Letters**, 85 (2017).

[44] N. Gordini and V. Veglio, *Customers churn prediction and marketing retention strategies. An application of support vector machines based on the AUC parameter-selection technique in B2B e-commerce industry*, **Industrial Marketing Management**, 62 (2017) 100–107.

[45] Y. Liu, J.-W. Bi, and Z.-P. Fan, *A method for multi-class sentiment classification based on an improved one-vs-one (OVO) strategy and the support vector machine (SVM) algorithm*, **Information Sciences**, 394 (2017) 38–52.

[46] X. Liang, L. Zhu, and D.-S. Huang, *Multi-task ranking SVM for image cosegmentation*, **Neurocomputing**, 247 (2017) 126–136.

[47] L. Zhang, Z. He, and Y. Liu, *Deep object recognition across domains based on adaptive extreme learning machine*, **Neurocomputing**, 239 (2017) 194–203.

[48] N. Zeng, H. Zhang, W. Liu, J. Liang, and F. E. Alsaadi, *A switching delayed PSO optimized extreme learning machine for short-term load forecasting*, **Neurocomputing**, 240 (2017) 175–182.

[49] Z. Wang, D. Wu, R. Gravina, G. Fortino, Y. Jiang, and K. Tang, *Kernel fusion based extreme learning machine for cross-location activity recognition*, **Information Fusion**, 37 (2017) 1–9.

[50] J Suckling et al, *The Mammographic Image Analysis Society Digital Mammogram Database*, Exerpta Medica. International Congress Series, (1994) pp.375–378.

[51] M. Heath *et al.*, Current Status of the Digital Database for Screening Mammography, *Computational Imaging and Vision*. Springer Nature, pp. 457–460, 1998.

[52] T. M. Deserno, M. Soiron, J. E. E. de Oliveira, and A. de A. Araújo, Computer-aided diagnostics of screening mammography using content-based image retrieval, *Medical Imaging 2012: Computer-Aided Diagnosis*. SPIE-Intl Soc Optical Eng, 2012.

[53] O. Russakovsky *et al.*, *ImageNet Large Scale Visual Recognition Challenge*, **International Journal of Computer Vision**, 115:3 (2015) 211–252.

[54] C. B. R. Ferreira and D. L. Borges, *Analysis of mammogram classification using a wavelet transform decomposition*, **Pattern Recognition Letters**, 24:7 (2003) 973–982.

[55] S. Dhahbi, W. Barhoumi, and E. Zagrouba, *Breast cancer diagnosis in digitized mammograms using curvelet moments*, **Computers in Biology and Medicine**, 64 (2015) 79–90.

[56] N. Dalal and B. Triggs, Histograms of Oriented Gradients for Human Detection, *2005 IEEE Computer Society Conference on Computer Vision and Pattern Recognition (CVPR'05)*. Institute of Electrical and Electronics Engineers (IEEE).

[57] T. Watanabe, S. Ito, and K. Yokoi, *Co-occurrence Histograms of Oriented Gradients for Human Detection*, **Information and Media Technologies**, 5:2 (2010) 659–667.

[58] Y.-B. Lin and C.-P. Young, *High-precision bicycle detection on single side-view image based on the geometric relationship*, **Pattern Recognition**, 63 (2017) 334–354.

[59] M. Meselhy Eltoukhy, I. Faye, and B. Belhaouari Samir, *A comparison of wavelet and curvelet for breast cancer diagnosis in digital mammogram*, **Computers in Biology and Medicine**, 40:4 (2010) 384–391.

[60] S. Ergin and O. Kilinc, *A new feature extraction framework based on wavelets for breast cancer diagnosis*, **Computers in Biology and Medicine**, 51 (2014) 171–182.

[61] J. Y. Choi and Y. M. Ro, *Multiresolution local binary pattern texture analysis combined with variable selection for application to false-positive reduction in computer-aided detection of breast masses on mammograms*, **Physics in Medicine and Biology**, 57:21 (2012) 7029–7052.

[62] S. Lahmiri and M. Boukadoum, *Hybrid Discrete Wavelet Transform and Gabor Filter Banks Processing for Features Extraction from Biomedical Images*, **Journal of Medical Engineering**, 2013 (2013) 1–13.

[63] Y. A. Reyad, M. A. Berbar, and M. Hussain, *Comparison of Statistical, LBP, and Multi-Resolution Analysis Features for Breast Mass Classification*, **Journal of Medical Systems**, 38:9 (2014).

[64] M. N. Do and M. Vetterli, *The contourlet transform: an efficient directional multiresolution image representation*, **IEEE Transactions on Image Processing**, 14:12 (2005) 2091–2106.

[65] A. L. Da Cunha, J. Zhou, and M. N. Do, *The Nonsubsampled Contourlet Transform: Theory, Design, and Applications*, **IEEE Transactions on Image Processing**, 15:10 (2006) 3089–3101.

[66] K. Hanbay, N. Alpaslan, M. F. Talu, D. Hanbay, A. Karci, and A. F. Kocamaz, *Continuous rotation invariant features for gradient-based texture classification*, **Computer Vision and Image Understanding**, 132 (2015).

[67] J. Donahue *et al.*, *DeCAF: A Deep Convolutional Activation Feature for Generic Visual Recognition*, (2013).

[68] A. Krizhevsky, I. Sutskever, and G. E. Hinton, ImageNet Classification with Deep Convolutional Neural Networks. pp. 1097–1105, 2012.

[69] W. Zhang *et al.*, *Deep convolutional neural networks for multi-modality isointense infant brain image segmentation*, **NeuroImage**, 108 (2015) 214–224.

[70] H. R. Roth *et al.*, *Improving Computer-Aided Detection Using Convolutional Neural Networks and Random View Aggregation*, **IEEE Transactions on Medical Imaging**, 35:5 (2016) 1170–1181.

[71] (2017). https://www.analyticsvidhya.com/blog/2016/04/deep-learning-computer-vision-introduction-convolution-neural-networks/ (29, Jun., 2017).

[72] L. Bottou, Large-Scale Machine Learning with Stochastic Gradient Descent, *Proceedings of COMPSTAT'2010*. Heidelberg: Physica-Verlag HD, pp. 177–186, 2010.

[73] G. M. te Brake and N. Karssemeijer, *Segmentation of suspicious densities in digital mammograms*, **Medical Physics**, 28:2 (2001) 259–266.

[74] B. Zheng, Y.-H. Chang, and D. Gur, *Computerized detection of masses in digitized mammograms using single-image segmentation and a multilayer*

topographic feature analysis, **Academic Radiology**, 2:11 (1995) 959–966.

[75] S. Lobregt and M. A. Viergever, *A discrete dynamic contour model*, **IEEE Transactions on Medical Imaging**, 14:1 (1995) 12–24.

[76] Y. Yuan, M. L. Giger, H. Li, K. Suzuki, and C. Sennett, *A dual-stage method for lesion segmentation on digital mammograms*, **Medical Physics**, 34:11 (2007) 4180–4193.

[77] A. R. Domínguez and A. K. Nandi, *Improved dynamic-programming-based algorithms for segmentation of masses in mammograms*, **Medical Physics**, 34:11 (2007) 4256–4269.

[78] L. Vincent and P. Soille, *Watersheds in digital spaces: an efficient algorithm based on immersion simulations*, **IEEE Transactions on Pattern Analysis and Machine Intelligence**, 13:6 (1991) 583–598.

[79] R. S and A. M. Khan, *Bio-Medical Image Segmentatıon Using Marker Controlled Watershed Algorithm: A Case Study*, **International Journal of Research in Engineering and Technology**, 3:15 (2014) 26–30.

[80] C.-C. Jen and S.-S. Yu, *Automatic detection of abnormal mammograms in mammographic images*, **Expert Systems with Applications**, 42:6 (2015) 3048–3055.

[81] P. Agrawal, M. Vatsa, and R. Singh, *Saliency based mass detection from screening mammograms*, **Signal Processing**, 99 (2014) 29–47.

[82] T. Liu *et al.*, *Learning to Detect a Salient Object*, **IEEE Transactions on Pattern Analysis and Machine Intelligence**, 33:2 (2011) 353–367.

[83] T. Avraham and M. Lindenbaum, *Esaliency (Extended Saliency): Meaningful Attention Using Stochastic Image Modeling*, **IEEE Transactions on Pattern Analysis and Machine Intelligence**, 32:4 (2010) 693–708.

[84] J. Donahue *et al.*, *DeCAF: A Deep Convolutional Activation Feature for Generic Visual Recognition*, (2013).

[85] W. Zhang *et al.*, *Mitosis Detection in Breast Cancer Histology Images with Deep Neural Networks*, **Nature**, 35:11 (2013) 529–533.

[86] Z. Jiao, X. Gao, Y. Wang, and J. Li, *A deep feature based framework for breast*

masses classification, **Neurocomputing**, 197 (2016) 221–231.

[87] U. Avni, H. Greenspan, E. Konen, M. Sharon, and J. Goldberger, *X-ray Categorization and Retrieval on the Organ and Pathology Level, Using Patch-Based Visual Words*, **IEEE Transactions on Medical Imaging**, 30:3 (2011) 733–746.

[88] C. Farabet, C. Couprie, L. Najman, and Y. LeCun, *Learning Hierarchical Features for Scene Labeling*, **IEEE Transactions on Pattern Analysis and Machine Intelligence**, 35:8 (2013) 1915–1929.

[89] R. Girshick, J. Donahue, T. Darrell, and J. Malik, *Rich feature hierarchies for accurate object detection and semantic segmentation*, (2013).

[90] Y. LeCun *et al.*, Handwritten Digit Recognition with a Back-Propagation Network. pp. 396–404, 1990.

[91] Y. Bengio and A. Courville, Deep Learning of Representations, *Intelligent Systems Reference Library*. Springer Nature, pp. 1–28, 2013.

[92] Y. LeCun, Y. Bengio, and G. Hinton, *Deep learning*, **Nature**, 521:7553 (2015) 436–444.

[93] Y. Bengio, A. Courville, G. E. Hinton, Y. LeCun, Y. Bengio, and G. E. Hinton, *Reducing the Dimensionality of Data with Neural Networks*, **Nature**, 521:7553 (2015) 436–444.

[94] V. Jain *et al.*, *Supervised Learning of Image Restoration with Convolutional Networks*, 2007 IEEE 11th International Conference on Computer Vision, (2007) pp.1–8.

[95] V. Jain and S. Seung, Natural Image Denoising with Convolutional Networks. pp. 769–776, 2009.

[96] M. Helmstaedter, K. L. Briggman, S. C. Turaga, V. Jain, H. S. Seung, and W. Denk, *Connectomic reconstruction of the inner plexiform layer in the mouse retina*, **Nature**, 500:7461 (2013) 168–174.

[97] D. Ciresan, A. Giusti, L. M. Gambardella, and J. Schmidhuber, Deep Neural Networks Segment Neuronal Membranes in Electron Microscopy Images. pp. 2843–2851, 2012.

[98] D. C. Cireşan, A. Giusti, L. M. Gambardella, and J. Schmidhuber, Mitosis Detection in Breast Cancer Histology Images with Deep Neural Networks. Springer, Berlin, Heidelberg, pp. 411–418, 2013.

[99] Y. LeCun, *The AI Arms Race*, WIRED Business Conference 2016, (2016).

[100] X. Glorot, A. Bordes, and Y. Bengio, *Deep sparse rectifier neural networks*, AISTATS '11: Proceedings of the 14th International Conference on Artificial Intelligence and Statistics, (2011) pp.315–323.

[101] C. Szegedy *et al.*, *Going Deeper with Convolutions*, (2014).

[102] G. E. Dahl, T. N. Sainath, and G. E. Hinton, *Improving deep neural networks for LVCSR using rectified linear units and dropout*, 2013 IEEE International Conference on Acoustics, Speech and Signal Processing, (2013) pp.8609–8613.

[103] A. Coates, A. Arbor, and A. Y. Ng, *An Analysis of Single-Layer Networks in Unsupervised Feature Learning*, **Aistats 2011**, 15 (2011) 215–223.

[104] A. Vedaldi and B. Fulkerson, *Vlfeat: an open and portable library of computer vision algorithms*, Proceedings of the international conference on Multimedia - MM '10, (2010) pp.1469.

[105] N. Howlader, A. Noone, and M. Krapcho, *Statistics Review, 1975-2008*, **National Cancer Institute**, (2011).

[106] L. Van Der Maaten and G. Hinton, *Visualizing Data using t-SNE*, **Journal of Machine Learning Research**, 9 (2008) 2579–2605.

[107] M. D. Zeiler and R. Fergus, Visualizing and Understanding Convolutional Networks, *Computer Vision – ECCV 2014*. Springer Nature, pp. 818–833, 2014.

[108] M. D. Zeiler, D. Krishnan, G. W. Taylor, and R. Fergus, Deconvolutional networks, *2010 IEEE Computer Society Conference on Computer Vision and Pattern Recognition*. Institute of Electrical and Electronics Engineers (IEEE), 2010.

[109] Y. Wang, J. Li, and X. Gao, *Latent feature mining of spatial and marginal characteristics for mammographic mass classification*, **Neurocomputing**, 144 (2014) 107–118.

[110] M. Dong, X. Lu, Y. Ma, Y. Guo, Y. Ma, and K. Wang, *An Efficient Approach*

for Automated Mass Segmentation and Classification in Mammograms, **Journal of Digital Imaging**, 28:5 (2015) 613–625.

[111] R. Rouhi, M. Jafari, S. Kasaei, and P. Keshavarzian, *Benign and malignant breast tumors classification based on region growing and CNN segmentation*, **Expert Systems with Applications**, 42:3 (2015) 990–1002.

[112] M. M. Eltoukhy, S. J. Safdar Gardezi, and I. Faye, *A method to reduce curvelet coefficients for mammogram classification*, IEEE Region 10 Symposium, (2014) pp.663–666.

[113] N. Gedik and A. Atasoy, *A computer-aided diagnosis system for breast cancer detection by using a curvelet transform*, **Turkish Journal of Electrical Engineering and Computer Sciences**, 21:4 (2013) 1002–1014.

[114] S. J. S. Gardezi, I. Faye, and M. M. Eltoukhy, *Analysis of mammogram images based on texture features of curvelet sub-bands* (2014) pp.906924.

CURRICULUM VITAE (CV)

Full Name **:** Nuh ALPASLAN

Date of Birth **:** 19.11.1987

Place of Birth **:** Gaziantep - Nizip

Adress **:** İnönü Üniversitesi Mühendislik Fakültesi Bilgisayar Mühendisliği Bölümü - Malatya

e-mail **:** nuhalpaslan@gmail.com

Educational Background

(Current) **PhD**, Inonu University, Computer Science Dept.

- Advisor: Prof. Dr. Prabir Bhattacharya and Assoc. Prof. Dr. Davut HANBAY

- Area of Study: Medical Image Analysis

MSc, Inonu University, Computer Science Dept., 2013 February

- Thesis Topic: New approaches to gradient based heterogeneous feature extraction methods.

- Advisor: Assoc. Prof. Dr. M. Fatih TALU

- Area of Study: Computer Vision

BSc, Firat University, Computer Science Dept., 2010.

Work Experience

Research Assistant	Bingol University (Turkey)	2010-2011
Research Assistant	Inonu University (Turkey)	2011-
Visiting Research Scholar	Morgan State University (Maryland)	2015-2016
Visiting Research Scholar	Johns Hopkins University (Maryland)	2016

Publications

Journal Papers

- Hanbay K., **Alpaslan N**., Talu, M.F., Hanbay D, Principal curvatures based rotation invariant algorithms for efficient texture classification, Neurocomputing, Volume 199, 26 July 2016, Pages 77-89, ISSN 0925-2312.
- Hanbay K., **Alpaslan N.,** Talu, M.F., Hanbay D, Karci A., Kocamaz A.F., Continuous rotation invariant features for gradient-based texture classification, Computer Vision and Image Understanding, Volume 132, March 2015, Pages 87-101, ISSN 1077-3142.
- Talu, M.F., Gül, M., **Alpaslan, N**., Yigitcan, B., " Calculation Of Melatonin And Resveratrol Effects On Steatosis Hepatis Using Soft Computing Methods", Computer Methods and Programs in Biomedicine, Volume 111, Issue 2, August 2013, Pages 498–506.
- **Alpaslan, N.**, Talu, M.F., Gül, M., Yiğitcan, B., " Calculation of drug effectiveness on treatment of steatosıs hepatis Using HOG based ANN. ", Sakarya University Journal of Science, [S.l.], v. 16, n. 2, jun. 2012.

Conference Papers

- Rahman M., Alpaslan N. (2017). Automated Melanoma Recognition in Dermoscopic Images Based on Extreme Learning Machine (ELM), SPIE Medical Imaging, Orlando, Florida, United States.
- **Alpaslan N**., Rahman M. (2016). Developing a Retrieval Based Diagnostic Aid for Automated Melanoma Recognition of Dermoscopic Images. 2016 IEEE Applied Imagery Pattern Recognition workshop (AIPR2016), Washington DC, United States.
- **Alpaslan N**., Rahman M. (2016). An Integrated Classification and Retrieval Based Diagnostic Aid for Breast Cancer Detection of Mammograms. SIIM Scientific Conference on Machine Intelligence in Medical Imaging, Alexandria Virginia, United States.
- **N. Alpaslan**, MD Rahman, “Developing a Decision Support System for Breast Cancer Detection on Mammograms using Image Processing & Machine Learning”, XSEDE2016, July 17-21, 2016, Miami / Florida, United States. (Best overall paper award).

- N. Alpaslan, Ö. Imik, and D. Hanbay, " Breast mass classification in mammogram images based on wavelet transform," International conference on natural science and engineering Kilis / Turkey, March 2016, pp. 1469-1472.
- N. Alpaslan, MD Rahman, "A Decision Support System (DSS) for Breast Cancer Detection Based on Automated Mass Detection, Classification, and Retrieval of Mammograms," Morgan Innovation Day, March 15, 2016, Annapolis / Maryland.
- N. Alpaslan, MD Rahman, "Mammogram classification assisted by content-based image retrieval for breast cancer diagnosis," 23rd Annual Undergraduate and Graduate Research Symposium, April 14, 2016, Baltimore / Maryland.
- A. Ari, N. Alpaslan and D. Hanbay, "Computer-aided tumor detection system using brain MR images," Medical Technologies National Conference (TIPTEKNO), 2015, Bodrum/Turkey, 2015, pp. 1-4.DOI: 10.1109/TIPTEKNO.2015.7374544.
- N. Alpaslan, A. Kara, B. Zencir and D. Hanbay, "Classification of breast masses in mammogram images using KNN," 2015 23nd Signal Processing and Communications Applications Conference (SIU), Malatya/Turkey, 2015, pp. 1469-1472.doi: 10.1109/SIU.2015.7130121.
- **N. Alpaslan**, K. Hanbay , D. Hanbay and M.F. Talu, A novel texture classification method based on hessian matrix and principal curvatures, Signal Processing and Communications Applications Conference (SIU), 2014 22nd , vol., no., pp.160,163, 23-25 April 2014.doi: 10.1109/SIU.2014.6830190.
- **Nuh Alpaslan**, Kazım Hanbay, Davut Hanbay, M. Fatih Talu, Continuous rotation invariant texture classification based on CoHOG algorithm, Third International Eurasian Conference on Mathematical Sciences and Applications, August 2014, Vienna, Austria.
- **Alpaslan N.**, Toptaş M., Öztürk B., Hanbay D., " Mass Detection on Mammograms and Normal-Benign-Malignant Distinction", National Conference on biomedical technologies, TıpTekno2014, Kapadokya / Turkey, Sep. 2014.
- **Nuh Alpaslan** ; Mehmet Murat Turhan ; Davut Hanbay; Determining noise performance of co-occurrence GMuLBP on object detection task .Proc. SPIE 9067, Sixth International Conference on Machine Vision (ICMV 2013),

90671Y United Kingdom, London (December 24, 2013); doi:10.1117/12.2053138.

- **Alpaslan, N**., Talu, M.F., Gül, M., "Parametric and non-parametric clustering for segmentation of mitochondrial damage in cardiac cells", International Symposium on Biomedical Science and Technology, p.38, 2011.
- Sulu M.,Ince K.,**Alpaslan N**.,Boy O.,Karcı A.,Icen I.," Pattern Discovery in graph-based biological sequence", Fırat University Symposium on Electrical-Electronics and Computer Systems, FEEB-2011, 5-7 October 2011, Elazığ / Turkey.